UNIVERSITÀ DEGLI STUDI DI TRIESTE

XXX CICLO DEL DOTTORATO DI RICERCA IN

NANOTECNOLOGIE

DRUG NANOCRYSTALS
IN
DRUG DELIVERY AND PHARMACOKINETICS

Settore scientifico-disciplinare: **ING-IND/24**

DOTTORANDO
GIANLUCA CHIARAPPA

COORDINATORE
PROF.SSA LUCIA PASQUATO

SUPERVISORE DI TESI
PROF.SSA SABRINA PRICL

CO-SUPERVISORE DI TESI
PROF. MARIO GRASSI

ANNO ACCADEMICO 2016/2017

Drug Nanocrystals in Drug Delivery and Pharmacokinetics

CHAPTER 1

INTRODUCTION

1.1. Biological Engineering

Since its origins dating from the end of the 19th century, chemical engineering (CE) has undergone profound and remarkable transformations (Chiarappa et al., 2017). Indeed, CE developed in Germany, Great Britain, and the USA, all of them already playing a prominent role in chemistry at the end of the 19th century (Peppas and Langer, 2004). For instance, Lewis M. Norton established, at the Department of Chemistry of MIT in Boston, a course in CE concerning the activities conducted in the German chemical industry, the actual leader in chemistry at that time. Frank T. Horpe, holding a B.S. degree from MIT and a doctorate from the University of Heidelberg in 1893 and Norton's successor as professor of the aforementioned course, published, in 1898, the first book on CE entitled "Outlines of Industrial Chemistry". While Norton and Thorpe may be considered the ancestors of CE, Arthur A. Noyes and afterward William H. Walker (1869-1934) were the first to describe the key features of chemical engineer's curriculum (Peppas, 1989). Meanwhile, in Great Britain, Davis, by publishing a book entitled "Handbook of Chemical Engineering" in 1904, became the father of the concept of unit operation which implies the subdivision of chemical processes in different parts such as, for instance, distillation, extraction, filtration, and crystallization, each one governed by distinct principles. The foundation of the American Institute of Chemical Engineers (AIChE) in 1908 definitively gave birth to CE. Obviously, in these early stages of development of the new discipline, the debate over the background knowledge of a chemical engineer was very intense. Milton C. Whitaker, professor of CE at Columbia University and, in addition to his early membership, AIChE president in 1914, stated that chemistry, physics, and mathematics together with notions of mechanics, electricity, and economics should have constituted the basic knowledge of a chemical engineer. He also emphasized the fundamental difference between chemists and chemical engineers as the ability of

the latter to transfer laboratory findings to the industrial production. Around 1920 and until the beginning of World War II, further developments in the field of unit operations and the subsequent introduction of thermodynamics and chemical kinetics significantly contributed to the success of CE. Then, around 1950, the development of the new discipline (CE) underwent a rapid acceleration and a definitive separation from chemistry due to the merit of five American researchers: Neal R. Amundson and Rutherford Aris from the University of Minnesota, R. Byron Bird, Edwin N. Lightfoot, and Warren E. Stewart from the University of Wisconsin. They promoted the innovative idea of a common feature unifying the apparently different unit operations and the equations of conservation of mass, energy, and momentum. The practice of analyzing separately the various unit operations persisted, but differential volume and balance equations became the core of the new approach to solving chemical engineers' problems. Approximately five years after the publication of "Transport Phenomena" (1960), the famous book written by Bird, Stewart, and Lightfoot, the concept of unit operation became obsolete and the new approach definitively affirmed in the research and education fields.

In Italy and other industrially less developed countries, CE advancement followed the American one. In fact, the origins of Italian CE date from the end of World War II, when Italy experienced its economic recovery. However, a clear evidence of the existence of CE in Italy was provided only in the '50s. Indeed, in those years, a major contribution to the growth of Italian chemical industry and CE was the nationalization of electricity production (sadly connected with the "announced" tragedy of Vajont in northern Italy (Paolini and Vacis, 1997)) and the consequent establishment of the National Board for Electricity (Enel). As a result, Edison, the main Italian private producer of electricity at that time, received full compensation from the Italian government for the expropriation of its power plants and invested that money in the sector of the chemical industry. Therefore, the necessity of rapidly acquiring the appropriate scientific and technical background knowledge without resorting to a slow research process required making a direct approach to consolidated German chemical companies such as BASF and Bayer. The exigencies of a close link between the investor and the German technical counterpart led, in 1958, to the foundation of the Italian Association of Chemical Engineering (AIDIC) and the Italian chemical industrial parks of Marghera, Mantua, and Priolo date from that period. Since then the development has been rapid, various, and rich in passionate discussions regarding the optimal organization at the national level (Astarita, 1980).

CE attitude to traditionally distant cultural horizons such as medicine, biology, and pharmacy became evident only in the mid-seventies, even though the birth of Biological Engineering (BE) may be dated around the early sixties (Peppas and Langer, 2004). This evolution was due to

talented American researchers (Elmer L. Gaden, Arthur B. Metzner, R. Byron Bird, Edward W. Merrill) who realized that chemical engineers could usefully contribute to areas different from the traditional ones. Accordingly, they underlined the importance of an interdisciplinary approach which would have successively proved to be a winning strategy in modern research. Obviously, the realization of such a profound change was possible because major American organizations such as the National Science Foundation and the National Institutes of Health decided to invest in these innovative methodological approaches to medicine, biology, and pharmacy. As a result, between the early sixties and the late seventies, Merril (1959) investigated blood rheology, Leonard (1959) designed an artificial kidney, Colton (1966) focused on hemodialysis, Peppas worked on contact lenses (1976) and smart hydrogels (1979), while Langer (1979) explored the drug release from polymeric matrices. As so often happens, the first involvement of a chemical engineer in the biomedical field was completely fortuitous as a Boston physician requested Merrill's help in solving a problem concerning the measurement of blood viscosity. Consequently, relevant information regarding the non-Newtonian properties of blood related to the strain rate, hematocrit, and to the presence of various proteins and white blood cells were gathered. Due to the development of mathematical models and computing power since the early eighties, CE could spread to areas of medicine hitherto unthinkable. In this regard, it is worth mentioning the study of the formation of atherosclerotic plaques based on mathematical models considering the mass transport in blood owing to diffusion, convection, carrier-mediated and vesicular transport mechanisms (Feig et al., 1982).

A noticeable contribution of chemical engineers to biomedicine also concerned biomaterials such as hydrogels. Indeed, these materials, although available since 1935, became the subject of intense interest only after the pioneering work of Wichterle and Lim (Wichterle and Lim, 1960), the first to prepare polyhydroxyethylmethacrylate-based gels, the basic constituent of soft contact lenses since the '70s. Moreover, applied thermodynamics and molecular theories made a major contribution to understanding and designing the properties of various biomaterials. Another topic covered by chemical engineers and very close to biomedicine consisted in designing living tissues. The guiding principle of tissue engineering states that the formation of tissues or parts of human organs requires an appropriate spatial arrangement of cells. This may be realized by seeding cells in suitable porous polymeric structures called scaffolds, i.e. a support or a matrix facilitating the migration, binding, and the transport of cells or bioactive molecules to replace, repair, and regenerate tissues (ASTM, 2007). For instance, it was possible to obtain human nervous tissues, cartilage, and hepatocytes (Folkman and Haudenschild, 1980; Bissell and Barcellos-Hoff, 1983; Vacanti et al., 1988). Similarly, chemical engineers encapsulated cells in polymeric structures in

order to obtain the so-called immunoisolation membranes, which are permeable to small molecules such as glucose or other nutrients but impermeable to large molecules such as immunoglobulins and the cells of the immune system.

One of the fruits of this sparkling cultural context is the recent foundation of the Society for Biological Engineering (SBE) by AIChE, whose aim is to promote engineers and scientists to advance the integration between biology and engineering. Nevertheless, one of the most important contributions of CE to the biomedical field thus far has undoubtedly been drug delivery committing a large number of chemical engineers, among whom Peppas and Langer should be remembered.

1.2. Quantitative System Pharmacology

All the previous considerations perfectly match an emerging discipline named quantitative systems pharmacology (QSP), which dates from the beginning of the third millennium but has become known to a wider audience since 2010 (Sorger et al., 2011; Knight-Schrijver et al., 2016). Similarly to other disciplines, QSP has been evolving through independent innovative efforts rather than an overarching strategic plan (Musante et al., 2016). While different definitions may be found in literature (Sorger et al., 2011), QSP may be defined as the quantitative analysis of the dynamic interactions between drug(s) and a biological system aiming to understand the behavior of the entire system rather than that of its individual components (van der Graaf et al., 2011; Gadkar et al., 2016). Accordingly, the output of QSP is a knowledge base or a model with predictive capabilities to, for instance, enhance drug discovery, rationalize drug action, predict individual response to treatment, assess drug efficacy and safety, enable a rational design of clinical trials and an equally rational interpretation of their results (Knight-Schrijver et al., 2016; Androulakis, 2016). Consequently, QSP also has a multidisciplinary approach, mathematics, engineering, physics, biology, and pharmacy being its roots. Indeed, this is the only way to provide creative and innovative solutions to the increasingly complex problems posed by personalized and precision medicine (Sorger et al., 2011; Musante et al., 2016). Ultimately, BE may be considered a modern contribution of chemical engineers to QSP.

1.3. Physiologically-based Pharmacokinetic Models

Recent studies of pharmacokinetics (PK) in mammals and, more specifically, in humans have required a multi, inter, and transdisciplinary approach (MITA). PK entails the dynamic quantification of administered drugs in the different organs and tissues of patients. In detail, drugs,

after administration, undergo the ADME (Absorption, Distribution, Metabolism, Excretion) processes through complicated pathways (ADME pathways) which are mediated by the anatomical and physiological characteristics of the mammalian body. A MITA to PK requires contributions from different perspectives and cultural backgrounds epitomized by physicians, pharmacists, biologists, chemists, and engineers (Ferrari et al., 2005).

When engineers start to approach the PK subject, a large number of scientific publications guide them through rather complex phenomena which, from a mechanistic viewpoint, require deepening the understanding of both anatomy and physiology. Indeed, when one/two-compartment simplified models are taken into consideration (Wagner, 1993), an engineer may recognize their limitations in terms of modeling details and physical consistency with the human body. On the contrary, the introduction of an excessive number of details in the PK model (Jain et al., 1981) may lead to an overparameterized (98 adaptive parameters) and oversized (38 ordinary differential equations (ODE) and 21 compartments) model whose utility is constrained to one mammalian species (rats) and limited to one administration route (intravenous). In this context, physiologically-based pharmacokinetic (PBPK) models demonstrate their potential since they describe how the mammalian body follows ADME pathways. These models are based on an anatomical and physiological representation of organs and tissues interconnected by the circulatory and lymphatic systems. Engineers' perception of the functioning of organs and tissues is always in terms of process units, unit operations, vessels, reactors, membranes, transport phenomena, ducts, inputs, outputs, recirculation, and efficiency. Hence, according to process engineers' point of view, the mammalian body may be represented by a set of interconnected process units (compartments) exchanging mass flows and symbolizing either single or lumped organs/tissues (Di Muria et al., 2010; Del Cont et al., 2014). Some may be mathematically represented by perfectly mixed tanks/reactors (such as stomach, liver, gallbladder, and poorly perfused tissues which may lump different subsystems together), others may be assimilated to plug flow ducts/reactors such as the small and large intestinal lumina, where distributed mass flows cross the surrounding wall (i.e. the intestinal membrane) and deliver substances (i.e. nutrients and active principles) to the gastrointestinal circulatory system by means of two-way mass transfer coefficients. The mass transfer through the intestinal wall may be assumed as a diffusive phenomenon based on Fick's law, but, in reality, the involved cellular membrane molecular exchange is more complicated than a passive gradient-driven mass transfer. The plug flow representation of the intestinal lumina may be further simplified into a suitable series of perfectly mixed tanks/reactors. Hence, the partial differential equations describing the spatiotemporal mass flows are discretized into finite difference equations and the translation into a system of ODE

renders the numerical solution easier and more efficient. At the same time, the organs/tissues, represented in terms of compartments and symbolized by an equivalent plant equipment, are interconnected by mass transfer pathways. The process flow diagram, which graphically shows the interconnected compartments, may also include recirculation, for instance, the enterohepatic circulation between gallbladder and duodenum through Oddi's sphincter discussed by Abbiati and co-workers (Abbiati et al., 2015a). The periodic recirculation of bile from the gallbladder to the intestinal lumen is mediated by Oddi's sphincter acting as a valve, thus opening and closing according to the feeding and digestive processes. The aforementioned entails the simulation of periodic batch, semi-batch, and continuous processes as a function of the specific compartment. Every patient may be characterized by a personalized PBPK model depending on sex, age, body mass index, and other factors. In order to consider these factors, the principal organs such as liver and kidneys may be characterized by a specific efficiency as catalysts, heat exchangers or separation units. The combination of these elements allows writing a series of dynamic mass balances around the nodes of the plant (i.e. compartments), thus obtaining an ODE system. Hence, the concentrations in organs and tissues are dependent variables to be integrated numerically in order to determine PK profiles involved in ADME phenomena. The input and output streams of the mammalian body are represented by administration routes and excretion pathways, respectively. The estimated organs/tissues concentrations constitute a valuable decision support tool for physicians, by allowing them to comprehend the distribution and metabolic pathways of drugs in patients and thus determine the amount of active principle per body mass and time unit to be dynamically administered in order to either shorten healing times or equalize the concentration distribution in the case of chronic diseases treatment (Abbiati et al., 2015b).

1.4. Bioavailability Enhancement

Bioavailability, defined as the rate and extent to which the active substance or the active moiety is absorbed from a pharmaceutical form and becomes available at the site of action (Pharmacos 4), depends on several factors, among which the drug solubility in an aqueous environment and the drug permeability across lipophilic membranes play a prominent role (Yu et al., 2000). Indeed, only dissolved molecules may be absorbed by cellular membranes, thus reaching the site of drug action (vascular system, for instance). Depending on solubility and permeability, drugs may be classified into four different classes (Amidon et al., 1995) and, therefore, a drug belonging in class IV (high solubility and permeability) is defined as bioavailable. Several techniques are commonly employed to improve the bioavailability of poorly water-soluble but permeable drugs (Perrett and

Venkatesh, 2006). In this sense, drug particle size reduction, drug encapsulation in the lipid matrix of nano/microspheres (Charman et al., 1992) or drug dissolution in the dispersed lipophilic phase of oil/water emulsions or microemulsions (Costantinides, 1995; Gasco, 1997; Pouton, 1997; Kumar and Mittal, 1999) may be mentioned. A similar goal is achievable through drug complexation with cyclodextrins in solution or in the presence of the molten drug. Finally, by means of solvent swelling, it is possible to load a drug in a nanocrystalline or amorphous state into a polymeric carrier, thus considerably increasing its bioavailability (Grassi et al., 2003; Dobetti et al., 2001). For instance, the simple particle size reduction by milling allowed reducing fenofibrate (Tricor®) dose from a standard drug 300 mg capsule to a bioequivalent 145 mg tablet containing nanocrystalline drug (Perrett and Venkatesh, 2006). Interesting examples of lipid-based formulations (either self-emulsifying or emulsifying due to the presence of bile salts) are antivirals – Norvir® (ritonavir) and Fortovase® (saquinavir) – and immunosuppressive cyclosporines – Sandimmune® and Neoral®. While Fortovase® increased saquinavir bioavailability up to threefold with respect to the original Invirase® (saquinavir mesylate in powder form) (Roche), the reduction of emulsion particle size allowed Neoral® to be more bioavailable than the original Sandimmune® (Van Mourik et al., 1999). Cyclodextrins may be found in several marketed products such as Vfend® (voriconazole), Geodon® (ziprasidone mesylate), and Sporanox® (itraconazole). These solutions are intended for parenteral or oral use (Perrett and Venkatesh, 2006) and characterized by a high cyclodextrin/drug ratio (from approximately 15:1 to 40:1). Prograf® and Sporanox® capsules are successful examples of commercial applications of the solvent swelling technique (Ueda et al., US Patent; Gilis et al., US Patent). Obviously, each approach shows advantages and disadvantages and may be more suitable for a certain type of drug or a specific administration route. Mechanochemically activated systems, in particular, may be administered in the form of tablets or capsules, as both formulations preserve the "activated" state. In general, any formulation not requiring the employment of solvents or high temperatures may be in principle taken into consideration. For these reasons, mechanochemically activated systems are suitable for oral administration, the most common route for humans due to better patient compliance and versatility with regard to dosing conditions. Nevertheless, the mechanochemical and solvent swelling activation entails a considerable bioavailability improvement when the drug solubility in aqueous media is lower than 100 $\mu g/cm^3$.

1.5. Nanocrystals

As the oral route has always been the simplest and most appreciated way to administer drugs,

many efforts were made in the past to render this administration also practicable for poorly water-soluble drugs, which are usually characterized by low bioavailability (Grassi et al., 2007) and represent approximately 40% of the drugs in the development pipelines. In addition, up to 60% of synthesized compounds are poorly soluble (Lipinski, 2002) and 70% of potential drug candidates are discarded due to low bioavailability related to poor solubility in water (Cooper, 2010). Examples of commonly marketed poorly soluble drugs (water solubility less than 100 μg cm^{-3}) include analgesics, cardiovasculars, hormones, antivirals, immunosuppressants, and antibiotics (Grassi et al., 2007). Thus far, an effective solution to increase the bioavailability of poorly soluble drugs has appeared to be nanonization, i.e. the pulverization of solid substances into the nanometer range, which dramatically increases the crystal surface-volume ratio and the solid-liquid interface. This immediately translates into the nanocrystals melting temperature (T_m) and enthalpy (ΔH_m) reductions (Brun et al., 1973), which, in turn, is reflected in the increase of drug water solubility and, consequently, drug bioavailability.

A valid explanation for this phenomenon is the different arrangement of the surface and bulk phases. Indeed, the surface atoms/molecules present fewer bonds than the bulk ones (Lubashenko, 2010) and, accordingly, a higher energy content. Therefore, the surface lattice destruction necessitates less energy and is favored over the bulk one. Molecular dynamics (MD) simulations and experimental data regarding Au nanocrystals confirmed the previous theoretical analysis (Huang et al., 2008; Toledano and Toledano, 1987) by highlighting the different behavior of the surface and bulk atoms. In fact, the coherent electron patterns diffracted by single nanocrystals depend on the atomic structure of surfaces. This interpretation, valid for metals, may be also extended to organic substances (Jiang et al., 1999). Indeed, the fundamentally vibrational melting entropy of organic crystals implies that the organic molecules in crystalline arrangement behave analogously to metals. This indicates that the peculiar properties of organic nanocrystals may be investigated by means of the same theoretical models employed for metallic nanocrystals. Indeed, the melting entropy of organic crystals is essentially constituted by a vibrational component, which implies that the molecules in organic crystals exhibit a similarity to the atoms in metallic crystals. Accordingly, for molecular solids, the difference in activation energy between surface and bulk may be explained by a difference in molecular mobility (Jiang et al., 1999). Obviously, the surface atoms/molecules effect is macroscopically detectable only if their number is comparable to the bulk one, i.e. when the surface-volume ratio is no longer negligible as it happens in nanocrystals.

Several researchers (Zhang et al., 2000) investigated both experimentally and theoretically the melting properties in connection with crystal size, whereas solubility dependence is still controversial due to experimental measurement difficulties (Grassi et al., 2007, Buckton and

Beezer, 1992). In particular, manufacturing processes, usually altering surface characteristics by introducing lattice defects, prevent the use of fine crystals for experimental solubility determinations (Mosharraf and Nyström, 2003). Little impurities are able to affect solubility and polydispersed crystals undergo Ostwald ripening (Madras and McCoy, 2003), the growth of larger crystals at the expense of the smaller ones, which leads to an asymptotic solubility diminution. Therefore, in the light of these considerable experimental difficulties, the theoretical determination of drug solubility as a function of nanocrystals size has become mandatory. Despite the previously discussed experimental issues, the manufacture of nanocrystal-based drug delivery systems is feasible without particular difficulties. For instance, solvent swelling (Carli et al., 1986; Grassi et al., 2000), supercritical carbon dioxide (Debenedetti et al., 1993; Kikic et al., 1999), cogrinding (Grassi et al., 1998; Voinovich et al., 2009; Hasa et al., 2011; Hasa et al., 2012; Coceani et al., 2012), and cryomilling (Crowley and Zografi, 2002) allow the dispersion of the drug, in nanocrystalline or amorphous form, into a carrier, typically an amorphous cross-linked polymer (Colombo et al., 2009). Indeed, the polymer acts as a stabilizer for nanocrystalline/amorphous drugs, which otherwise would tend to recrystallize, thus returning to their more thermodynamically stable macrocrystalline state. The presence of drug and stabilizer generates a distribution of particles with different sizes, i.e. the secondary grains, composed of crystals, i.e. the primary grains, which are connected by an amorphous phase constituted by the amorphous drug and/or stabilizer. Furthermore, primary grains are constituted by short-range structural arrangements (crystallites), i.e. those coherent crystalline domains whose size is commonly referred to as crystal dimension (Colombo et al., 2009). The reliability and effectiveness of such delivery systems were proved by in vitro and in vivo tests, which revealed a considerable bioavailability improvement for poorly water-soluble but permeable drugs (Colombo et al., 2009; Meriani et al., 2004), otherwise known as class II drugs according to Amidon's classification (Amidon et al., 1995).

Traditionally, the peculiar properties of nanocrystals have been explored in metallurgy (Nanda, 2009; Goswami and Nanda, 2012) and then in materials (Ha et al., 2004; Ha et al., 2005) and pharmaceutical sciences (Hamilton et al., 2012). In particular, Ha and co-workers (Ha et al., 2004), by studying the crystallization of anthranilic acid (AA) in nanoporous polymeric and vitreous matrices, were the first to report on the effect of nanoconfinement on organic polymorphic crystals. They demonstrated that polymorph selectivity during the sublimation of AA was influenced by the surface properties of glass substrates. Indeed, the preference for the metastable form II in smaller pores is assumed to be caused by a smaller critical nucleus size than the other two polymorphs (I and III). In another paper, Ha and co-workers (Ha et al., 2005), by examining the crystallization of organic compounds in nanochannels of controlled pore glass and porous

polystyrene, detected a clear $T_m/\Delta H_m$ depression associated with the decreasing channel diameters, this being consistent with the increasing crystals surface/volume ratio. In addition, they realized that T_m depression also depends on the properties of the embedding matrix and this was explained with the different nanocrystals interactions with channel walls. While Zandavi demonstrated the validity of thermodynamics at least in pores down to a radius of 1.3 nm (Zandavi and Ward, 2013), Beiner and collaborators deepened the understanding of the effect of pores morphology on crystals polymorphism (Beiner et al., 2007) and the appearance of an amorphous drug layer between pore wall and nanocrystal surface due to drug-wall interactions (Rengarajan et al., 2008). Hasa (Hasa et al., 2016), Belenguer (Belenguer et al., 2016), and co-workers focused the attention on cocrystals. In particular, Hasa and co-workers (Hasa et al., 2016) explored how the amount of a specific liquid present during the liquid-assisted mechanochemical reactions may be exploited to rapidly investigate polymorphs diversity. Indeed, for the considered multicomponent crystalline system formed by caffeine and AA in a 1:1 stoichiometric ratio, only 4 out of 15 liquids were found to be highly selective for one polymorphic form, while the others produced more than one cocrystal polymorph depending on the amount of liquid used (the selected volume range was 10–100 μL). A similar phenomenon was observed by Belenguer and co-workers (Belenguer et al., 2016) while investigating two other (dimorphic) systems, namely 1:1 theophylline/benzamide cocrystals and an aromatic disulfide. Importantly, Belenguer and co-workers (Belenguer et al., 2016) also provided a possible explanation for the different amounts of a liquid which produce different polymorphic forms. Indeed, such phenomenon was related to particle size: metastable polymorphs, as micrometer-sized or larger crystals, may often be thermodynamically stabilized at the nanoscale. Additionally, surface effects were reported to be significant in the polymorphism at the nanoscale and the outcomes of mechanochemical equilibrium experiments appeared to be, in general, controlled by thermodynamics. While Lee was able to measure amorphous ibuprofen solubility by resorting to nanoporous aluminum oxide (Lee et al., 2013), Beiner and his group proved that nanoconfinement is a strategy to produce and stabilize otherwise metastable or transient polymorphs of pharmaceuticals, as required by controllable and effective drug delivery (Graubner et al., 2014; Sonnenberger et al., 2016). Myerson and co-workers (Eral et al., 2014; Badruddoza et al., 2016) investigated the use of biocompatible alginate hydrogels as smart materials to crystallize and encapsulate different types of drugs (acetaminophen and fenofibrate). Interestingly, they discovered that hydrogels with smaller meshes appear to show faster nucleation kinetics. In addition, Myerson and co-workers (O'Mahony et al., 2015; Dwyer et al., 2017) employed controlled pore glass and porous silica supports to obtain nanocrystals of fenofibrate and griseofulvin, thus achieving an increased dissolution rate in comparison with that of the

original macrocrystals.

1.6. Drug Activation

In the light of what discussed thus far, the nanocrystalline and amorphous states may be considered an "activated" condition as they are characterized by an enhanced solubility (and thus bioavailability) with respect to the macrocrystals they originate from. The experimental verification of this activation falls into the broad field of the solid state characterization. Typically, the considered approach evaluates the macro, nanocrystalline or amorphous states of a drug embedded in an amorphous matrix acting as a stabilizer. Indeed, the nanocrystalline and amorphous states are unstable and tend to return to the original macrocrystalline condition. Accordingly, the techniques based on the difference of periodicity of the atoms in crystals (X-rays powder diffraction, XRPD), the energy of the bond stretching/bending and lattice vibrations (infrared, IR, and Raman spectroscopy), the electronic environment of nuclei (nuclear magnetic resonance, NMR), the thermal analysis of heat flow or weight change (differential scanning calorimetry, DSC, and thermal gravimetric analysis, TGA), and morphology (optical microscopy) may be useful for this purpose (Stephenson et al., 2001; Bugay, 2001). In particular, the solid state characterization serves to exclude the formation of new chemical species (the evidence of chemical reactions) or polymorphs raising regulatory issues. At the same time, this characterization is required to estimate the residual amount of crystalline drug (X_{nc}) after the activation treatment. Indeed, this parameter may be roughly regarded as a measure of drug activation. More precisely, a more proper evaluation of activation not only requires the determination of X_{nc} but also the size distribution of drug crystals. In addition to the aforementioned techniques, other approaches are able to provide an estimation of activation such as solution calorimetry, water sorption (Yu, 2001), and release tests (RT) (Grassi et al., 2007).

The DSC characterization is based on the reduction of $T_m/\Delta H_m$ with crystals size decrease. Indeed, at the nanoscale, crystals properties not only depend on bulk atoms/molecules but also on the surface ones. This is due to the fact that surface atoms show fewer interatomic bonds than the bulk ones, which makes the former more loosely bound than the latter (Zhang et al., 2000). The T_m reduction in nanosized particles was originally predicted by the thermodynamic nucleation theory in the early 1900s (Gibbs-Thomson's equation) (Gibbs, 1928; Ha et al., 2005):

$$\frac{\Delta T_m}{T_m} = -\frac{4\gamma^{sl}}{\rho_s \Delta H_m d}\cos(\theta) \qquad (1.6.1)$$

where d is crystal diameter, γ^{sl} is solid-liquid surface tension, and θ represents the contact angle of the solid nanocrystal with the pore wall in the case of crystals confined in nanopores, being $\theta = 180°$ ($\cos(\theta) = -1$) in the case of unconfined nanocrystals.

When, at the moment of melting, a substance decomposes and/or solid phase interactions occur during heating, DSC is unable to detect the presence and abundance of crystals. In this case, a valid alternative is represented by XRPD provided that the amount of amorphous phase and/or adsorbed water is modest and the X-rays diffraction pattern is unaffected by considerable peak overlaps and the preferred orientation of the powder sample is meaningless. While a detailed description of the crystals abundance determination after drug/carrier grinding goes beyond the scopes of this chapter, it is interesting to recall its working equation (Bergese et al., 2003):

$$X_D = \frac{\sum_i I_i}{\sum_i I_{i0}} [f(X_D)]^{\alpha} \tag{1.6.2}$$

where X_D is the drug macro and nanocrystalline fraction in the ground mixture, I_i is the area of the i^{th} peak belonging to the X-rays pattern, $\sum_i I_i$ and $\sum_i I_{i0}$ are, respectively, the sum of all peak areas characterizing the ground and original drug X-rays pattern, α is a semiempirical factor considering microabsorption effects, and $f(X_D)$ is a function of X_D depending on the drug-carrier mixture. The unknowns α, $f(X_D)$, and $\sum_i I_{i0}$ may be calculated from a calibration procedure based on the measurement of several physical mixtures of the original crystalline drug and the carrier. While amorphous structures cause a broad diffraction owing to the lack of a long-range periodicity of the atomic arrangement, nanocrystalline materials entail a deviation from the X-rays diffraction pattern related to an ideal crystal since an atomic arrangement periodicity exists only over a few molecular distances. In particular, a finite crystallite size, strain, and extended defects (stacking faults, dislocations) lead to broadening diffraction peaks. In this context, the entire pattern profile modeling (peaks position, intensity, width, and shape) may provide a complete evaluation of the grains size distribution and lattice defects content (Grassi et al., 2007). The use of the so-called radial distribution function, evaluable from experimental patterns by means of Fourier's transform, allows determining the probability of finding an atom at a given distance from the center of a reference atom of the system (Proffen et al., 2003). Very smooth and low noise experimental data are required to achieve reliable and reproducible results. For these reasons, synchrotron and similarly intense X-rays sources are recommended. An alternative approach to the analysis of diffraction data of amorphous materials is the one proposed by Luterotti and co-workers (Luterotti

et al., 1998). In this regard, crystallite size and microstrain were introduced to consider the diffraction peaks broadening of an amorphous structure. By reducing coherent scattering domains, the corresponding Bragg's reflections broaden to such an extent that they produce a typical amorphous solids diffraction pattern (halo). Furthermore, in the pharmaceutical field, XRPD is able to provide further information concerning the drug-stabilizer system. Indeed, while drug activation is desirable, the formation of new chemical entities or polymorphs is undesirable, as their presence would lead to regulatory issues. Undoubtedly, the Food and Drug Administration (FDA) approval for the native drug is unextendable to the other chemical compounds produced by the process (solvent swelling, supercritical carbon dioxide, cogrinding, and cryomilling) considered to obtain drug activation. In this context, XRPD plays a crucial role, as the formation of polymorphs or the occurrence of chemical transformations is reflected in evident differences between the XRPD pattern of the native and activated drug.

The drug release test on activated systems is another excellent method to evaluate the activation level, although the determination of the crystalline, nanocrystalline, and amorphous drug abundance is indirect by interpreting experimental data by means of proper mathematical models (Grassi et al., 2007). Unfortunately, a unifying model which describes the drug release from every activated system is unavailable, as release kinetics also depends on the considered carrier (stabilizer). In this regard, carriers may be approximately divided into two main classes: the cross-linked polymers and the remaining ones. This classification is motivated by the fact that, in the second case, drug-carrier interactions develop superficially through more or less complex adsorption/desorption mechanisms, while, in the first case (cross-linked polymers), the topological properties of the carrier are also able to play a key role, as the drug may be embedded in the (stable) polymeric network. Accordingly, both the drug diffusion into the (swelling) network and drug-polymer interactions affect release kinetics. Besides these mechanisms, the crystalline, nanocrystalline, and amorphous drug dissolution in the release medium also rules release kinetics. Indeed, after contacting the external release medium, the stabilizing action exerted by the carrier vanishes (obviously, by following different kinetics depending on the carrier type) and the drug starts dissolving with the possible formation of macrocrystals and/or polymorphs. As drug solubility depends on crystal dimension (the amorphous phase may be regarded as crystals of vanishingly small dimensions), the release process may occur due to the time-dependent drug solubility (Grassi et al., 2007). One of the most common equations used to describe this particular behavior is Nogami's (Nogami et al., 1969):

$$C_s(t) = \left(C_{a,nc} - C_{mc}\right)e^{-K_r t} + C_{mc} \tag{1.6.3}$$

where C_s is the time (t) dependent drug solubility, K_r is the recrystallization constant, $C_{a,nc}$ represents the amorphous or nanocrystalline drug solubility, while C_{mc} indicates the solubility of macrocrystals. This equation states that, at the beginning ($t = 0$), C_s equals $C_{a,nc}$ and then decreases exponentially, thus reaching C_{mc}. Obviously, eq 1.6.3 intrinsically takes account of macrocrystals dissolution (those not undergoing recrystallization phenomena). Indeed, their dissolution is represented by eq 1.6.3 when $K_r = \infty$ (C_s is then always equal to C_{mc}). Accordingly, the general dissolution equation becomes:

$$\frac{\partial C_{a,nc}}{\partial t} = -K_t^{a,nc}\left[C_s(t) - C\right] \tag{1.6.4}$$

where $K_t^{a,nc}$ indicates the amorphous or nanocrystalline drug dissolution constant. Obviously, eq 1.6.4 may be written for the amorphous, nanocrystalline, and macrocrystalline drugs. The contribution of each equation to the global dissolution rate depends on the relative abundance of each form. By associating eq 1.6.4 with a proper equation considering the drug diffusion across the polymeric network, the final mathematical model able to interpret experimental data is obtained.

Experimentally, release tests may be performed in the sink or non-sink conditions according to the usual dissolution testing procedures. While, in sink conditions, higher activation levels are reflected in higher release kinetics, the adoption of non-sink conditions allows observing a peculiar release pattern. Indeed, due to the conversion of the amorphous drug into the more stable macrocrystalline form implying a drug solubility reduction, the release concentration curve may display a rapid increase followed by a decrease.

1.7. Aim

In the previously delineated context, the attention of the present doctoral thesis was turned to drug nanocrystals embedded/mixed in/with cross-linked polymeric microparticles acting as a stabilizer for nanocrystalline and amorphous drugs (Colombo et al., 2009). Owing to their low water solubility, good permeability, and relevance to the pharmaceutical industry (Grassi et al., 2007; Davis and Brogden, 1994), nimesulide, griseofulvin, and nifedipine, three typical poorly water-soluble drugs, were selected as a proof of concept in the present study.

Thus far, the majority of theoretical approaches have been devoted to investigating the relation existing between spherical nanocrystals size and $T_m/\Delta H_m$, while only a few of them considered

non-spherical shapes (Nanda, 2009). Moreover, these last ones were focused on metallic nanocrystals and none of them on drug nanocrystals. It seems that no study aimed at elucidating the effect of nanocrystals shape on the reduction of $T_m/\Delta H_m$ and the consequent increase of solubility is present in the literature until now. Accordingly, this thesis attempted to theoretically study the dependence of $T_m/\Delta H_m$ decrease on nanocrystals size by means of a thermodynamic model considering crystals shape (sphere, cylinder, parallelepiped). The outcomes of this model were validated by the corresponding ones obtained from molecular dynamics simulations as a function of drug crystal shape and size. Finally, the information acquired from the developed thermodynamic model was embodied in another mathematical model dedicated to describing the drug release from an ensemble of polydispersed polymeric particles administered following the oral route. Therefore, this model could describe the simultaneous processes of drug release and drug absorption by living tissues and allow evaluating the effect of nanocrystals.

CHAPTER 2

THERMODYNAMIC MODEL

2.1. Physical Frame

At the beginning of the last century, T_m decrease by means of crystal size reduction was thermodynamically predicted and experimentally demonstrated (Pawlow, 1909). Afterward, several researchers developed theoretical models to explain $T_m/\Delta H_m$ depression phenomenon accompanying crystals size decrease. Among them, the thermodynamic ones (Nanda, 2009;

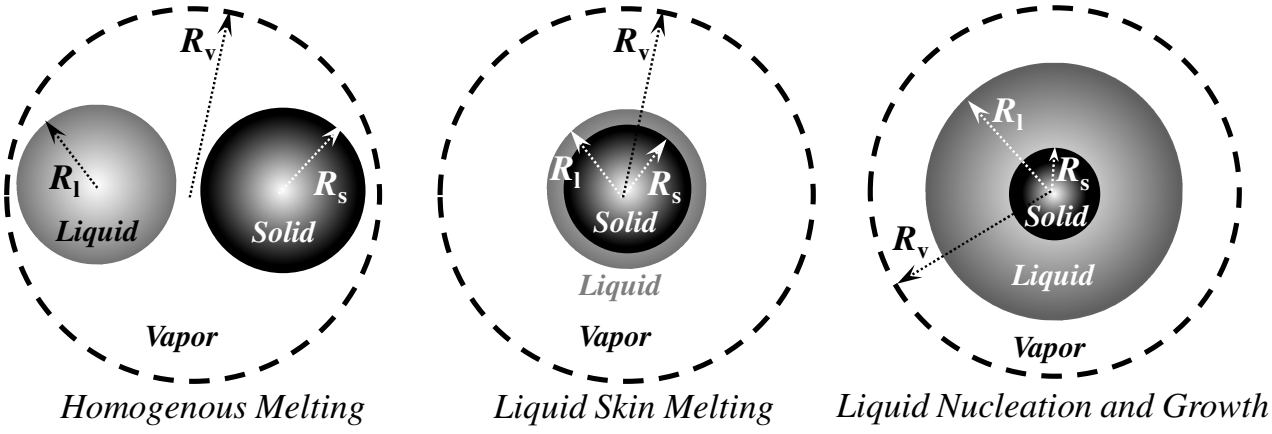

Figure 2.1. Thermodynamic models of nanocrystals melting are based on three mechanisms: Homogeneous Melting, Liquid Skin Melting, Liquid Nucleation and Growth. R_v, R_l, and R_s are the vapor, liquid, and solid phases radii, respectively.

Sdobnyakov et al., 2008) were confirmed by MD simulations and were potentially able to describe different crystal shapes. Furthermore, these models are well adapted to describe the phenomena involved in the drug melting process. Fundamentally, the thermodynamic models rely on the three physical schemes shown in Figure 2.1 (Nanda, 2009). The homogeneous melting (HM) approach

assumes the equilibrium between the solid and liquid drug phases that share the same mass and lie in the vapor phase. The liquid skin melting (LSM) theory presupposes the formation of a thin liquid layer over the solid core. The thickness of the liquid layer remains constant until the solid core completely melts. According to the liquid nucleation and growth (LNG) approach, on the contrary, the liquid layer thickness grows while approaching T_m. The solid core melting occurs when the liquid layer thickness is no longer negligible in comparison to the solid core size.

Despite the fact that, theoretically, there are no reasons for preferring one of the three mechanisms depicted in Figure 2.1 (HM, LSM, LNG), two distinct physical considerations are in favor of the LSM and LNG approaches. The first one relies on the direct observation of drug crystals melting which shows the formation of a liquid shell around the solid phase before the occurrence of complete melting (hot stage microscopy approach). The second one is strictly related to a particularly interesting application of nanocrystals, i.e. the controlled delivery of drugs (the main focus of this thesis), where delivery systems relying on drug nanocrystals-polymer mixtures are often employed. Indeed, regardless of the drug loading technique considered to prepare drug-polymer mixtures (solvent swelling, supercritical carbon dioxide, co-grinding, and cryomilling), the coexistence of drug nanocrystals and amorphous drug inside the polymeric matrix is usually observed (Bergese et al., 2004; Bergese et al., 2005). Thus, when the ratio between the amount of nanocrystalline drug and amorphous drug is very high (i.e. when nanocrystals mass fraction (X_{nc}) is close to one), drug melting should occur according to the physical description of the LSM approach. On the contrary, when X_{nc} approaches zero, i.e. when few nanocrystals melt inside an amorphous drug rich environment, the LNG theory appears to describe the melting process properly. Indeed, in this case, nanocrystals melting occurs in contact with a conspicuous drug liquid phase as, regardless of nanocrystal size, melting occurs at a higher temperature than the glass transition temperature of the amorphous drug, a value over which the amorphous drug is liquid and able to flow. Accordingly, it appears reasonable to presume that, when melting occurs, the thickness of the liquid layer surrounding the solid core is no longer negligible in comparison to the solid core one.

2.2. Mathematical Frame

The starting point for the three melting mechanisms is the definition of the infinitesimal reversible variation of the internal energy (E) for a closed system composed of k components and three phases (s solid, l liquid, v vapor) (Adamson and Gast, 1997):

$$dE = dE^{s} + dE^{l} + dE^{v} + dE^{sv} + dE^{lv} \qquad \text{HM} \tag{2.1a}$$

$$dE = dE^{s} + dE^{l} + dE^{v} + dE^{sl} + dE^{lv} \qquad \text{LNG/LSM} \tag{2.1b}$$

where $E^{s}, E^{l}, E^{v}, E^{sv}, E^{sl}$, and E^{lv} represent the solid, liquid, vapor, solid/vapor, solid/liquid, and liquid/vapor phase internal energy, respectively. The expressions of the internal energy for the bulk and interfacial phases are given, respectively, by:

$$dE^{b} = T^{b}dS^{b} + \sum_{i=1}^{k} \mu_{i}^{b} dn_{i}^{b} - P^{b}dV^{b} \tag{2.2}$$

$$dE^{f} = T^{f}dS^{f} + \sum_{i=1}^{k} \mu_{i}^{f} dn_{i}^{f} + \gamma^{f}dA^{f} + C_{1}^{f}dc_{1}^{f} + C_{2}^{f}dc_{2}^{f} \tag{2.3}$$

where the superscript "b" stands for bulk phase "s, l, or v", the superscript "f" stands for interfacial phase "sv, sl, or lv", T is temperature, S is entropy, μ_{i} and n_{i} are, respectively, the chemical potential and the number of moles of the i-th component in each bulk/interfacial phase, P is pressure, V is volume, γ^{f} and A^{f} are, respectively, the surface tension and the area of the interface f, c_{1}^{f} and c_{2}^{f} are the first and the second curvature referring to the interface f, while C_{1}^{f} and C_{2}^{f} are the related constants. In order to transform eqs 2.1a and 2.1b into an operative model able to relate T_{m} to crystal radius, some hypotheses are required (Adamson and Gast, 1997):

a) the contribution of the first and the second curvature to the system internal energy is negligible (this is strictly true for planes and spheres);
b) the system composed of the solid, liquid, and vapor phases is closed (no matter or energy exchanges with the surroundings, i.e. system volume, entropy, and moles number are constant);
c) thermal and chemical equilibrium is attained among the bulk and surface phases (same temperature and chemical potential for all components in all bulk and surface phases).

Accordingly, eqs 2.1a and 2.1b may be rewritten as:

$$dE = -P^{s}dV^{s} - P^{l}dV^{l} - P^{v}dV^{v} + \gamma^{sv}dA^{sv} + \gamma^{lv}dA^{lv} \qquad \text{HM} \tag{2.4a}$$

$$dE = -P^{s}dV^{s} - P^{l}dV^{l} - P^{v}dV^{v} + \gamma^{sl}dA^{sl} + \gamma^{lv}dA^{lv} \qquad \text{LNG/LSM} \tag{2.4b}$$

By remembering the closed system condition (hypothesis (b): $dV^{s} + dV^{l} + dV^{v} = 0$), the first three terms of eqs 2.4a and 2.4b right-hand sides become:

$$-P^{s}dV^{s} - P^{l}dV^{l} + P^{v}\left(dV^{s} + dV^{l}\right) = \left(P^{v} - P^{s}\right)dV^{s} + \left(P^{v} - P^{l}\right)dV^{l} \qquad \text{HM} \tag{2.5a}$$

$$-P^{s}\mathrm{d}V^{s}+P^{l}\left(\mathrm{d}V^{s}+\mathrm{d}V^{v}\right)-P^{v}\mathrm{d}V^{v}=\left(P^{l}-P^{s}\right)\mathrm{d}V^{s}+\left(P^{l}-P^{v}\right)\mathrm{d}V^{v} \qquad \text{LNG/LSM} \qquad (2.5b)$$

Therefore, eqs 2.4a and 2.4b may be rewritten as:

$$\mathrm{d}E=\left(P^{v}-P^{s}\right)\mathrm{d}V^{s}+\left(P^{v}-P^{l}\right)\mathrm{d}V^{l}+\gamma^{sv}\mathrm{d}A^{sv}+\gamma^{lv}\mathrm{d}A^{lv} \qquad \text{HM} \qquad (2.6a)$$

$$\mathrm{d}E=\left(P^{l}-P^{s}\right)\mathrm{d}V^{s}+\left(P^{l}-P^{v}\right)\mathrm{d}V^{v}+\gamma^{sl}\mathrm{d}A^{sl}+\gamma^{lv}\mathrm{d}A^{lv} \qquad \text{LNG/LSM} \qquad (2.6b)$$

The condition of minimal energy ($\mathrm{d}E=0$) allows establishing the mechanical equilibrium among phases:

$$P^{s}-P^{v}=\gamma^{sv}\frac{\mathrm{d}A^{sv}}{\mathrm{d}V^{s}} \qquad (2.7)$$

$$P^{l}-P^{v}=\gamma^{lv}\frac{\mathrm{d}A^{lv}}{\mathrm{d}V^{l}} \qquad (2.8)$$

$$P^{s}-P^{l}=\gamma^{sl}\frac{\mathrm{d}A^{sl}}{\mathrm{d}V^{s}} \qquad (2.9)$$

$$P^{v}-P^{l}=\gamma^{lv}\frac{\mathrm{d}A^{lv}}{\mathrm{d}V^{v}} \qquad (2.10)$$

or in differential terms:

$$\mathrm{d}P^{s}=\mathrm{d}P^{v}+\mathrm{d}\left(\gamma^{sv}\frac{\mathrm{d}A^{sv}}{\mathrm{d}V^{s}}\right) \qquad (2.11)$$

$$\mathrm{d}P^{l}=\mathrm{d}P^{v}+\mathrm{d}\left(\gamma^{lv}\frac{\mathrm{d}A^{lv}}{\mathrm{d}V^{l}}\right) \qquad (2.12)$$

$$\mathrm{d}P^{s}=\mathrm{d}P^{l}+\mathrm{d}\left(\gamma^{sl}\frac{\mathrm{d}A^{sl}}{\mathrm{d}V^{s}}\right) \qquad (2.13)$$

$$\mathrm{d}P^{v}=\mathrm{d}P^{l}+\mathrm{d}\left(\gamma^{lv}\frac{\mathrm{d}A^{lv}}{\mathrm{d}V^{v}}\right) \qquad (2.14)$$

In the case of a system constituted by one component only (i.e. the focus of this work), Gibbs-Duhem's equations for the solid, liquid, and vapor phases become:

$$s^{s}\mathrm{d}T + \mathrm{d}\mu_1 - v^{s}\mathrm{d}P^{s} = 0 \qquad \text{solid} \tag{2.15}$$

$$s^{l}\mathrm{d}T + \mathrm{d}\mu_1 - v^{l}\mathrm{d}P^{l} = 0 \qquad \text{liquid} \tag{2.16}$$

$$s^{v}\mathrm{d}T + \mathrm{d}\mu_1 - v^{v}\mathrm{d}P^{v} = 0 \qquad \text{vapor} \tag{2.17}$$

where s and v represent the molar entropy and volume referred to each bulk phase (solid, liquid, and vapor), while μ_1 is the chemical potential of the only component constituting the three bulk phases (solid, liquid, and vapor). By subtracting eq 2.16 from eq 2.15 and eq 2.17 from eqs 2.15 and 2.16 leads to:

$$\left(s^{s} - s^{l}\right)\mathrm{d}T - v^{s}\mathrm{d}P^{s} + v^{l}\mathrm{d}P^{l} = 0 \tag{2.18}$$

$$\left(s^{s} - s^{v}\right)\mathrm{d}T - v^{s}\mathrm{d}P^{s} + v^{v}\mathrm{d}P^{v} = 0 \tag{2.19}$$

$$\left(s^{l} - s^{v}\right)\mathrm{d}T - v^{l}\mathrm{d}P^{l} + v^{v}\mathrm{d}P^{v} = 0 \tag{2.20}$$

Equations 2.13 and 2.14 insertion into eqs 2.18 and 2.20 yields to:

$$\mathrm{d}P^{l} = \frac{s^{s} - s^{l}}{v^{s} - v^{l}}\mathrm{d}T - \frac{v^{s}}{v^{s} - v^{l}}\mathrm{d}\left(\gamma^{sl}\frac{\mathrm{d}A^{sl}}{\mathrm{d}V^{s}}\right) \tag{2.21}$$

$$\mathrm{d}P^{l} = \frac{s^{l} - s^{v}}{v^{l} - v^{v}}\mathrm{d}T + \frac{v^{v}}{v^{l} - v^{v}}\mathrm{d}\left(\gamma^{lv}\frac{\mathrm{d}A^{lv}}{\mathrm{d}V^{v}}\right) \tag{2.22}$$

Then, eqs 2.11 and 2.12 insertion into eqs 2.19 and 2.20 leads to:

$$\mathrm{d}P^{v} = \frac{s^{s} - s^{v}}{v^{s} - v^{v}}\mathrm{d}T - \frac{v^{s}}{v^{s} - v^{v}}\mathrm{d}\left(\gamma^{sv}\frac{\mathrm{d}A^{sv}}{\mathrm{d}V^{s}}\right) \tag{2.23}$$

$$\mathrm{d}P^{v} = \frac{s^{l} - s^{v}}{v^{l} - v^{v}}\mathrm{d}T - \frac{v^{l}}{v^{l} - v^{v}}\mathrm{d}\left(\gamma^{lv}\frac{\mathrm{d}A^{lv}}{\mathrm{d}V^{l}}\right) \tag{2.24}$$

By equating the right-hand side term of eq 2.23 with that of eq 2.24 and doing the same for eqs 2.21 and 2.22 yield to:

$$\left(\frac{s^{s} - s^{v}}{v^{s} - v^{v}} - \frac{s^{l} - s^{v}}{v^{l} - v^{v}}\right)\mathrm{d}T = \frac{v^{s}}{v^{s} - v^{v}}\mathrm{d}\left(\gamma^{sv}\frac{\mathrm{d}A^{sv}}{\mathrm{d}V^{s}}\right) - \frac{v^{l}}{v^{l} - v^{v}}\mathrm{d}\left(\gamma^{lv}\frac{\mathrm{d}A^{lv}}{\mathrm{d}V^{l}}\right) \qquad \text{HM} \tag{2.25a}$$

$$\left(\frac{s^{s}-s^{l}}{v^{s}-v^{l}}-\frac{s^{l}-s^{v}}{v^{l}-v^{v}}\right)\mathrm{d}T=\frac{v^{s}}{v^{s}-v^{l}}\mathrm{d}\left(\gamma^{sl}\frac{\mathrm{d}A^{sl}}{\mathrm{d}V^{s}}\right)-\frac{v^{v}}{v^{v}-v^{l}}\mathrm{d}\left(\gamma^{lv}\frac{\mathrm{d}A^{lv}}{\mathrm{d}V^{v}}\right) \qquad \text{LNG/LSM} \qquad (2.25b)$$

Equations 2.25a and 2.25b connect triple point temperature variation with interfacial properties. By further defining the difference ($s^{l}-s^{s}$) as the molar melting entropy $\Delta s_{m}=\Delta h_{m}/T_{m}$, the working equation connecting T_{m} with the molar melting enthalpy (Δh_{m}) is obtained:

$$\Delta h_{m}\frac{\mathrm{d}T_{m}}{T_{m}}=v^{l}\mathrm{d}\left(\gamma^{lv}\frac{\mathrm{d}A^{lv}}{\mathrm{d}V^{l}}\right)-v^{s}\mathrm{d}\left(\gamma^{sv}\frac{\mathrm{d}A^{sv}}{\mathrm{d}V^{s}}\right) \qquad \text{HM} \qquad (2.26a)$$

as v^{s} and v^{l} may be supposed to be negligible in comparison to v^{v} (Brun et al., 1973), and:

$$\Delta h_{m}\frac{\mathrm{d}T_{m}}{T_{m}}=\left(v^{s}-v^{l}\right)\mathrm{d}\left(\gamma^{lv}\frac{\mathrm{d}A^{lv}}{\mathrm{d}V^{v}}\right)-v^{s}\mathrm{d}\left(\gamma^{sl}\frac{\mathrm{d}A^{sl}}{\mathrm{d}V^{s}}\right) \qquad \text{LNG/LSM} \qquad (2.26b)$$

since $\left|\frac{s^{l}-s^{v}}{v^{l}-v^{v}}\right|<<\left|\frac{s^{s}-s^{l}}{v^{s}-v^{l}}\right|$ and $\frac{v^{v}}{v^{v}-v^{l}}\approx 1$.

If the specific melting enthalpy is referred to the unit mass (ΔH_{m}), eqs 2.26a and 2.26b become:

$$\Delta H_{m}\frac{\mathrm{d}T_{m}}{T_{m}}=\frac{1}{\rho_{l}}\mathrm{d}\left(\gamma^{lv}\frac{\mathrm{d}A^{lv}}{\mathrm{d}V^{l}}\right)-\frac{1}{\rho_{s}}\mathrm{d}\left(\gamma^{sv}\frac{\mathrm{d}A^{sv}}{\mathrm{d}V^{s}}\right) \qquad \text{HM} \qquad (2.27a)$$

$$\Delta H_{m}\frac{\mathrm{d}T_{m}}{T_{m}}=\left(\frac{1}{\rho_{s}}-\frac{1}{\rho_{l}}\right)\mathrm{d}\left(\gamma^{lv}\frac{\mathrm{d}A^{lv}}{\mathrm{d}V^{v}}\right)-\frac{1}{\rho_{s}}\mathrm{d}\left(\gamma^{sl}\frac{\mathrm{d}A^{sl}}{\mathrm{d}V^{s}}\right) \qquad \text{LNG/LSM} \qquad (2.27b)$$

where ρ_{s} and ρ_{l} are, respectively, the solid and liquid phases density.

Equations 2.27a and 2.27b should be adapted to consider the different geometrical shapes (sphere, cylinder, parallelepiped) chosen to approximate crystals shape. In particular, this adaptation regards the derivatives $\mathrm{d}A^{lv}/\mathrm{d}V^{l}$, $\mathrm{d}A^{sv}/\mathrm{d}V^{s}$, $\mathrm{d}A^{lv}/\mathrm{d}V^{v}$, and $\mathrm{d}A^{sl}/\mathrm{d}V^{s}$. Interestingly, by assuming that ρ_{s} and ρ_{l} are equal, considering spherical crystals, remembering Young's equation for a pure substance ($\gamma^{sl}+\gamma^{lv}=\gamma^{sv}$) (Adamson and Gast 1997), regarding γ^{sl} and γ^{lv} as independent of curvature and ΔH_{m} as independent of temperature, the integration of eqs 2.27a and 2.27b returns the well-known Gibbs-Thomson's equation (Gibbs, 1928; Ha et al., 2005):

$$\frac{\Delta T_{m}}{T_{m}}=-\frac{4\gamma^{sl}}{\rho_{s}\Delta H_{m}d}\cos(\theta) \qquad (2.28)$$

where d is crystal diameter and θ represents the contact angle of the solid nanocrystal with the pore wall in the case of crystals confined in nanopores. In the case of unconfined nanocrystals (i.e. the situation considered in this work), $\cos(\theta) = -1$ ($\theta = 180°$).

In the following sections, eq 2.27b is particularized for differently shaped nanocrystals (sphere, parallelepiped, and cylinder). Although the same procedure may be also performed for eq 2.27a, it was decided not to consider that approach on the basis of the reasons exposed in the last part of section 2.1 and owing to the feeling that eq 2.27b is more general than eq 2.27a. Indeed, if no hypotheses are attempted on the spatial disposition of the three bulk phases, the infinitesimal reversible variation of the internal energy (E) becomes:

$$\mathrm{d}E = \mathrm{d}E^{\mathrm{s}} + \mathrm{d}E^{\mathrm{l}} + \mathrm{d}E^{\mathrm{v}} + \mathrm{d}E^{\mathrm{sv}} + \mathrm{d}E^{\mathrm{sl}} + \mathrm{d}E^{\mathrm{lv}} \tag{2.29}$$

Equation 2.29 manipulation according to the same hypotheses and procedures applied to eq 2.1a and eq 2.1b leads to the following expression:

$$\mathrm{d}E = -P^{\mathrm{v}}\mathrm{d}V^{\mathrm{v}} - P^{\mathrm{s}}\mathrm{d}V^{\mathrm{s}} - P^{\mathrm{l}}\mathrm{d}V^{\mathrm{l}} + \gamma^{\mathrm{sv}}\mathrm{d}A^{\mathrm{sv}} + \gamma^{\mathrm{sl}}\mathrm{d}A^{\mathrm{sl}} + \gamma^{\mathrm{lv}}\mathrm{d}A^{\mathrm{lv}} \tag{2.30}$$

The closed system hypothesis allows concluding that the first three terms of eq 2.30 right-hand side become:

$$-P^{\mathrm{v}}\mathrm{d}V^{\mathrm{v}} + P^{\mathrm{s}}\left(\mathrm{d}V^{\mathrm{l}} + \mathrm{d}V^{\mathrm{v}}\right) - P^{\mathrm{l}}\mathrm{d}V^{\mathrm{l}} = \mathrm{d}V^{\mathrm{v}}\left(P^{\mathrm{s}} - P^{\mathrm{v}}\right) + \mathrm{d}V^{\mathrm{l}}\left(P^{\mathrm{s}} - P^{\mathrm{l}}\right) \tag{2.31}$$

By substituting the pressure drop between the solid and vapor phases ($P^{\mathrm{s}} - P^{\mathrm{v}}$) with the obvious relation ($P^{\mathrm{s}} - P^{\mathrm{v}} = P^{\mathrm{s}} - P^{\mathrm{l}} + P^{\mathrm{l}} - P^{\mathrm{v}}$), eq 2.31 becomes:

$$\mathrm{d}V^{\mathrm{v}}\left(P^{\mathrm{s}} - P^{\mathrm{l}}\right) + \mathrm{d}V^{\mathrm{v}}\left(P^{\mathrm{l}} - P^{\mathrm{v}}\right) + \mathrm{d}V^{\mathrm{l}}\left(P^{\mathrm{s}} - P^{\mathrm{l}}\right) = -\mathrm{d}V^{\mathrm{s}}\left(P^{\mathrm{s}} - P^{\mathrm{l}}\right) + \mathrm{d}V^{\mathrm{v}}\left(P^{\mathrm{l}} - P^{\mathrm{v}}\right) \tag{2.32}$$

By introducing eq 2.32 into eq 2.30 and remembering Young's equation for a pure substance ($\gamma^{\mathrm{sl}} + \gamma^{\mathrm{lv}} = \gamma^{\mathrm{sv}}$) (Adamson and Gast, 1997), the following relation is obtained:

$$\mathrm{d}E = -\mathrm{d}V^{\mathrm{s}}\left(P^{\mathrm{s}} - P^{\mathrm{l}}\right) + \mathrm{d}V^{\mathrm{v}}\left(P^{\mathrm{l}} - P^{\mathrm{v}}\right) + \gamma^{\mathrm{sl}}\mathrm{d}\left(A^{\mathrm{sl}} + A^{\mathrm{sv}}\right) + \gamma^{\mathrm{lv}}\mathrm{d}\left(A^{\mathrm{lv}} + A^{\mathrm{sv}}\right) \tag{2.33}$$

The minimal energy condition ($\mathrm{d}E = 0$) allows establishing the mechanical equilibrium ones:

$$\left(P^{\mathrm{s}} - P^{\mathrm{l}}\right) = \gamma^{\mathrm{sl}}\frac{\mathrm{d}\left(A^{\mathrm{sl}} + A^{\mathrm{sv}}\right)}{\mathrm{d}V^{\mathrm{s}}} = \gamma^{\mathrm{sl}}\frac{\mathrm{d}A^{\mathrm{s}}}{\mathrm{d}V^{\mathrm{s}}} \tag{2.34}$$

$$\left(P^{\mathrm{v}} - P^{\mathrm{l}}\right) = \gamma^{\mathrm{lv}}\frac{\mathrm{d}\left(A^{\mathrm{lv}} + A^{\mathrm{sv}}\right)}{\mathrm{d}V^{\mathrm{v}}} = \gamma^{\mathrm{lv}}\frac{\mathrm{d}A^{\mathrm{v}}}{\mathrm{d}V^{\mathrm{v}}} \tag{2.35}$$

or, in differential terms:

$$\mathrm{d}P^{\mathrm{s}} = \mathrm{d}P^{\mathrm{l}} + \mathrm{d}\left(\gamma^{\mathrm{sl}} \frac{\mathrm{d}A^{\mathrm{s}}}{\mathrm{d}V^{\mathrm{s}}} \right) \tag{2.36}$$

$$\mathrm{d}P^{\mathrm{v}} = \mathrm{d}P^{\mathrm{l}} + \mathrm{d}\left(\gamma^{\mathrm{lv}} \frac{\mathrm{d}A^{\mathrm{v}}}{\mathrm{d}V^{\mathrm{v}}} \right) \tag{2.37}$$

where A^{s} and A^{v} are, respectively, the area of the solid and vapor interfaces. By introducing eqs 2.36 and 2.37 into Gibbs-Duhem's equations (eqs 2.18 and 2.20), the following ones are obtained:

$$\mathrm{d}P^{\mathrm{l}} = \left(\frac{s^{\mathrm{s}} - s^{\mathrm{l}}}{v^{\mathrm{s}} - v^{\mathrm{l}}} \right) \mathrm{d}T - \left(\frac{v^{\mathrm{s}}}{v^{\mathrm{s}} - v^{\mathrm{l}}} \right) \mathrm{d}\left(\gamma^{\mathrm{sl}} \frac{\mathrm{d}A^{\mathrm{s}}}{\mathrm{d}V^{\mathrm{s}}} \right) \tag{2.38}$$

$$\mathrm{d}P^{\mathrm{l}} = \left(\frac{s^{\mathrm{l}} - s^{\mathrm{v}}}{v^{\mathrm{l}} - v^{\mathrm{v}}} \right) \mathrm{d}T + \left(\frac{v^{\mathrm{v}}}{v^{\mathrm{l}} - v^{\mathrm{v}}} \right) \mathrm{d}\left(\gamma^{\mathrm{lv}} \frac{\mathrm{d}A^{\mathrm{v}}}{\mathrm{d}V^{\mathrm{v}}} \right) \tag{2.39}$$

Equating the right-hand side terms of eqs (2.38) – (2.39) and rearranging them lead to:

$$\left(\frac{s^{\mathrm{s}} - s^{\mathrm{l}}}{v^{\mathrm{s}} - v^{\mathrm{l}}} - \frac{s^{\mathrm{l}} - s^{\mathrm{v}}}{v^{\mathrm{l}} - v^{\mathrm{v}}} \right) \mathrm{d}T = \left(\frac{v^{v}}{v^{\mathrm{l}} - v^{\mathrm{v}}} \right) \mathrm{d}\left(\gamma^{\mathrm{lv}} \frac{\mathrm{d}A^{\mathrm{v}}}{\mathrm{d}V^{\mathrm{v}}} \right) + \left(\frac{v^{\mathrm{s}}}{v^{\mathrm{s}} - v^{\mathrm{l}}} \right) \mathrm{d}\left(\gamma^{\mathrm{sl}} \frac{\mathrm{d}A^{\mathrm{s}}}{\mathrm{d}V^{\mathrm{s}}} \right) \tag{2.40}$$

By proceeding as for eqs 2.26a and 2.26b (ν^{l} and ν^{s} negligible compared with ν^{v}), eq 2.40 becomes:

$$\Delta h_{\mathrm{m}} \frac{\mathrm{d}T_{\mathrm{m}}}{T_{\mathrm{m}}} = \left(v^{\mathrm{s}} - v^{\mathrm{l}} \right) \mathrm{d}\left(\gamma^{\mathrm{lv}} \frac{\mathrm{d}A^{\mathrm{v}}}{\mathrm{d}V^{\mathrm{v}}} \right) - v^{\mathrm{s}} \mathrm{d}\left(\gamma^{\mathrm{sl}} \frac{\mathrm{d}A^{\mathrm{s}}}{\mathrm{d}V^{\mathrm{s}}} \right) \tag{2.41}$$

or, if the specific enthalpy per unit mass is considered (ΔH_{m}):

$$\Delta H_{\mathrm{m}} \frac{\mathrm{d}T_{\mathrm{m}}}{T_{\mathrm{m}}} = \left(\frac{1}{\rho_{\mathrm{s}}} - \frac{1}{\rho_{\mathrm{l}}} \right) \mathrm{d}\left(\gamma^{\mathrm{lv}} \frac{\mathrm{d}A^{\mathrm{v}}}{\mathrm{d}V^{\mathrm{v}}} \right) - \frac{1}{\rho_{\mathrm{s}}} \mathrm{d}\left(\gamma^{\mathrm{sl}} \frac{\mathrm{d}A^{\mathrm{s}}}{\mathrm{d}V^{\mathrm{s}}} \right) \tag{2.42}$$

It is easy to verify that eq 2.42 coincides with eq 2.27b when A^{v} and A^{s} are replaced, respectively, with A^{lv} and A^{sl}, i.e. the physical meaning of the vapor and solid interfaces when the phases disposition is the one assumed by the LNG/LSM mechanisms.

2.2.1. Spheres

By assuming crystals to be spherical (see Figure 2.1), it is possible to evaluate the two derivatives

dA^{lv}/dV^{v} and dA^{sl}/dV^{s} required by eq 2.27b:

$$\frac{dA^{lv}}{dV^{v}} = \frac{d\left(4\pi R_l^2\right)}{d\left(\frac{4}{3}\pi R_v^3 - \frac{4}{3}\pi R_l^3\right)} = -\frac{8\pi R_l dR_l}{4\pi R_l^2 dR_l} = -\frac{2}{R_l} \tag{2.2.1.1}$$

$$\frac{dA^{sl}}{dV^{s}} = \frac{d\left(4\pi R_s^2\right)}{d\left(\frac{4}{3}\pi R_s^3\right)} = \frac{8\pi R_s dR_s}{4\pi R_s^2 dR_s} = \frac{2}{R_s} \tag{2.2.1.2}$$

where R_s, R_l, and R_v represent the radius of the solid, liquid, and vapor phases, respectively. While performing the two derivatives, the volume ($\frac{4}{3}\pi R_v^3$) is assumed constant. Moreover, Tolman's equation was considered to take into account the surface energy dependence on surface curvature (Tolman, 1949; Samsonov et al., 2004; Lu et al., 2007; Jiang et al., 1999):

$$\frac{\gamma}{\gamma_\infty} = \left(1 + \frac{2\delta_0}{r}\right)^{-1} \tag{2.2.1.3}$$

where γ and γ_∞ are the energy of a surface with curvature radius r and that of a flat surface (infinite curvature radius), respectively, while δ_0 is Tolman's length whose order of magnitude should correspond to the actual diameter (d_m) of the molecules constituting the bulk phase and is usually assumed to be $d_m/3$ (Rowlinson and Windom, 1982). Equation 2.2.1.3 predicts that surface energy tends to zero for low values of r. Thus, according to eqs 2.2.1.1 – 2.2.1.3, eq 2.27b becomes:

$$\Delta H_m \frac{dT_m}{T_m} = -2\left[\left(\frac{1}{\rho_s} - \frac{1}{\rho_l}\right) d\left(\frac{\gamma_\infty^{lv}}{R_l + 2\delta_0}\right) + \frac{1}{\rho_s} d\left(\frac{\gamma_\infty^{sl}}{R_s + 2\delta_0}\right)\right] \tag{2.2.1.4}$$

where γ_∞^{lv} and γ_∞^{sl} are the surface energy of the plane liquid/vapor and solid/liquid interfaces, respectively.

It is now necessary to express the dependence of R_l on R_s by adopting the strategy conceived by Coceani (Coceani et al., 2012). This approach relies on the fact that, very often, drug nanocrystals melting occurs in the presence of the amorphous drug that becomes liquid considerably before them. Indeed, as the glass transition temperature of the amorphous drug is lower than nanocrystals melting temperature, the amorphous drug will be liquid before nanocrystals melting. Thus, at the melting point, X_{nc} (drug nanocrystals mass/drug total mass) may be evaluated as:

$$X_{nc} = \frac{\frac{4}{3}\pi R_s^3 \rho_s}{\frac{4}{3}\pi R_s^3 \rho_s + \frac{4}{3}\pi \rho_l \left(R_l^3 - R_s^3\right)} = \frac{R_s^3 \rho_s}{R_s^3 \rho_s + \rho_l \left(R_l^3 - R_s^3\right)} \tag{2.2.1.5}$$

Equation 2.2.1.5 allows obtaining the following parameter representing the ratio between R_l and R_s:

$$\alpha = \frac{R_l}{R_s} = \sqrt[3]{\frac{\rho_s}{\rho_l}\left(\frac{1-X_{nc}}{X_{nc}}\right)+1} \tag{2.2.1.6}$$

Obviously, while eq 2.2.1.5 strictly holds for a monodispersed nanocrystals size distribution, it on average holds for a polydispersed one. It is easy to verify that the LSM condition occurs when X_{nc} tends to 1 (the amorphous/liquid phase is virtually absent; $R_l \approx R_s$), while the LNG condition takes place for X_{nc} near 0 (nanocrystals melting occurs in a virtually infinite liquid phase; $R_l \approx \infty$). Thus, eq 2.2.1.4 may be rewritten as:

$$\Delta H_m \frac{dT_m}{T_m} = -2\left[\left(\frac{1}{\rho_s}-\frac{1}{\rho_l}\right)d\left(\frac{\gamma_\infty^{lv}}{\alpha R_s + 2\delta_0}\right)+\frac{1}{\rho_s}d\left(\frac{\gamma_\infty^{sl}}{R_s+2\delta_0}\right)\right] \tag{2.2.1.7}$$

By assuming both ρ_s and ρ_l constant and independent of R_s, the integration of eq 2.2.1.7 between the melting temperature of the infinite radius crystal ($T_{m\infty}$) and the melting temperature of the one with radius R_s (T_m) allows finding the working equation holding for spheres:

$$\int_{T_{m\infty}}^{T_m} \Delta H_m \frac{dT_m}{T_m} = -2\left[\left(\frac{1}{\rho_s}-\frac{1}{\rho_l}\right)\frac{\gamma_\infty^{lv}}{\alpha R_s + 2\delta_0}+\frac{1}{\rho_s}\left(\frac{\gamma_\infty^{sl}}{R_s+2\delta_0}\right)\right] \tag{2.2.1.8}$$

In order to solve eq 2.2.1.8 and obtain T_m dependence on R_s, it is necessary to evaluate ΔH_m dependence on T_m (see the integral in eq 2.2.1.8). In this context, the classic thermodynamic approach employed by Zhang and co-workers, holding regardless of nanocrystals nature (organic or inorganic) and being characterized by easily determinable parameters, may be considered (Zhang et al., 2000). This approach relies on a thermodynamic cycle (see Figure 2.2) according to which ΔH_m is calculated as the sum of five different contributions. The first is due to the aggregation of nanospheres with radius R_s into the bulk phase at nanocrystals melting temperature T_m (ΔH_1). In performing the evaluation of ΔH_1, the surface energy of the bulk phase is implicitly assumed to be negligible in comparison to the original nanospheres one as the bulk phase surface is vanishingly small compared to that of nanospheres. The second implies the bulk phase heating from T_m to the infinitely large crystal melting temperature $T_{m\infty}$ (ΔH_2), while the third represents the bulk phase melting at $T_{m\infty}$ (ΔH_3). The fourth implies the bulk liquid disintegration into liquid nanospheres with radius R_s at $T_{m\infty}$ (ΔH_4). Similarly, as in the aggregation of nanospheres (step 1), the surface energy of the bulk liquid phase is considered negligible in comparison to that of liquid

nanodrops. Finally, the fifth is the cooling of liquid nanodrops from $T_{m\infty}$ to nanocrystals melting temperature T_m (ΔH_5):

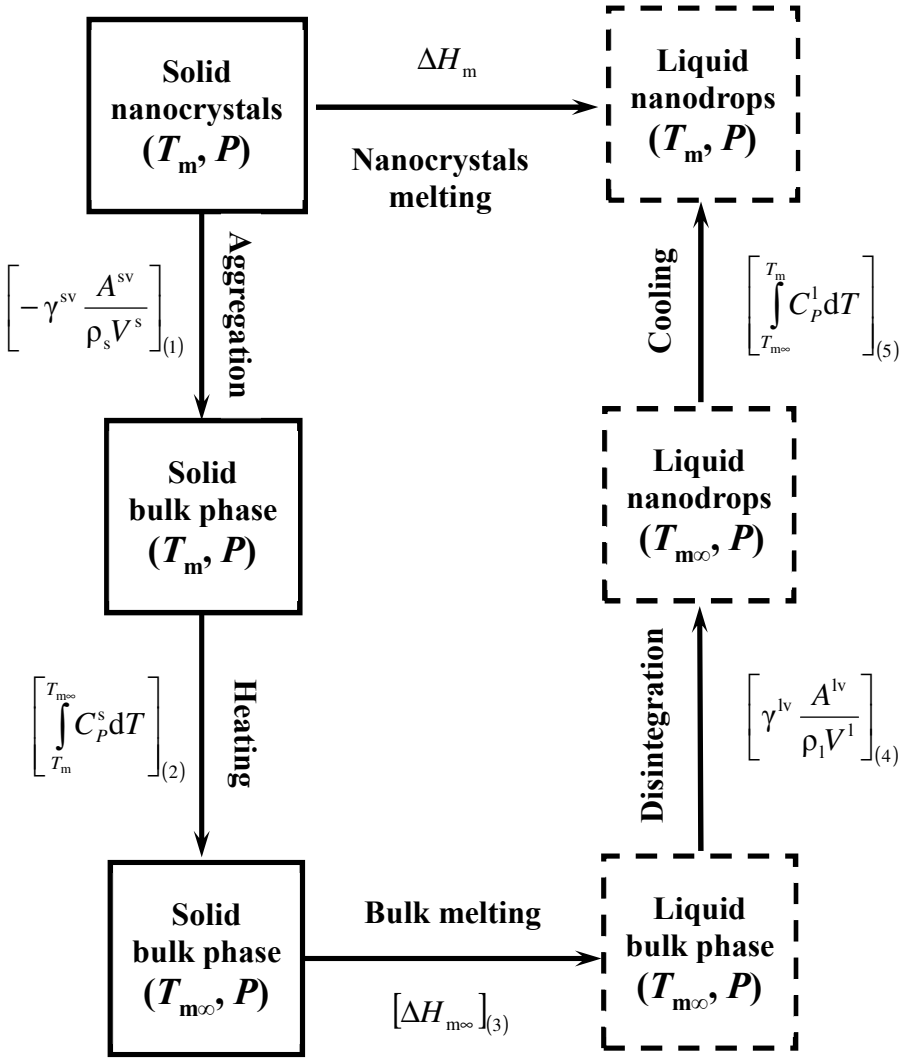

Figure 2.2. Thermodynamic cycle employed to derive eq 2.2.1.9. T is absolute temperature, P is pressure, T_m and ΔH_m are, respectively, nanocrystals melting temperature and enthalpy, $T_{m\infty}$ and $\Delta H_{m\infty}$ are, respectively, macrocrystals melting temperature and enthalpy, V^s and A^{sv} are, respectively, solid phase volume and area of the solid-vapor interface referring to the ensemble of spheres with radius R_s, V^l and A^{lv} are, respectively, liquid phase volume and area of the liquid-vapor interface referring to the ensemble of spheres with radius R_s, γ^{sv} and γ^{lv} are, respectively, solid-vapor and liquid-vapor interface energies, C_P^s and C_P^l are, respectively, specific heat at constant pressure relative to solid and liquid phases, while ρ_s and ρ_l are, respectively, density of the solid and liquid phases.

$$\Delta H_m = \left[-\gamma^{sv}\frac{A^{sv}}{\rho_s V^s}\right]_{(1)} + \left[\int_{T_m}^{T_{m\infty}} C_P^s dT\right]_{(2)} + [\Delta H_{m\infty}]_{(3)} + \left[\gamma^{lv}\frac{A^{lv}}{\rho_l V^l}\right]_{(4)} + \left[\int_{T_{m\infty}}^{T_m} C_P^l dT\right]_{(5)} \qquad (2.2.1.9)$$

where $\Delta H_{m\infty}$ is the specific melting enthalpy of an infinitely large crystal, V^s and A^{sv} are, respectively, the solid phase volume and the area of the solid-vapor interface referring to the ensemble of spheres with radius R_s, V^l and A^{lv} are, respectively, the liquid phase volume and the area of the liquid-vapor interface referring to the ensemble of spheres with radius R_s, while C_P^s and C_P^l are, respectively, the solid and liquid drug specific heat capacities at constant pressure. By remembering that $A^{sv}/V^s = 3/R_s$, $A^{lv}/V^l = 3/R_s$, γ^{sv} and γ^{lv} depend on surface curvature ($1/R_s$) according to Tolman's theory (eq 2.2.1.3), and the difference between C_P^s and C_P^l is almost temperature independent (Hasa et al., 2013), eq 2.2.1.9 finally reads:

$$\Delta H_m = \Delta H_{m\infty} - \frac{3}{R_s + 2\delta_0}\left(\frac{\gamma_\infty^{sv}}{\rho_s} - \frac{\gamma_\infty^{lv}}{\rho_l}\right) - \left(C_P^l - C_P^s\right)\left(T_{m\infty} - T_m\right) \tag{2.2.1.10}$$

where γ_∞^{sv} is the surface energy of the plane solid/vapor interface.

The melting properties dependence on nanospheres radius R_s ($T_m(R_s)$; $\Delta H_m(R_s)$) is achieved by the simultaneous numerical solution of eqs 2.2.1.8 and 2.2.1.10. By assuming that ΔH_m is constant in the temperature interval ($T_{m\infty}$; $T_{m1} = T_{m\infty} - \Delta T$), eq 2.2.1.8 reads:

$$\int_{T_{m\infty}}^{T_{m1}} \Delta H_m \frac{dT_m}{T_m} \approx \Delta H_{m1} \ln\left(T_{m1}/T_{m\infty}\right) \approx -2\left[\left(\frac{1}{\rho_s} - \frac{1}{\rho_l}\right)\frac{\gamma_\infty^{lv}}{\alpha R_{s1} + 2\delta_0} + \frac{1}{\rho_s}\left(\frac{\gamma_\infty^{sl}}{R_{s1} + 2\delta_0}\right)\right] \tag{2.2.1.11}$$

Consequently, the first estimation of ΔH_{m1} according to eq 2.2.1.11 is:

$$\Delta H_{m1} = -\frac{2}{\ln\left(T_{m1}/T_{m\infty}\right)}\left[\left(\frac{1}{\rho_s} - \frac{1}{\rho_l}\right)\frac{\gamma_\infty^{lv}}{\alpha R_{s1} + 2\delta_0} + \frac{1}{\rho_s}\left(\frac{\gamma_\infty^{sl}}{R_{s1} + 2\delta_0}\right)\right] \tag{2.2.1.12}$$

By equating this ΔH_{m1} estimation to the Zhang's one (eq 2.2.1.10), it is possible to determine the value of R_{s1} related to T_{m1}:

$$\begin{aligned} &-\frac{2}{\ln\left(T_{m1}/T_{m\infty}\right)}\left[\left(\frac{1}{\rho_s} - \frac{1}{\rho_l}\right)\frac{\gamma_\infty^{lv}}{\alpha R_{s1} + 2\delta_0} + \frac{1}{\rho_s}\left(\frac{\gamma_\infty^{sl}}{R_{s1} + 2\delta_0}\right)\right] = \\ &= \Delta H_{m\infty} - \frac{3}{R_{s1} + 2\delta_0}\left(\frac{\gamma_\infty^{sv}}{\rho_s} - \frac{\gamma_\infty^{lv}}{\rho_l}\right) - \left(C_P^l - C_P^s\right)\left(T_{m\infty} - T_{m1}\right) \end{aligned} \tag{2.2.1.13}$$

R_{s1} is determined according to Newton's method by assuming a relative tolerance of 10^{-6}. Once R_{s1} is known, ΔH_{m1} may be evaluated according to eq 2.2.1.8 or eq 2.2.1.10. By repeating the same strategy for further melting temperature reductions ($T_m - i\Delta T$), the following general equation for

R_{si} is achieved:

$$-\frac{1}{\ln\left(T_{mi}/T_{mi-1}\right)}\left[\left(\frac{1}{\rho_s}-\frac{1}{\rho_1}\right)\frac{2\gamma_\infty^{lv}}{\alpha R_{si}+2\delta_0}+\frac{1}{\rho_s}\left(\frac{2\gamma_\infty^{sl}}{R_{si}+2\delta_0}\right)+\sum_{j=1}^{i-1}\Delta H_{mj}\ln\left(T_{mj}/T_{mj-1}\right)\right]= \\ =\Delta H_{m\infty}-\frac{3}{R_{si}+2\delta_0}\left(\frac{\gamma_\infty^{sv}}{\rho_s}-\frac{\gamma_\infty^{lv}}{\rho_1}\right)-\left(C_P^1-C_P^s\right)\left(T_{m\infty}-T_{mi}\right) \tag{2.2.3.14}$$

Similarly, after finding R_{si}, ΔH_{mi} may be evaluated according to eq 2.2.1.8 or eq 2.2.1.10. In order to ensure the reliability of the numerical procedure, ΔT was set equal to 0.1 K.

2.2.2. Parallelepipeds

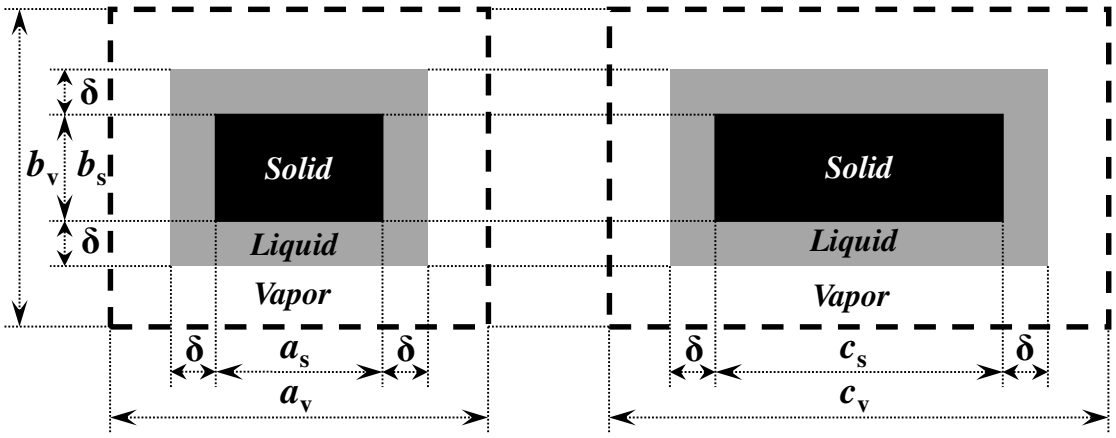

Figure 2.3. Spatial disposition of the three drug phases (solid, liquid, and vapor) according to the LNG and LSM theories. a_s, b_s, and c_s represent the three dimensions of the parallelepiped solid core, δ is the thickness of the surrounding liquid layer, while a_v, b_v, and c_v are the three dimensions of the vapor phase.

While it is reasonable and physically sound that, in the case of a spherical crystal, the liquid phase is represented by a spherical shell (see Figure 2.1), the shape assumed by the liquid phase around the solid parallelepiped, on the contrary, is less obvious. However, for the sake of simplicity, it is usual to assume that the shape of the liquid phase is the same as the solid one (Sar et al., 2008). Accordingly, Figure 2.3, borrowing, for a parallelepiped, the physical situation depicted in Figure 2.1, allows evaluating the analytical expression of the two derivatives dA^{lv}/dV^v and dA^{sl}/dV^s:

$$\frac{dA^{lv}}{dV^v}=\frac{d\left[2(a_s+2\delta)(b_s+2\delta)+2(a_s+2\delta)(c_s+2\delta)+2(b_s+2\delta)(c_s+2\delta)\right]}{d\left[a_v b_v c_v-(a_s+2\delta)(b_s+2\delta)(c_s+2\delta)\right]}= \\ =-\frac{4}{3a_s}\left(\frac{1}{1+2\Delta}+\frac{1}{\beta+2\Delta}+\frac{1}{\xi+2\Delta}\right) \tag{2.2.2.1}$$

$$\frac{dA^{sl}}{dV^{s}} = \frac{d\left(2a_s b_s + 2a_s c_s + 2b_s c_s\right)}{d\left(a_s b_s c_s\right)} = \frac{4}{3a_s}\left(1 + \frac{1}{\beta} + \frac{1}{\xi}\right) \tag{2.2.2.2}$$

where a_s, b_s, c_s, a_v, b_v, and c_v represent the three dimensions of the solid and vapor phases, respectively, δ is the thickness of the surrounding liquid layer, $\Delta = \delta/a_s$, $\beta = b_s/a_s$, and $\xi = c_s/a_s$. While performing the two derivatives, the volume ($a_v b_v c_v$) is assumed constant. Hence, by assuming that surface energy is the same for each parallelepiped face, eq 2.27b becomes:

$$\Delta H_m \frac{dT_m}{T_m} = -\left(\frac{1}{\rho_s} - \frac{1}{\rho_l}\right) d\left[\gamma_\infty^{lv} \frac{4}{3a_s}\left(\frac{1}{1+2\Delta} + \frac{1}{\beta+2\Delta} + \frac{1}{\xi+2\Delta}\right)\right] - \frac{1}{\rho_s} d\left[\gamma_\infty^{sl} \frac{4}{3a_s}\left(1 + \frac{1}{\beta} + \frac{1}{\xi}\right)\right] \tag{2.2.2.3}$$

In order to evaluate the ratio Δ, it is convenient to recall the definition of X_{nc} (drug nanocrystals mass/drug total mass):

$$X_{nc} = \frac{\rho_s a_s b_s c_s}{\rho_s a_s b_s c_s + \rho_l\left[(a_s + 2\delta)(b_s + 2\delta)(c_s + 2\delta) - a_s b_s c_s\right]} \tag{2.2.2.4}$$

Equation 2.2.2.4 inversion allows the determination of the function $\Delta(X_{nc})$:

$$\Delta^3 + \frac{1+\beta+\xi}{2}\Delta^2 + \frac{\beta+\beta\xi+\xi}{4}\Delta + \frac{\beta\xi\rho_s}{8\rho_l}\left(1 - \frac{1}{X_{nc}}\right) = 0 \tag{2.2.2.5}$$

The numerical solution of eq 2.2.2.5 (Newton's method) enables the evaluation of the parameter Δ required by eq 2.2.2.3. By assuming both ρ_s and ρ_l constant and independent of a_s, the integration of eq 2.2.2.3 from the melting temperature of the infinitely large crystal ($T_{m\infty}$) to the melting temperature of the nanocrystal with size a_s (T_m), allows finding the working equation holding for parallelepipeds:

$$\int_{T_{m\infty}}^{T_m} \Delta H_m \frac{dT_m}{T_m} = -\frac{4}{3a_s}\left[\gamma_\infty^{lv}\left(\frac{1}{\rho_s} - \frac{1}{\rho_l}\right)\left(\frac{1}{1+2\Delta} + \frac{1}{\beta+2\Delta} + \frac{1}{\xi+2\Delta}\right) + \frac{\gamma_\infty^{sl}}{\rho_s}\left(1 + \frac{1}{\beta} + \frac{1}{\xi}\right)\right] \tag{2.2.2.6}$$

Implicitly, eq 2.2.2.6 implies that surface energy (both γ_∞^{lv} and γ_∞^{sl}) is independent of crystal shape (β, ξ), dimension (a_s), and crystal facet. As a matter of fact, this assumption is sometimes unverified, as nicely documented by Heng and co-workers (Heng et al., 2006) who proved that paracetamol form I crystals exhibit different solid/vapor surface energies on distinct crystal facets. In this particular case, the explanation for this occurrence was the variable number of hydroxyl groups present on crystal facets. It is worth mentioning that, in principle, the derivation of eq 2.2.2.6 could also consider the surface energy dependence on crystal shape, dimension, and facet.

In particular, in order to take account of the surface energy dependence on crystal facet, eq 2.2.2.6 modification is relatively straightforward provided that the surface energy pertaining to each facet is available:

$$\int_{T\mathrm{m}\infty}^{T\mathrm{m}} \Delta H_{\mathrm{m}} \frac{\mathrm{d}T_{\mathrm{m}}}{T_{\mathrm{m}}} = -\frac{2}{3a_{\mathrm{s}}} \left\{ \left(\frac{1}{\rho_{\mathrm{s}}} - \frac{1}{\rho_{\mathrm{l}}} \right) \left[\left(\underbrace{\gamma_{\infty}^{\mathrm{lv}}}_{a_{\mathrm{s}}b_{\mathrm{s}}(\mathrm{I})} + \underbrace{\gamma_{\infty}^{\mathrm{lv}}}_{a_{\mathrm{s}}b_{\mathrm{s}}(\mathrm{II})} \right) \frac{1}{1+2\Delta} + \left(\underbrace{\gamma_{\infty}^{\mathrm{lv}}}_{a_{\mathrm{s}}c_{\mathrm{s}}(\mathrm{I})} + \underbrace{\gamma_{\infty}^{\mathrm{lv}}}_{a_{\mathrm{s}}c_{\mathrm{s}}(\mathrm{II})} \right) \frac{1}{\beta+2\Delta} + \left(\underbrace{\gamma_{\infty}^{\mathrm{lv}}}_{b_{\mathrm{s}}c_{\mathrm{s}}(\mathrm{I})} + \underbrace{\gamma_{\infty}^{\mathrm{lv}}}_{b_{\mathrm{s}}c_{\mathrm{s}}(\mathrm{II})} \right) \frac{1}{\xi+2\Delta} \right] + \right.$$
$$\left. + \frac{1}{\rho_{\mathrm{s}}} \left[\left(\underbrace{\gamma_{\infty}^{\mathrm{sl}}}_{a_{\mathrm{s}}b_{\mathrm{s}}(\mathrm{I})} + \underbrace{\gamma_{\infty}^{\mathrm{sl}}}_{a_{\mathrm{s}}b_{\mathrm{s}}(\mathrm{II})} \right) + \left(\underbrace{\gamma_{\infty}^{\mathrm{sl}}}_{a_{\mathrm{s}}c_{\mathrm{s}}(\mathrm{I})} + \underbrace{\gamma_{\infty}^{\mathrm{sl}}}_{a_{\mathrm{s}}c_{\mathrm{s}}(\mathrm{II})} \right) \frac{1}{\beta} + \left(\underbrace{\gamma_{\infty}^{\mathrm{sl}}}_{b_{\mathrm{s}}c_{\mathrm{s}}(\mathrm{I})} + \underbrace{\gamma_{\infty}^{\mathrm{sl}}}_{b_{\mathrm{s}}c_{\mathrm{s}}(\mathrm{II})} \right) \frac{1}{\xi} \right] \right\} \tag{2.2.2.7}$$

where $\underbrace{\gamma_{\infty}^{\mathrm{lv}}}_{a_{\mathrm{s}}b_{\mathrm{s}}(\mathrm{I})}$, $\underbrace{\gamma_{\infty}^{\mathrm{lv}}}_{a_{\mathrm{s}}b_{\mathrm{s}}(\mathrm{II})}$, $\underbrace{\gamma_{\infty}^{\mathrm{lv}}}_{a_{\mathrm{s}}c_{\mathrm{s}}(\mathrm{I})}$, $\underbrace{\gamma_{\infty}^{\mathrm{lv}}}_{a_{\mathrm{s}}c_{\mathrm{s}}(\mathrm{II})}$, $\underbrace{\gamma_{\infty}^{\mathrm{lv}}}_{b_{\mathrm{s}}c_{\mathrm{s}}(\mathrm{I})}$, $\underbrace{\gamma_{\infty}^{\mathrm{lv}}}_{b_{\mathrm{s}}c_{\mathrm{s}}(\mathrm{II})}$, $\underbrace{\gamma_{\infty}^{\mathrm{sl}}}_{a_{\mathrm{s}}b_{\mathrm{s}}(\mathrm{I})}$, $\underbrace{\gamma_{\infty}^{\mathrm{sl}}}_{a_{\mathrm{s}}b_{\mathrm{s}}(\mathrm{II})}$, $\underbrace{\gamma_{\infty}^{\mathrm{sl}}}_{a_{\mathrm{s}}c_{\mathrm{s}}(\mathrm{I})}$, $\underbrace{\gamma_{\infty}^{\mathrm{sl}}}_{a_{\mathrm{s}}c_{\mathrm{s}}(\mathrm{II})}$, $\underbrace{\gamma_{\infty}^{\mathrm{sl}}}_{b_{\mathrm{s}}c_{\mathrm{s}}(\mathrm{I})}$, and $\underbrace{\gamma_{\infty}^{\mathrm{sl}}}_{b_{\mathrm{s}}c_{\mathrm{s}}(\mathrm{II})}$ are, respectively, the surface energy of each liquid/vapor and solid/liquid flat interface. It is easy to verify that if all liquid and solid facets are characterized by the same surface energy ($\gamma_{\infty}^{\mathrm{lv}}$ and $\gamma_{\infty}^{\mathrm{sl}}$, respectively), eq 2.2.2.6 is returned. Moreover, while it is more probable that solid facets are characterized by different surface energies, this is an unlikely occurrence for "liquid facets". Indeed, as already mentioned (Heng et al., 2006), different values of $\gamma_{\infty}^{\mathrm{sl}}$ may be owed to an anisotropic spatial distribution of atoms/molecules inside a crystalline network. On the contrary, this explanation appears to be far less plausible inside a liquid phase owing to the lack of a crystalline order. Accordingly, although eq 2.2.2.7 is more general, the differentiation of $\gamma_{\infty}^{\mathrm{lv}}$ is commonly unnecessary.

Similarly, eq 2.2.2.6 solution requires the evaluation of ΔH_{m} on T_{m} (see the integral in eq 2.2.2.6) and Zhang's approach may be used (Zhang et al., 2000). With the same hypotheses of eq 2.2.1.9, Zhang's equation for parallelepipeds reads:

$$\begin{aligned} \Delta H_{\mathrm{m}} &= \left[-\gamma_{\infty}^{\mathrm{sv}} \frac{A^{\mathrm{sv}}}{\rho_{\mathrm{s}} V^{\mathrm{s}}} \right]_{(1)} + \left[\int_{T_{\mathrm{m}}}^{T_{\mathrm{m}\infty}} C_P^{\mathrm{s}} \mathrm{d}T \right]_{(2)} + \left[\Delta H_{\mathrm{m}\infty} \right]_{(3)} + \left[\gamma_{\infty}^{\mathrm{lv}} \frac{A^{\mathrm{lv}}}{\rho_{\mathrm{l}} V^{\mathrm{l}}} \right]_{(4)} + \left[\int_{T_{\mathrm{m}\infty}}^{T_{\mathrm{m}}} C_P^{\mathrm{l}} \mathrm{d}T \right]_{(5)} = \\ &= \Delta H_{\mathrm{m}\infty} - \frac{2}{a_{\mathrm{s}}} \left(\frac{\gamma_{\infty}^{\mathrm{sv}}}{\rho_{\mathrm{s}}} - \frac{\gamma_{\infty}^{\mathrm{lv}}}{\rho_{\mathrm{l}}} \right) \left(1 + \frac{1}{\beta} + \frac{1}{\xi} \right) - \left(C_P^{\mathrm{l}} - C_P^{\mathrm{s}} \right) \left(T_{\mathrm{m}\infty} - T_{\mathrm{m}} \right) \end{aligned} \tag{2.2.2.8}$$

where V^{s} and A^{sv} are, respectively, the solid phase volume and the area of the solid-vapor interface referring to the ensemble of parallelepipeds with dimensions a_{s}, b_{s}, c_{s}, V^{l} and A^{lv} are, respectively, the liquid phase volume and the area of the liquid-vapor interface referring to the ensemble of parallelepipeds with dimensions a_{s}, b_{s}, c_{s}.

The melting properties dependence on nanoparallelepipeds size a_s ($T_m(a_s)$; $\Delta H_m(a_s)$) is achieved by the simultaneous numerical solution of eqs 2.2.2.6 and 2.2.2.8. By assuming that ΔH_m is constant in the temperature interval ($T_{m\infty}$; $T_{m1} = T_{m\infty} - \Delta T$), eq 2.2.2.6 reads:

$$\int_{T_{m\infty}}^{T_{m1}} \Delta H_m \frac{dT_m}{T_m} \approx \Delta H_{m1} \ln\left(T_{m1}/T_{m\infty}\right) \approx -\frac{4}{3a_{s1}}\left[\gamma_\infty^{lv}\left(\frac{1}{\rho_s}-\frac{1}{\rho_l}\right)\left(\frac{1}{1+2\Delta}+\frac{1}{\beta+2\Delta}+\frac{1}{\xi+2\Delta}\right)+\frac{\gamma_\infty^{sl}}{\rho_s}\left(1+\frac{1}{\beta}+\frac{1}{\xi}\right)\right] \quad (2.2.2.9)$$

Consequently, the first estimation of ΔH_{m1} according to eq 2.2.2.9 is:

$$\Delta H_{m1} = -\frac{4}{3a_{s1}\ln\left(T_{m1}/T_{m\infty}\right)}\left[\gamma_\infty^{lv}\left(\frac{1}{\rho_s}-\frac{1}{\rho_l}\right)\left(\frac{1}{1+2\Delta}+\frac{1}{\beta+2\Delta}+\frac{1}{\xi+2\Delta}\right)+\frac{\gamma_\infty^{sl}}{\rho_s}\left(1+\frac{1}{\beta}+\frac{1}{\xi}\right)\right] \quad (2.2.2.10)$$

By equating this ΔH_{m1} estimation to the Zhang's one (eq 2.2.2.8), it is possible to determine the value of a_{s1} related to T_{m1}:

$$a_{s1} = \frac{2\left(\frac{\gamma_\infty^{sv}}{\rho_s}-\frac{\gamma_\infty^{lv}}{\rho_l}\right)\left(1+\frac{1}{\beta}+\frac{1}{\xi}\right)-\frac{4}{3\ln\left(T_{m1}/T_{m\infty}\right)}\left[\begin{array}{l}\gamma_\infty^{lv}\left(\frac{1}{\rho_s}-\frac{1}{\rho_l}\right)\left(\frac{1}{1+2\Delta}+\frac{1}{\beta+2\Delta}+\frac{1}{\xi+2\Delta}\right)+\\ +\frac{\gamma_\infty^{sl}}{\rho_s}\left(1+\frac{1}{\beta}+\frac{1}{\xi}\right)\end{array}\right]}{\Delta H_{m\infty}-\left(C_P^l-C_P^s\right)\left(T_{m\infty}-T_{m1}\right)} \quad (2.2.2.11)$$

Once a_{s1} is known, ΔH_{m1} may be evaluated according to eq 2.2.2.6 or eq 2.2.2.8. By repeating the same strategy for further reductions of T_m, the following general expression for a_{si} is achieved:

$$a_{si} = \frac{2\left(\frac{\gamma_\infty^{sv}}{\rho_s}-\frac{\gamma_\infty^{lv}}{\rho_l}\right)\left(1+\frac{1}{\beta}+\frac{1}{\xi}\right)-\frac{4}{3\ln\left(T_{mi}/T_{mi-1}\right)}\left[\begin{array}{l}\gamma_\infty^{lv}\left(\frac{1}{\rho_s}-\frac{1}{\rho_l}\right)\left(\frac{1}{1+2\Delta}+\frac{1}{\beta+2\Delta}+\frac{1}{\xi+2\Delta}\right)+\\ +\frac{\gamma_\infty^{sl}}{\rho_s}\left(1+\frac{1}{\beta}+\frac{1}{\xi}\right)\end{array}\right]}{\Delta H_{m\infty}-\left(C_P^l-C_P^s\right)\left(T_{m\infty}-T_{mi}\right)+\frac{1}{\ln\left(T_{mi}/T_{mi-1}\right)}\sum_{j=1}^{i-1}\Delta H_{mj}\ln\left(T_{mj}/T_{mj-1}\right)} \quad (2.2.2.12)$$

Similarly, after finding a_{si}, ΔH_{mi} may be evaluated according to eq 2.2.2.6 or eq 2.2.2.8. In order to ensure the reliability of the numerical procedure, ΔT was set equal to 0.1 K.

2.2.3. Cylinders

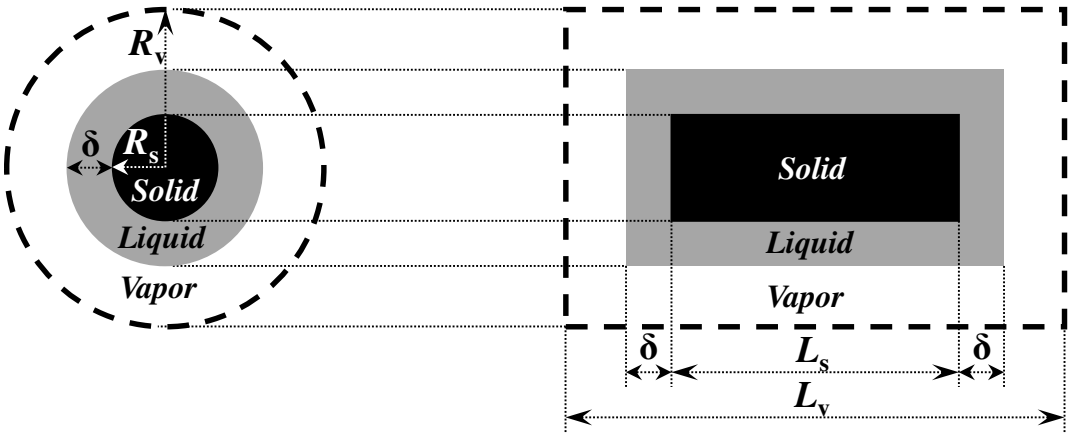

Figure 2.4. Spatial disposition of the three drug phases (solid, liquid and vapor) according to the LNG and LSM theories. R_s and L_s represent the radius and the length of the cylinder solid core, respectively, δ is the thickness of the surrounding liquid layer, while R_v and L_v are the radius and the length of the vapor phase, respectively.

By following the same strategy adopted for parallelepipeds, the two derivatives dA^{lv}/dV^{v} and dA^{sl}/dV^{s} become, for cylindrical crystals (see Figure 2.4):

$$\frac{dA^{lv}}{dV^{v}} = \frac{d[2\pi(R_s+\delta)^2 + 2\pi(R_s+\delta)(L_s+2\delta)]}{d[\pi R_v^2 L_v - \pi(R_s+\delta)^2(L_s+2\delta)]} = -\frac{4}{3R_s}\left(\frac{1}{1+\Delta}+\frac{1}{\lambda+2\Delta}\right) \tag{2.2.3.1}$$

$$\frac{dA^{sl}}{dV^{s}} = \frac{d\left(2\pi R_s^2 + 2\pi R_s L_s\right)}{d\left(\pi R_s^2 L_s\right)} = \frac{4}{3R_s}\left(1+\frac{1}{\lambda}\right) \tag{2.2.3.2}$$

where R_s, L_s, R_v, and L_v represent the radius and the length of the solid and vapor phases, respectively, δ is the thickness of the surrounding liquid layer, $\Delta = \delta/R_s$, and $\lambda = L_s/R_s$. While performing the two derivatives, the volume $\pi R_v^2 L_v$ is assumed constant.

For cylindrical crystals, particular attention should be paid to the expression of the interface energy as, while assuming the lateral surface of the cylinder chemically and physically equal to the two bases, the different curvature of the bases (infinite curvature) and the lateral surface (curvature = $1/R_s$) should be considered. Hence, according to eqs 2.2.3.1, 2.2.3.2, and 2.2.1.3, eq 2.27b becomes:

$$\Delta H_m \frac{dT_m}{T_m} = -\left(\frac{1}{\rho_s}-\frac{1}{\rho_l}\right) d\left\{\gamma_\infty^{lv}\frac{4}{3}\left[\frac{1}{R_s(1+\Delta)+2\delta_0}+\frac{1}{R_s(\lambda+2\Delta)}\right]\right\} - \frac{1}{\rho_s} d\left[\gamma_\infty^{sl}\frac{4}{3}\left(\frac{1}{R_s+2\delta_0}+\frac{1}{\lambda R_s}\right)\right] \tag{2.2.3.3}$$

Similarly, Δ may be evaluated by resorting to X_{nc} (drug nanocrystals mass/drug total mass):

$$X_{nc} = \frac{\rho_s \pi R_s^2 L_s}{\rho_s \pi R_s^2 L_s + \rho_l \left[\pi (R_s + \delta)^2 (L_s + 2\delta) - \pi R_s^2 L_s\right]} \tag{2.2.3.4}$$

or:

$$\Delta^3 + \left(2 + \frac{\lambda}{2}\right)\Delta^2 + (\lambda + 1)\Delta + \frac{\lambda \rho_s}{2\rho_l}\left(1 - \frac{1}{X_{nc}}\right) = 0 \tag{2.2.3.5}$$

The numerical solution (Newton's method) of eq 2.2.3.5 allows determining the parameter Δ required by eq 2.2.3.3. By assuming both ρ_s and ρ_l independent of R_s, the integration of eq 2.2.3.3 from the melting temperature of the infinitely large crystal ($T_{m\infty}$) to the one of the nanocrystal with radius R_s (T_m) allows finding the working equation holding for cylinders:

$$\int_{T_{m\infty}}^{T_m} \Delta H_m \frac{dT_m}{T_m} = -\frac{4}{3}\left\{\gamma_\infty^{lv}\left(\frac{1}{\rho_s} - \frac{1}{\rho_l}\right)\left[\frac{1}{R_s(1+\Delta) + 2\delta_0} + \frac{1}{R_s(\lambda + 2\Delta)}\right] + \frac{\gamma_\infty^{sl}}{\rho_s}\left(\frac{1}{R_s + 2\delta_0} + \frac{1}{\lambda R_s}\right)\right\} \tag{2.2.3.6}$$

Similarly, eq 2.2.3.6 solution requires the evaluation of ΔH_m on T_m (see the integral in eq 2.2.3.6) and Zhang's approach may be used (Zhang et al., 2000). With the same hypotheses of eq 2.2.1.9, Zhang's equation for cylinders reads:

$$\begin{aligned} \Delta H_m &= \left[-\gamma^{sv}\frac{A^{sv}}{\rho_s V^s}\right]_{(1)} + \left[\int_{T_m}^{T_{m\infty}} C_P^s dT\right]_{(2)} + \left[\Delta H_{m\infty}\right]_{(3)} + \left[\gamma^{lv}\frac{A^{lv}}{\rho_l V^l}\right]_{(4)} + \left[\int_{T_{m\infty}}^{T_m} C_P^l dT\right]_{(5)} = \\ &= \Delta H_{m\infty} - 2\left(\frac{\gamma_\infty^{sv}}{\rho_s} - \frac{\gamma_\infty^{lv}}{\rho_l}\right)\left(\frac{1}{\lambda R_s} + \frac{1}{R_s + 2\delta_0}\right) - \left(C_P^l - C_P^s\right)\left(T_{m\infty} - T_m\right) \end{aligned} \tag{2.2.3.7}$$

where V^s and A^{sv} are the solid phase volume and the area of the solid-vapor interface referring to the ensemble of cylinders with radius R_s and length L_s, respectively, while V^l and A^{lv} are the liquid phase volume and the area of the liquid-vapor interface referring to the ensemble of cylinders with radius R_s and length L_s, respectively. Equations 2.2.3.6 and 2.2.3.7 inspection reveals that the reduction of surface energy (γ^{lv}, γ^{sl}) with cylinder radius (see eq 2.2.1.3) implies a smaller decrease of both ΔH_m and T_m.

The melting properties dependence on nanocylinders radius R_s ($T_m(R_s)$; $\Delta H_m(R_s)$) is achieved by the simultaneous numerical solution of eqs 2.2.3.6 and 2.2.3.7. By assuming that ΔH_m is constant in the temperature interval ($T_{m\infty}$; $T_{m1} = T_{m\infty} - \Delta T$), eq 2.2.3.6 reads:

$$\int_{T_{m\infty}}^{T_{m1}} \Delta H_m \frac{dT_m}{T_m} \approx \Delta H_{m1} \ln\left(T_{m1}/T_{m\infty}\right) \approx -\frac{4}{3\ln\left(T_{m1}/T_{m\infty}\right)} \left\{ \begin{array}{l} \gamma_\infty^{lv}\left(\frac{1}{\rho_s}-\frac{1}{\rho_l}\right)\left[\frac{1}{(1+\Delta)R_{s1}+2\delta_0}+\frac{1}{(\lambda+2\Delta)R_{s1}}\right]+ \\ +\frac{\gamma_\infty^{sl}}{\rho_s}\left(\frac{1}{R_{s1}+2\delta_0}+\frac{1}{\lambda R_{s1}}\right) \end{array} \right\} \tag{2.2.3.8}$$

Consequently, the first estimation of ΔH_{m1} according to eq 2.2.3.8 is:

$$\Delta H_{m1} = -\frac{4}{3\ln\left(T_{m1}/T_{m\infty}\right)} \left\{ \gamma_\infty^{lv}\left(\frac{1}{\rho_s}-\frac{1}{\rho_l}\right)\left[\frac{1}{(1+\Delta)R_{s1}+2\delta_0}+\frac{1}{(\lambda+2\Delta)R_{s1}}\right]+\frac{\gamma_\infty^{sl}}{\rho_s}\left(\frac{1}{R_{s1}+2\delta_0}+\frac{1}{\lambda R_{s1}}\right) \right\} \tag{2.2.3.9}$$

By equating this ΔH_{m1} estimation to the Zhang's one (eq 2.2.3.7), it is possible to determine the value of R_{s1} related to T_{m1}:

$$\begin{aligned} &-\frac{4}{3\ln\left(T_{m1}/T_{m\infty}\right)} \left\{ \gamma_\infty^{lv}\left(\frac{1}{\rho_s}-\frac{1}{\rho_l}\right)\left[\frac{1}{(1+\Delta)R_{s1}+2\delta_0}+\frac{1}{(\lambda+2\Delta)R_{s1}}\right]+\frac{\gamma_\infty^{sl}}{\rho_s}\left(\frac{1}{R_{s1}+2\delta_0}+\frac{1}{\lambda R_{s1}}\right) \right\} = \\ &= \Delta H_{m\infty} - 2\left(\frac{\gamma_\infty^{sv}}{\rho_s}-\frac{\gamma_\infty^{lv}}{\rho_l}\right)\left(\frac{1}{\lambda R_{s1}}+\frac{1}{R_{s1}+2\delta_0}\right)-\left(C_P^l-C_P^s\right)\left(T_{m\infty}-T_{m1}\right) \end{aligned} \tag{2.2.3.10}$$

R_{s1} is determined according to Newton's method by assuming a relative tolerance of 10^{-6}. Once R_{s1} is known, ΔH_{m1} may be evaluated according to eq 2.2.3.6 or eq 2.2.3.7. By repeating the same strategy for further reductions of T_m, the following general equation for R_{si} is achieved:

$$\begin{aligned} &-\frac{1}{\ln\left(T_{mi}/T_{mi-1}\right)} \left\{ \begin{array}{l} \frac{4}{3}\gamma_\infty^{lv}\left(\frac{1}{\rho_s}-\frac{1}{\rho_l}\right)\left[\frac{1}{(1+\Delta)R_{si}+2\delta_0}+\frac{1}{(\lambda+2\Delta)R_{si}}\right]+ \\ +\frac{4\gamma_\infty^{sl}}{3\rho_s}\left(\frac{1}{R_{si}+2\delta_0}+\frac{1}{\lambda R_{si}}\right)+\sum_{j=1}^{i-1}\Delta H_{mj}\ln\left(T_{mj}/T_{mj\text{-}1}\right) \end{array} \right\} = \\ &= \Delta H_{m\infty} - 2\left(\frac{\gamma_\infty^{sv}}{\rho_s}-\frac{\gamma_\infty^{lv}}{\rho_l}\right)\left(\frac{1}{\lambda R_{si}}+\frac{1}{R_{si}+2\delta_0}\right)-\left(C_P^l-C_P^s\right)\left(T_{m\infty}-T_{mi}\right) \end{aligned} \tag{2.2.3.11}$$

Similarly, after finding R_{si}, ΔH_{mi} may be evaluated according to eq 2.2.3.6 or eq 2.2.3.7. In order to ensure the reliability of the numerical procedure, ΔT was set equal to 0.1 K.

2.3. Solubility and Crystal Size

It is interesting to evaluate the effect of the variation of melting temperature/enthalpy on a nanocrystals property of paramount importance, i.e. the nanocrystals solubility in a solvent (typically water when considering drug nanocrystals). The solubility dependence on nanocrystals size may be obtained by a classic thermodynamic approach describing the equilibrium between a liquid phase (solvent) and a nanocrystalline solid phase (drug) (Prausnitz et al., 1999). By assuming that only drug dissolves in the solvent (not vice versa), the equilibrium conditions require that the drug fugacity in the solid phase ($\hat{f}_{\mathrm{d}}^{\mathrm{s}}$) equals the drug fugacity in the liquid phase ($\hat{f}_{\mathrm{d}}^{\mathrm{l}}$):

$$\hat{f}_{\mathrm{d}}^{\mathrm{l}} = \gamma_{\mathrm{d}} X_{\mathrm{d}} f_{\mathrm{d}}^{\mathrm{l}} = f_{\mathrm{d}}^{\mathrm{s}} = \hat{f}_{\mathrm{d}}^{\mathrm{s}} \tag{2.3.1}$$

where γ_{d} and X_{d} are, respectively, the drug activity coefficient and the solubility (molar fraction) in the solvent, $f_{\mathrm{d}}^{\mathrm{l}}$ is the drug fugacity in the reference state, while $f_{\mathrm{d}}^{\mathrm{s}}$ is the drug fugacity in the solid state. Accordingly, the drug solubility in the liquid phase reads:

$$X_{\mathrm{d}} = \frac{f_{\mathrm{d}}^{\mathrm{s}}}{f_{\mathrm{d}}^{\mathrm{l}}} \frac{1}{\gamma_{\mathrm{d}}} \tag{2.3.2}$$

By assuming $f_{\mathrm{d}}^{\mathrm{l}}$ as the fugacity of the pure drug in the state of undercooled liquid at the system temperature (T) and pressure (P), the ratio $f_{\mathrm{d}}^{\mathrm{s}} / f_{\mathrm{d}}^{\mathrm{l}}$ is obtainable by:

$$\Delta\overline{G}_{41} = RT \ln\left(f_{\mathrm{d}}^{\mathrm{l}} / f_{\mathrm{d}}^{\mathrm{s}}\right) \tag{2.3.3}$$

where R is the universal gas constant and $\Delta\overline{G}_{41}$ represents the variation of the molar Gibbs' free energy between the state of undercooled liquid drug (state 4) and that of solid (nanocrystalline) drug (state 1). $\Delta\overline{G}_{41}$ may be conveniently evaluated according to the thermodynamic cycle depicted in Figure 2.5: solid nanocrystals at T and P represent state 1; state 2 portrays nanocrystals heated, at constant pressure (P), up to their melting temperature T_{m}; state 3 depicts the completely melted nanocrystals at T_{m} and P; and, finally, state 4 is achieved by cooling up to T, at constant pressure P, the liquid drug (undercooled liquid). Accordingly, it follows:

$$\Delta\overline{G}_{41} = \Delta\overline{H}_{41} - T\Delta\overline{S}_{41} = \Delta\overline{H}_{21} + \Delta\overline{H}_{32} + \Delta\overline{H}_{43} - T\left(\Delta\overline{S}_{21} + \Delta\overline{S}_{32} + \Delta\overline{S}_{43}\right) \tag{2.3.4}$$

where $\Delta\overline{H}_{\mathrm{ij}}$ and $\Delta\overline{S}_{\mathrm{ij}}$ are, respectively, the variation of molar enthalpy and entropy between state

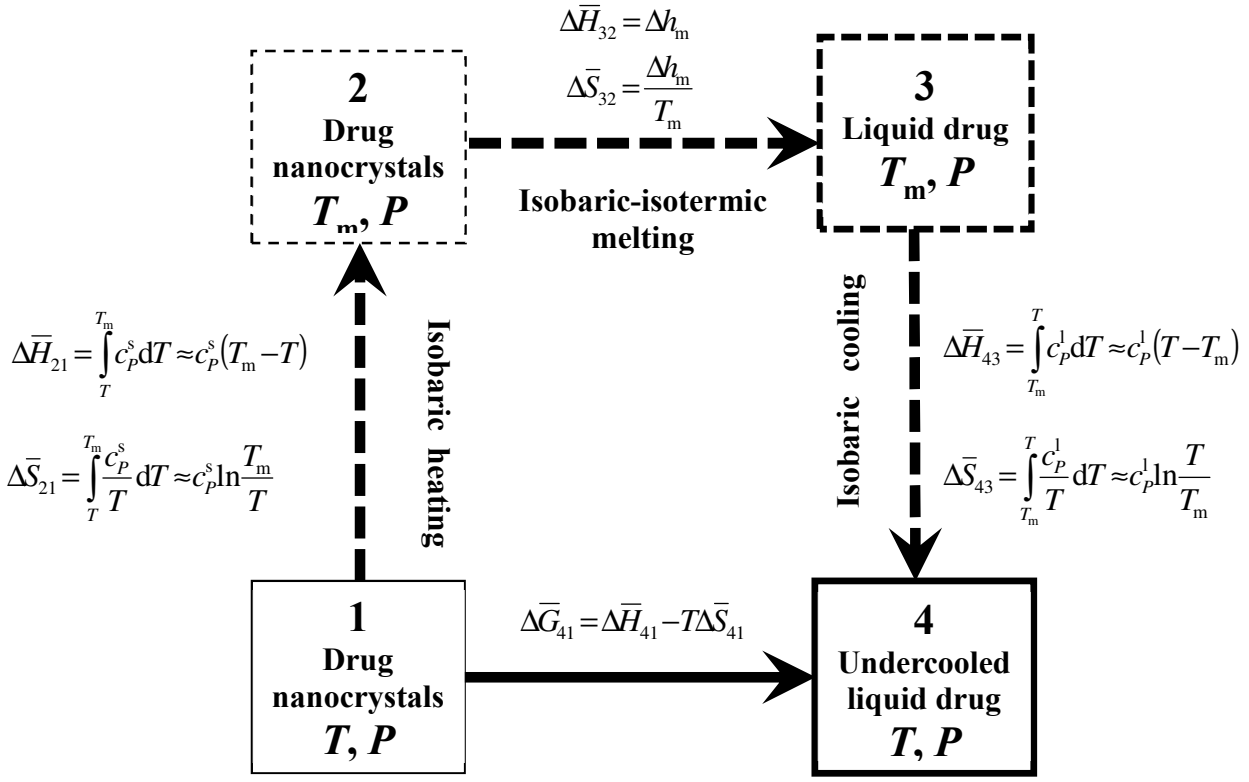

Figure 2.5. Thermodynamic cycle estimating the molar Gibbs' free energy ($\Delta\overline{G}_{41}$) variation between the state of undercooled liquid drug (state 4) and that of solid (nanocrystalline) drug (state 1). T is absolute temperature, P is pressure, T_{m} is nanocrystals melting temperature, while $\Delta\overline{H}_{\mathrm{ij}}$ and $\Delta\overline{S}_{\mathrm{ij}}$ are, respectively, the specific enthalpy and entropy variation between state j and i.

j and i. In details:

$$\Delta\overline{H}_{21}=\int_{T}^{T_{\mathrm{m}}}c_P^{\mathrm{s}}\mathrm{d}T\approx c_P^{\mathrm{s}}\left(T_{\mathrm{m}}-T\right) \tag{2.3.5}$$

$$\Delta\overline{S}_{21}=\int_{T}^{T_{\mathrm{m}}}\frac{c_P^{\mathrm{s}}}{T}\mathrm{d}T\approx c_P^{\mathrm{s}}\ln\frac{T_{\mathrm{m}}}{T}\qquad[\text{as } \mathrm{d}P=0] \tag{2.3.6}$$

$$\Delta\overline{H}_{32}=\Delta h_{\mathrm{m}} \tag{2.3.7}$$

$$\Delta\overline{S}_{32}=\frac{\Delta h_{\mathrm{m}}}{T_{\mathrm{m}}}\qquad[\text{as } \Delta g_{\mathrm{m}}=\Delta h_{\mathrm{m}}-T\Delta s_{\mathrm{m}}=0\,] \tag{2.3.8}$$

$$\Delta\overline{H}_{43}=\int_{T_{\mathrm{m}}}^{T}c_P^{\mathrm{l}}\mathrm{d}T\approx c_P^{\mathrm{l}}\left(T-T_{\mathrm{m}}\right) \tag{2.3.9}$$

$$\Delta\bar{S}_{43} = \int_{T_m}^{T} \frac{c_P^l}{T} dT \approx c_P^l \ln \frac{T}{T_m} \qquad [\text{as } dP = 0] \tag{2.3.10}$$

where c_P^s and c_P^l are, respectively, the solid and liquid drug molar specific heat at constant pressure, while Δg_m and Δs_m are, respectively, the molar nanocrystals melting Gibbs' free energy and entropy. By rearranging eqs 2.3.3 – 2.3.10, drug solubility may be expressed as a function of determinable parameters:

$$X_d = \frac{1}{\gamma_d} \left(\frac{T}{T_m} \right)^{\frac{\Delta c_P}{R}} \exp\left\{ -\left[\frac{\Delta h_m}{RT} \left(1 - \frac{T}{T_m} \right) + \frac{\Delta c_P}{R} \left(1 - \frac{T_m}{T} \right) \right] \right\} \tag{2.3.11}$$

where $\Delta c_P = c_P^l - c_P^s$ and Δh_m is the molar melting enthalpy. Finally, it is convenient to remind the relation between molar solubility X_d and mass/volume solubility (C_s):

$$C_s = \frac{X_d}{1 - X_d} \frac{M_d}{M_s} \rho_{sol} \tag{2.3.12}$$

where M_d and M_s are, respectively, the drug and solvent molecular weight, while ρ_{sol} is the solvent density.

For a better understanding of the physical meaning of eq 2.3.11, Figure 2.6 and Figure 2.7 exhibit X_d trend in rather artificial but useful situations. In particular, ideal conditions (γ_d = 1) with two different constant values of T (25 and 37°C) and Δh_m (23479 and 33541 J/mol), which are typical for small organic drugs, were assumed. Furthermore, Δc_P was set equal to 103 J/mol°C, another typical value for small organic drugs. It appears clear that, no matter the values of T or Δh_m, an increase of T_m is reflected in a reduction of X_d, which is reasonable as the higher T_m the more stable the crystal is. Accordingly, its dissolution in an external solvent is less favored, which implies the reduction of X_d. Moreover, eq 2.3.11 indicates that X_d increases with T (Figure 2.6) and decreases with Δh_m (Figure 2.7). While the first occurrence concerns the majority of solid-solvent couples, the second one is connected to the thermodynamic stability of the crystalline network. Indeed, a higher Δh_m implies a more stable crystalline network whose destruction due to the external solvent is less favored. Although real cases are considerably more complicated as the activity coefficient γ_d may depend on X_d and since T_m decrease implies Δh_m simultaneous reduction (amply discussed in section 2.2), Figures 2.6 and 2.7 allow capturing the physical essence of eq 2.3.11.

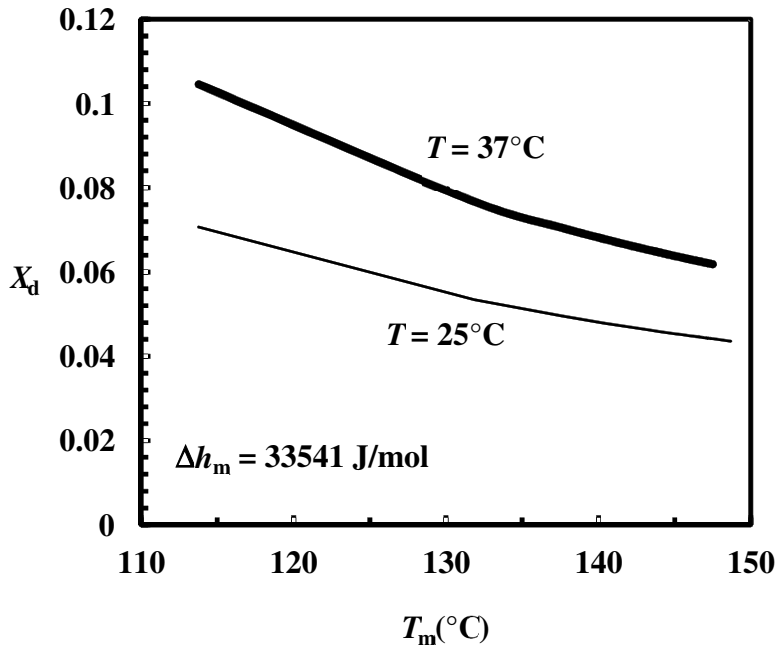

Figure 2.6. Ideal (γ_d = 1) molar solubility (X_d) dependence (eq 2.3.11) on melting temperature (T_m) at constant molar melting enthalpy (Δh_m) for two different operating temperatures (T) and Δc_P = 103 J/mol°C.

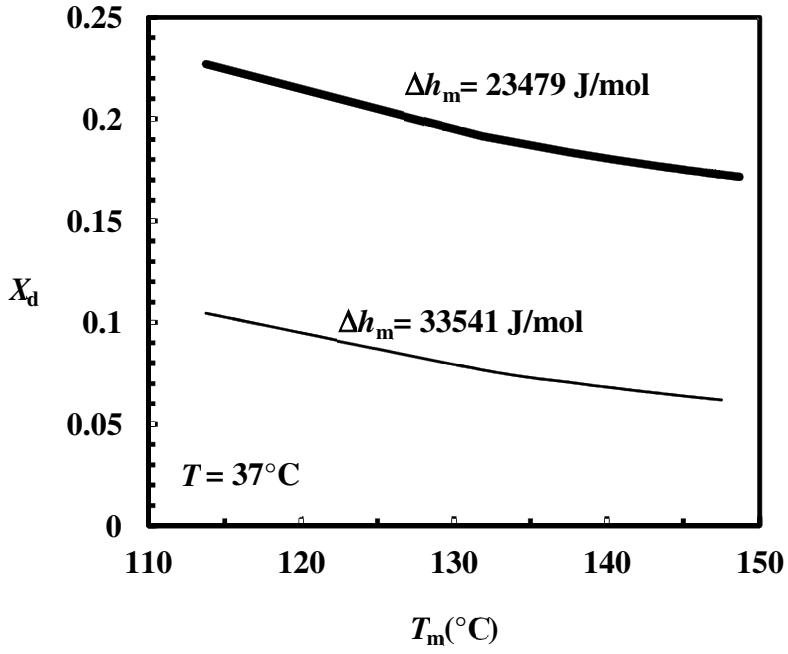

Figure 2.7. Ideal (γ_d = 1) molar solubility (X_d) dependence (eq 2.3.11) on melting temperature (T_m) at constant operating temperature (T) for two different values of molar melting enthalpy (Δh_m) and Δc_P = 103 J/mol°C.

2.4. Conclusions

In this chapter, a thermodynamic mathematical model able to evaluate the simultaneous reduction of melting temperature/enthalpy with crystal size was described. One of the main advantages of this approach resides in the absence of fitting parameters as all those present may be experimentally measured or theoretically determined. In addition, this model is able to take account of the shape of crystals, by overcoming the traditional and unrealistic simplification of spherical crystals. Finally, its combination with the classic thermodynamic approach describing the solid/liquid equilibrium was exposed. Therefore, a clear connection between typical bulk thermal properties (T_m and Δh_m) and solutions properties (X_d) was established.

CHAPTER 3

MODEL VALIDATION

3.1. Materials

Nimesulide (NIM) is a non-steroidal anti-inflammatory (NSAID) with pain medication and fever-reducing properties. Its approved indications are the treatment of acute pain, the symptomatic treatment of osteoarthritis, and primary dysmenorrhoea in adolescents and adults above 12 years old. It has a multifactorial mode of action and is characterized by a fast onset of action. It works by blocking the production of prostaglandins (a chemical associated with pain), thereby relieving pain and inflammation. NIM is absorbed rapidly following oral administration (Bernareggi, 1998) and undergoes extensive biotransformation, mainly to 4-hydroxynimesulide (which also appears to be biologically active). Food, gender, and advanced age have negligible effects on NIM pharmacokinetics. NIM has a relatively rapid onset of action, with meaningful reductions in pain and inflammation observed within 15 minutes from drug intake (Rainsford, 2006; Bianchi and Broggini, 2003). The therapeutic effects of NIM are the result of its complex mode of action, which targets a number of key mediators of the inflammatory process such as COX-2 mediated prostaglandins, free radicals, proteolytic enzymes, and histamine (Rainsford, 2006). Clinical evidence is available to support a particularly good profile in terms of gastrointestinal tolerability. (Laporte et al., 2004).

Nifedipine (NIF) is a drug used to manage angina, high blood pressure, Raynaud's phenomenon, and premature labor. It is one of the treatments of choice for Prinzmetal angina. It may be used to treat severe high blood pressure during pregnancy. Its use in preterm labor may allow more time for steroids to improve baby's lungs and time to transfer the mother to a well-qualified medical facility before delivery. NIF is taken by mouth and comes in fast and slow release formulations. NIF is a calcium channel blocker. Although NIF and other dihydropyridines are commonly regarded as specific to the L-type calcium channel, they also possess non-specific activity towards

other voltage-dependent calcium channels (Curtis et al., 2001; McDonald et al., 1994). NIF has additionally been found to act as an antagonist of the mineralocorticoid receptor, or as an antimineralocorticoid (Luther, 2014).

Griseofulvin (GRI) is an antifungal drug used to treat a number of types of dermatophytoses (ringworm). This includes fungal infections of the nails and skin when antifungal creams are ineffective. It is taken by mouth. GRI works by interfering with fungal mitosis. GRI is used orally only for dermatophytosis. It is ineffective topically. It is reserved for cases with nail, hair, or large body surface involvement (Tripathi, 2008). The drug binds to tubulin, interfering with microtubule function, thus inhibiting mitosis. It binds to keratin in keratin precursor cells and makes them resistant to fungal infections. The drug reaches its site of action only when hair or skin is replaced by the keratin-GRI complex. GRI then enters the dermatophyte through energy-dependent transport processes and binds to fungal microtubules. This alters the processing for mitosis and also the underlying information for the deposition of fungal cell walls.

3.1.1. Properties Evaluation

The melting temperature/enthalpy ($T_m/\Delta H_m$) and the difference of specific heat capacity at constant pressure between the liquid and solid drug may be measured by a differential scanning calorimeter (DSC). After calibrating DSC with indium, the actual measurement on drug or drug-carrier mixture consists in placing about 2 mg of sample in a pierced aluminum pan subsequently heated at a scanning rate of 10°C per minute under an inert atmosphere of nitrogen. The solid drug density may be determined by a helium pycnometer, while the liquid one as the ratio between drug molecular weight and its liquid molar volume (M_v) obtained by the group contribution method (Fedors, 1974; Van Krevelen and Hoftyzer, 1976) implemented in Breitkreutz's software (Breitkreutz, 1974).

The determination of the drug solid-vapor surface tension (γ_∞^{sv}) may be performed according to the following equation of state (Kwok and Neumann, 1999):

$$\cos\theta_i = 2\sqrt{\frac{\gamma_\infty^{sv}}{\gamma_i^{lv}}}e^{-\beta\left(\gamma_i^{lv}-\gamma_\infty^{sv}\right)^2} - 1 \qquad (3.1.1.1)$$

where θ_i is the contact angle of the liquid "i" on the solid drug, β is a model fitting parameter, and γ_i^{lv} is the liquid i-vapor surface tension. Equation 3.1.1.1 fitting to the experimental $\cos\theta_i$ of different liquids yields γ_∞^{sv} and β. Contact angles may be measured by a tensiometer. The drug

liquid-vapor surface tension (γ_{∞}^{lv}) may be evaluated by the parachor method (Van Krevelen, 1990):

$$\gamma_{\infty}^{lv} = \left(\frac{P_s}{M_v} \right)^4 \tag{3.1.1.2}$$

while the solid-liquid one (γ_{∞}^{sl}) according to Young's equation for pure substances ($\theta = 0$) (Adamson and Gast, 1997):

$$\gamma_{\infty}^{sl} = \gamma_{\infty}^{sv} - \gamma_{\infty}^{lv} \tag{3.1.1.3}$$

The drug solid-water surface tension (γ_1^{sl}) may be determined by Young's equation (Adamson and Gast, 1997):

$$\gamma_1^{sl} = \gamma_{\infty}^{sv} - \gamma_1^{lv} \cos\theta_1 \tag{3.1.1.4}$$

The drug Tolman's length (δ), i.e. 1/3 of the drug molecule diameter (Rowlinson and Windom, 1982), may be evaluated by knowing M_v and assuming spherical drug molecules:

$$\delta = \frac{1}{3}\sqrt[3]{\frac{6M_v}{N_A \pi}} \tag{3.1.1.5}$$

where N_A is Avogadro's number (Tolman, 1949).

3.2. Molecular Dynamics

3.2.1. Set-up

Due to the intrinsic difficulties in obtaining $T_m/\Delta H_m$ of specific size and shape nanocrystals from experimental tests, the present work resorts to molecular dynamics (MD) simulations in order to evaluate the aforementioned properties. The atomistic MD simulations explicitly represent the atoms constituting a nanocrystal, with the result that $T_m/\Delta H_m$ evaluations may become computationally unfeasible, especially for large crystals. In the present study, reference model volumes were selected as the best compromise among the computational time required to accurately derive $T_m/\Delta H_m$ and the values necessary for the comparison with the thermodynamic model. The minimum simulated volume in each data set ensures the construction of a reliable nanocrystal molecular model, featuring at least three crystallographic units in each direction whatever the nanocrystal shape and shape factor are.

NIM single crystal structure was retrieved from the Cambridge Structural Database (Cambridge, UK) (CCDC 773602) (Groom et al., 2016). NIM orthorhombic $Pca2_1$ crystal cell parameters are the following: *a* 16.1268 Å, *b* 5.0411 Å, *c* 32.761 Å, α 90°, β 90°, γ 90°.

The crystal cell was optimized by using Dreiding's force field with charges derived by fitting the electrostatic potential surface of the optimized structure at B3LYP/6-31G (d,p) level by Turbomole 7.1 (http://www.turbomole-gmbh.com) and RESP method (Bayly et al., 1993; Sanphui et al., 2011). NIM single crystal nanoparticles (NPs) of appropriate dimensions and shape were built by employing the *Nanocluster* module present in the Materials Studio v. 6.1 (Accelrys Inc., USA) program (http://accelrys.com/products/collaborative-science/biovia-materials-studio/). Free boundary conditions (free surfaces in a vacuum) were applied to MD simulations, which were performed within the canonical ensemble (NVT) where a constant temperature *T* was maintained by using Berendsen's method in a constant volume *V* (Berendsen et al., 1984). The van der Waals and electrostatic interactions were modeled by using Lennard-Jones' potential and a group contribution method, respectively, truncated at 1.20 nm. A 1 fs time step was used throughout simulations. NIM NPs were first relaxed at 300 K for 1 ns before gradually heating them at intervals. Then, NPs were equilibrated for at least 15 ns at each temperature assuming the last phase space point of a calculation as an input for the next temperature calculation. MD simulations were run by the Materials Studio v. 6.1 software in an in-house cluster.

Nanocrystals T_m was evaluated by calculating the potential energy per NIM molecule during heating (at each temperature, potential energy was averaged over the last 5 ns of each simulation with at least 500 independent configurations) and determining the melting point as the temperature where potential energy changes abruptly at the first-order transition point. In addition, ΔH_m could be calculated from the associated increment of potential energy.

The computational procedure described above was also applied to two further drugs, namely NIF and GRI. The unit cell of NIF (CCDC BICCIZ) has the following properties: monoclinic P1, a 10.923 Å, b 10.326 Å, c 14.814 Å, α 90°, β 92.7°, γ 90°. GRI (CCDC GRISFL02) has a tetragonal cell and a P41 space group with lattice parameters: a 8.967 Å, b 8.967 Å, c 19.904 Å, α 90°, β 90°, γ 90°. The COMPASS force field (Kumar and Shastri, 2014; Zhu et al., 2012) was applied to these MD simulations with charges calculated at B3LYP/6-31G(d) level.

3.2.2. Comparison

With the aim of validating the trends predicted by the presented thermodynamic model, MD calculations were performed in order to derive $T_m/\Delta H_m$ behavior of parallelepiped-shaped

nanocrystals as a function of selected shape factors (ξ = 0.1, 1, 10) for the considered three small organic drugs, NIM, NIF, and GRI.

Figures 3.2.2.1 and 3.2.2.2 display the comparison between NIM $T_m/\Delta H_m$ reductions with the crystal volume (V_C) decrease predicted by the thermodynamic model (eqs 2.2.2.6 and 2.2.2.8; solid lines) and those obtained by MD approach (open symbols). MD calculations confirm the decrease of T_m and ΔH_m as a function of nanocrystal volume predicted by the thermodynamic model. Moreover, the influence of shape factor (ξ) at constant crystal volume is properly resolved.

A further verification of the model was performed by considering the two-remaining small organic drugs, NIF and GRI, both belonging to Amidon's class II (low water solubility and good permeability). Figures 3.2.2.3 and 3.2.2.4 display the comparison between NIF $T_m/\Delta H_m$ reductions predicted by the thermodynamic model (eqs 2.2.2.6 and 2.2.2.8; solid lines) and those obtained by MD approach (open symbols). Similarly, Figures 3.2.2.5 and 3.2.2.6 display the comparison between GRI $T_m/\Delta H_m$ reductions predicted by the thermodynamic model (eqs 2.2.2.6 and 2.2.2.8; solid lines) and those obtained by MD approach (open symbols). Hence, a reasonable agreement between the presented model predictions and MD simulations is clearly exhibited also for the considered two-other organic drugs, namely NIF and GRI.

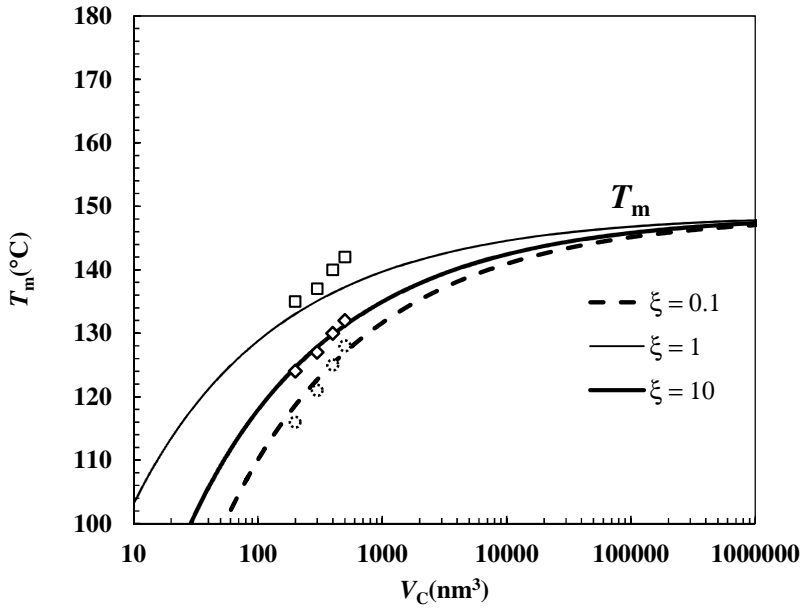

Figure 3.2.2.1. Nimesulide. Comparison between the melting temperature (T_m) reduction with the crystal volume (V_C) decrease according to the thermodynamic model (eqs 2.2.2.6 and 2.2.2.8; solid lines) and the molecular dynamics approach (symbols). The simulations were performed assuming nimesulide nanocrystals as parallelepipeds characterized by a square base (β = 1), three different shape factors (ξ = 0.1, 1, 10), and a nanocrystals mass fraction X_{nc} = 1.

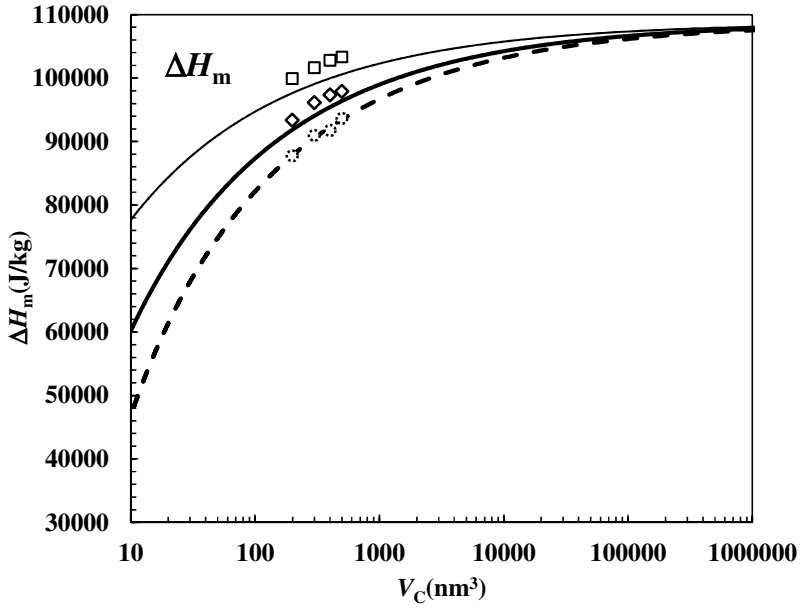

Figure 3.2.2.2. Nimesulide. Comparison between the melting enthalpy (ΔH_m) reduction with the crystal volume (V_C) decrease according to the thermodynamic model (eqs 2.2.2.6 and 2.2.2.8; solid lines) and the molecular dynamics approach (symbols). The simulations were performed assuming nimesulide nanocrystals as parallelepipeds characterized by a square base ($\beta = 1$), three different shape factors ($\xi = 0.1, 1, 10$), and a nanocrystals mass fraction $X_{nc} = 1$.

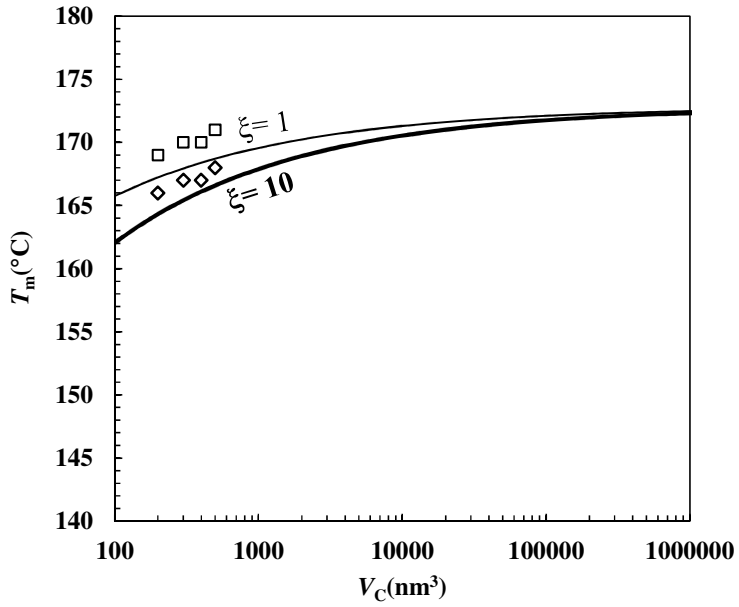

Figure 3.2.2.3. Nifedipine. Comparison between the melting temperature (T_m) reduction with the crystal volume (V_C) decrease according to the thermodynamic model (eqs 2.2.2.6 and 2.2.2.8; solid lines) and the molecular dynamics approach (symbols). The simulations were performed assuming nifedipine nanocrystals as parallelepipeds characterized by a square base ($\beta = 1$), two different shape factors ($\xi = 1, 10$), and a nanocrystals mass fraction $X_{nc} = 1$.

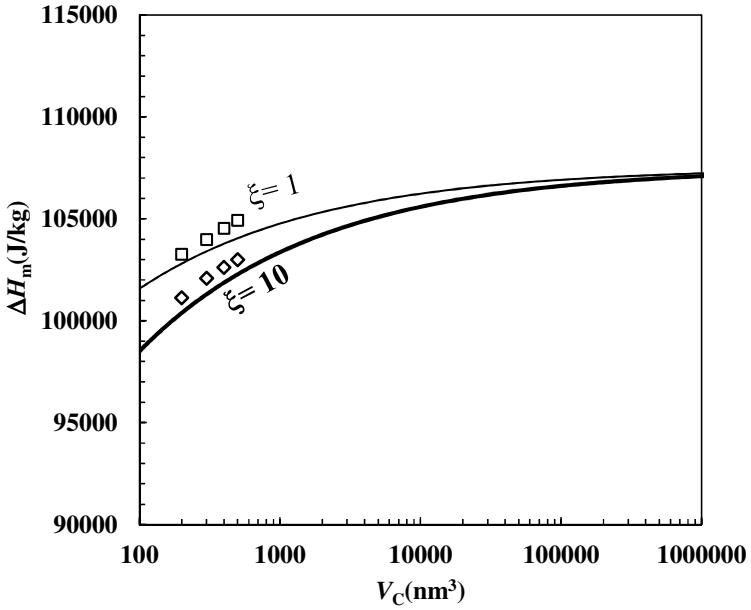

Figure 3.2.2.4. Nifedipine. Comparison between the melting enthalpy (ΔH_m) reduction with the crystal volume (V_C) decrease according to the thermodynamic model (eqs 2.2.2.6 and 2.2.2.8; solid lines) and the molecular dynamics approach (symbols). The simulations were performed assuming nifedipine nanocrystals as parallelepipeds characterized by a square base (β = 1), two different shape factors (ξ = 1, 10), and a nanocrystals mass fraction X_{nc} = 1.

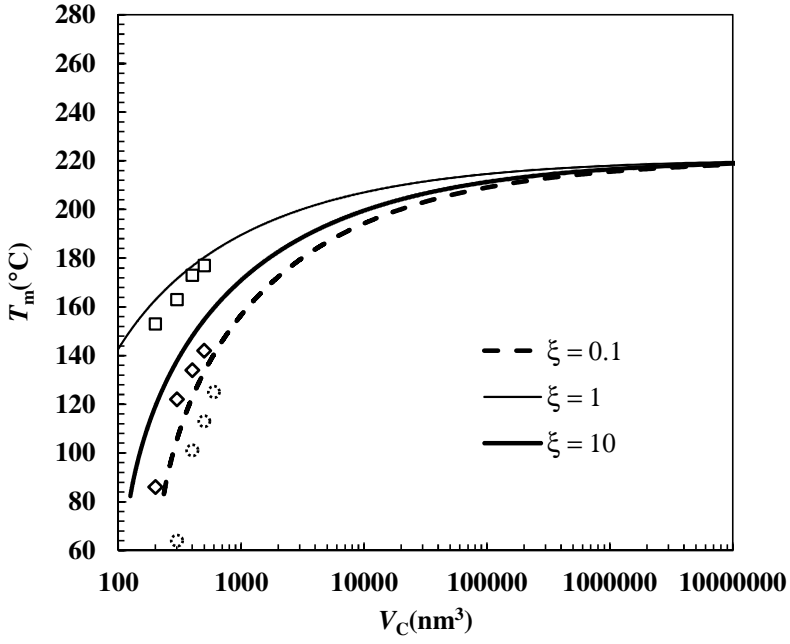

Figure 3.2.2.5. Griseofulvin. Comparison between the melting temperature (T_m) reduction with the crystal volume (V_C) decrease according to the thermodynamic model (eqs 2.2.2.6 and 2.2.2.8; solid lines) and the molecular dynamics approach (symbols). The simulations were performed assuming griseofulvin nanocrystals as parallelepipeds characterized by a square base (β = 1), three different shape factors (ξ = 0.1, 1, 10), and a nanocrystals mass fraction X_{nc} = 1.

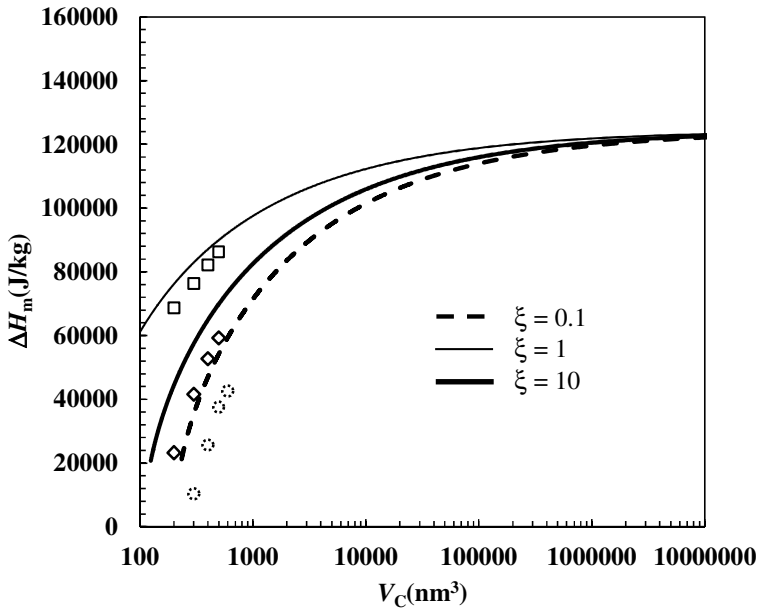

Figure 3.2.2.6. Griseofulvin. Comparison between the melting enthalpy (ΔH_m) reduction with the crystal volume (V_C) decrease according to the thermodynamic model (eqs 2.2.2.6 and 2.2.2.8; solid lines) and the molecular dynamics approach (symbols). The simulations were performed assuming griseofulvin nanocrystals as parallelepipeds characterized by a square base ($\beta = 1$), three different shape factors ($\xi = 0.1$, 1, 10), and a nanocrystals mass fraction $X_{nc} = 1$.

3.3. Theoretical Considerations

Being very difficult to establish the smallest volume of a crystalline solid constituted by small organic molecules, obviously, the developed thermodynamic model relies on the hypothesis that the crystalline phase has always the same properties regardless of crystal size (aside from the surface tension in spherical crystals). Nevertheless, some considerations may be made by resorting to the classical nucleation theory according to which the critical nucleation radius (r_c) of a spherical crystal corresponds to the maximum difference between Gibbs' energy of the solid and liquid phases (ΔG):

$$\Delta G = -\Delta G_V \tfrac{4}{3}\pi r_c^3 + \gamma_\infty^{sl} 4\pi r_c^2 \tag{3.3.1}$$

$$\Delta G_V \approx \frac{\Delta H_{m\infty}\rho_s}{T_{m\infty}}\left(T_{m\infty} - T_c\right) \tag{3.3.2}$$

$$r_c = \frac{2\gamma_\infty^{sl}}{\Delta G_V} \tag{3.3.3}$$

where ρ_s represents solid density, $\Delta H_{m\infty}$ and $T_{m\infty}$ are the melting enthalpy and temperature of the infinitely large crystal, while T_c is the undercooling temperature ($T_c < T_{m\infty}$). In the case of parallelepiped-shaped crystals, eq 3.3.3 becomes:

$$r_c = \frac{2}{3}\left(1+\frac{1}{\beta}+\frac{1}{\xi}\right)\frac{\gamma_\infty^{sl}}{\Delta G_V} \tag{3.3.4}$$

where β and ξ are, respectively, the length/width and height/width ratios characterizing the crystal. At this point, it is interesting to compare T_c and T_m as a function of crystal volume (V_C) according to the theory developed by Brun and co-workers for spherical nanocrystals (Brun et al., 1973), the starting point of the thermodynamic model proposed in this work:

$$r_C = \frac{2T_{m\infty}}{(T_{m\infty}-T_m)\Delta H_{m\infty}}\left[\left(\frac{1}{\rho_s}-\frac{1}{\rho_l}\right)\gamma_\infty^{lv}+\frac{\gamma_\infty^{sl}}{\rho_s}\right] \tag{3.3.5}$$

where r_C represents nanocrystal radius and ρ_l is liquid density. It is noticeable that, as ρ_s and ρ_l are quite similar in value, eq 3.3.5 may be simplified into:

$$r_C \approx \frac{2T_{m\infty}}{(T_{m\infty}-T_m)\Delta H_{m\infty}}\left(\frac{\gamma_\infty^{sl}}{\rho_s}\right) \tag{3.3.6}$$

which is nothing but the well-known Gibbs-Thomson's equation.

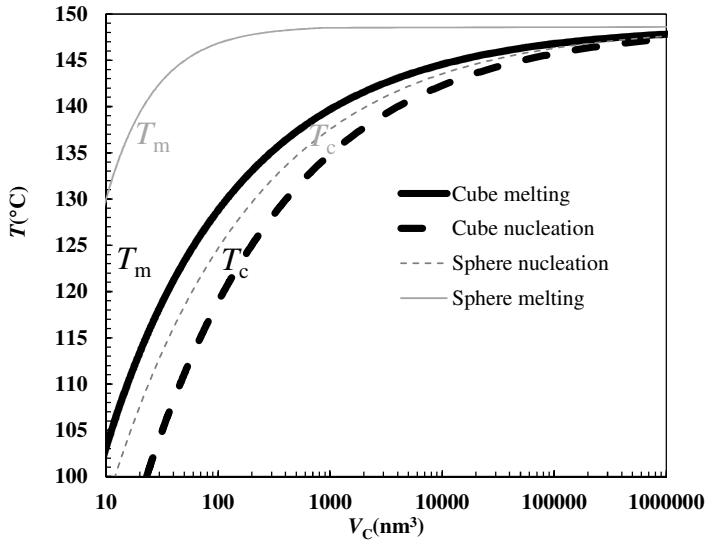

Figure 3.3.1. Comparison between nimesulide undercooling (T_c; eqs 3.3.3 and 3.3.4) and melting (T_m; eqs 3.3.5 and 2.2.2.6) temperatures as a function of crystal volume (V_C) for spherical (gray and thin lines) and cubic (black and thick lines) crystals.

Figure 3.3.1 demonstrates that, in the case of spherical nanocrystals (gray and thin lines), the two

approaches yield very different values of V_C when $T_c = T_m$. Indeed, T_m (continuous gray line; eq 3.3.5) and T_c (dashed gray line; eq 3.3.3) curves are completely detached from each other. This result indicates that Brun's theory (eq 3.3.5) relying on Gibbs-Duhem's equations and the nucleation approach (eqs 3.3.3 and 3.3.4) produce different outcomes. In particular, it appears that Brun's theory predicts the existence of smaller nanocrystals than those predicted by the nucleation approach. Interestingly, in the case of a cube (similar results are also obtainable for different shaped parallelepipeds), T_m trend according to the approach of the present work (eq 2.2.2.6; black and thick line) is considerably closer to that predicted by the nucleation theory (eq 3.3.4; black and dashed thick line). In the light of the approximations adopted to derive eqs 3.3.3 and 3.3.4 (with particular reference to the evaluation of ΔG_V), it seems that the outcomes of the developed model are compatible with those of the nucleation theory.

In the case of cylindrical crystals, similar considerations could also be made, although the situation is complicated by the fact that the lateral surface energy of a cylinder reduces with cylinder radius as predicted by Tolman's equation (eq 2.2.1.3). Accordingly, an ad hoc mathematical approach should be necessary.

The experimental verification (from the thermal and solubility point of view) of the presented model is very complicated. Indeed, not only the experimental determination of nanocrystals solubility is affected by several issues, as previously stated in Section 1.5, but also the simultaneous experimental determination of nanocrystals melting temperature/enthalpy and size is very complex. In the case of metals, although some uncertainties still exist (Goswani and Nanda, 2012), the thermodynamic models validation is achievable by means of a variety of techniques such as DSC for melting temperature/enthalpy and Transmission Electron Microscopy (TEM) for crystals size. Conversely, in the case of drug nanocrystals, almost all the authors exploring the melting point depression of organic drugs considered drug crystals embedded in regular inorganic or organic nanoporous matrices (Hamilton et al., 2012). Consequently, the melting temperature/enthalpy depression could be evaluated, for instance, by means of DSC, while nanocrystals size could be related to pores size. However, this is insufficient for the complete solution of the problem, as nicely documented in Sonnemberger et al., 2016. The authors realized that an amorphous drug layer develops between pore wall and nanocrystal surface due to drug-wall interactions. Accordingly, the determination of crystals size may be performed only indirectly. Indeed, it is the same situation arising when water freezes inside inorganic materials such as silica (Ishikiriyama et al., 1995). Since, in this last case, the determination of the amorphous layer thickness is feasible by following Ishikiriyama's procedure, it was decided, in the present study, to adapt the developed model in order to evaluate the silica pores size distribution

by relying on DSC measurements. The comparison between the pores size distribution according to the model and BET (Brunauer, Emmett, and Teller) measurements is displayed in Figure 3.3.2. The agreement between the two approaches is substantially acceptable and seems to prove the reliability of the developed model.

Despite this encouraging result, an analogous validation for the ensemble of polydispersed nanocrystals in a polymeric matrix constituted by crosslinked microparticles (Colombo et al., 2009) proves complicated. While melting temperature may be easily determined by DSC, crystals size may be only deduced by resorting, for instance, to a mathematical interpretation of X-ray diffraction patterns (Bergese et al., 2004). Accordingly, more than an experimental validation of the model, this could resemble a comparison between two different models. Ultimately, all the previous considerations suggested MD simulations as the most reliable (and feasible) approach to validating the presented thermodynamic model.

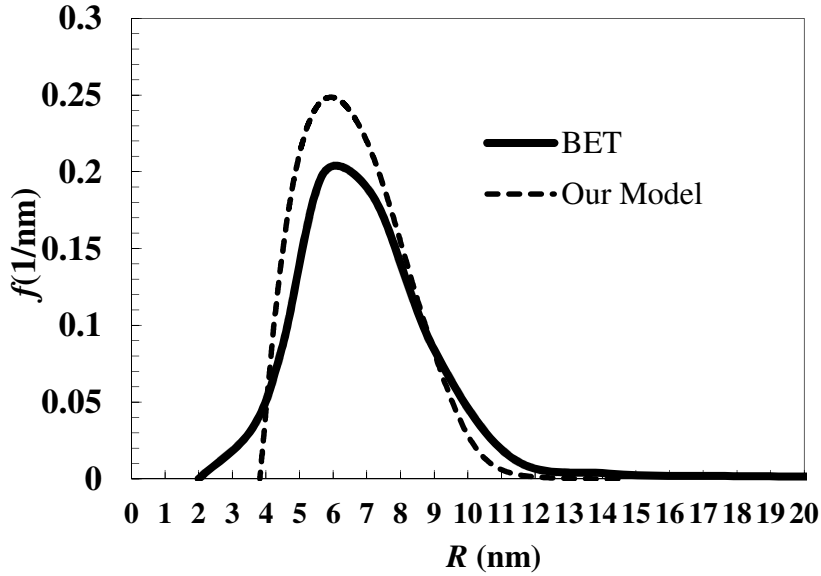

Figure 3.3.2. Comparison between the silica pores size distribution according to the presented model (dashed line) and BET measurements (solid line).

3.4. Solubility Evaluation

While atomistic MD simulations represent a very useful tool for validating the proposed thermodynamic model from the prediction of melting temperature/enthalpy point of view, a rather more complex problem is the model validation when it predicts the solubility increase with the decrease of nanocrystals dimension. Indeed, as mentioned in Chapter 1, the experimental work on nanocrystals is rendered problematic by several issues such as a) the manufacturing processes

which usually alter nanocrystals characteristics by introducing lattice defects, b) the presence of little impurities able to affect solubility, and c) the well-known Ostwald ripening (Madras et al., 2003) which affects the polydispersed nanocrystals ensemble. In particular, the last phenomenon results in the growth of larger and hence less soluble crystals at the expense of the smaller and thus more soluble ones. This, in turn, is reflected in the asymptotic decrease of experimental solubility. Unfortunately, a further problem afflicts the experimental verification of this model from the solubility point of view again. As discussed in Chapter 2 (see eq 2.3.11), not only the knowledge of the drug activity coefficient (γ_d) in the liquid phase is essential but also its dependence on solubility (or crystal dimension) is necessary for a reliable comparison between experimental solubility and model predictions. In the light of all these difficulties, it was decided, in this study, to abandon the idea of validating experimentally the model from the solubility point of view in favor of the evaluation of γ_d by resorting to experimentally known solubility data. For this purpose, the interpretation of experimental data obtained from intrinsic dissolution rate (IDR) tests proved to be very useful. This test aims to evaluate the solid dissolution rate in a solvent (water) at a fixed temperature and under carefully controlled hydrodynamic conditions.

3.4.1. Intrinsic Dissolution Rate

IDR is the typical test employed in the pharmaceutical field to evaluate solid drugs dissolution and performed by different experimental set-ups. One of the most famous consists in a drug disk fixed on a rotating shaft (ω is angular velocity) and immersed in a dissolving medium (typically water or an aqueous solvent) of very large volume. In order to greatly simplify the theoretical analysis, the drug cylinder lateral surface is coated by an impermeable membrane against the dissolving medium so that dissolution occurs only at the disk bottom plane surface. According to Levich (Levich, 1962), the first to model the test, the solid and liquid phases perfectly adhere (no fluid slippage). Therefore, at the liquid-solid interface, the dissolving fluid moves exclusively in a rotational manner. Immediately after the interface, the axial (v_y), tangential (v_θ), and radial (v_r) fluid velocity components are all different from zero, the reason for which the fluid approaches the solid surface according to a spiral trajectory. Away from the disk rotating surface, v_θ and v_r reduce progressively. Owing to the fluid continuity and the perfect adhesion to the solid surface, the rotating disk attracts the fluid from the bottom and moves it radially, thus causing the fluid streamlines to describe a loop. By solving the momentum and continuity equations, Levich concluded that the only important velocity component is v_y when the distance from the rotating surface is longer than a threshold value, the hydrodynamic boundary layer (δ_0). In addition, he

demonstrated that solids dissolution is ruled by the diffusive transport across the so-called diffusive boundary layer ($\delta < \delta_0$) whose thickness depends on the fluid kinematic viscosity, angular velocity, and the solid diffusion coefficient in the solvent.

Levich's theoretical analysis allows schematizing the dissolution process, which may be considered a consecutive steps process driven by energy changes (Grassi et al., 2007). The first step consists in the contact of the solvent with the solid surface (wetting), which leads to the creation of a solid-liquid interface by starting from a solid-vapor one. The cleavage of the molecular bonds of the solid (melting) and the molecules movement toward the solid-liquid interface (solvation) are the second and third steps, respectively. The final step is the transfer of the solvated molecules from the interfacial region to the bulk solution (diffusion). Obviously, each stage of the process requires energy to occur and the total energy for dissolution is the sum of the contributions related to the four aforementioned steps. Generally, the most important contribution to solids dissolution in terms of energy is represented by the melting step. While solvation and diffusion depend on the solid-solvent couple chemical nature and the dissolution environment conditions (temperature and mechanical agitation, for example), wetting and melting are also affected by the solid microstructure.

According to Levich, while the concentration of solid molecules at the solid surface is assumed equal to the solid solubility (C_s) in the dissolving medium, the drug concentration in the bulk solution (C_b) is presumed homogeneous and lower than C_s due to the mass transfer resistance offered by the boundary layer. By applying Fick's second law of diffusion to the boundary layer and assuming a linear solid concentration within it, the temporal increase in C_b is obtained by:

$$\frac{dC_b}{dt} = \frac{S}{V}\frac{D_{d0}}{\delta}(C_s - C_b) = \frac{S}{V}k_d(C_s - C_b) \qquad (3.4.1.1)$$

where t is time, V is the dissolving medium volume, S is the solid surface area available for dissolution, and k_d is the intrinsic dissolution constant, i.e. the ratio between the solid diffusion coefficient (D_{d0}) in the solvent and δ. By assuming that C_b is initially zero, eq 3.4.1.1 solution leads to:

$$C_b = C_s\left(1 - e^{-k_d\frac{S}{V}t}\right) \qquad (3.4.1.2)$$

A possible way to consider the effect of poor wettability on solids dissolution consists in considering the presence of a mass transfer resistance ($1/k_m$) at the solid-liquid interface in such a way that Fick's second equation must be solved by applying the following boundary conditions:

solid/liquid interface

$$D_{d0}\left.\frac{\partial C}{\partial X}\right|_{X=0} = -k_m\left(C_s - C_{|X=0}\right) \qquad (3.4.1.3)$$

boundary layer/dissolving medium bulk

$$\left.\frac{\partial C}{\partial X}\right|_{X=\delta} = -\frac{V}{S\,D_{d0}}\frac{dC_b}{dt} = -\frac{V}{S\,\delta\,k_d}\frac{dC_b}{dt} \qquad C_b = C_{|X=\delta} \qquad (3.4.1.4)$$

Equation 3.4.1.3 states that the solid concentration at the solid-liquid interface is variable because it increases from zero (the initial condition in the boundary layer) to C_s, with k_m ruling this kinetic process. Accordingly, high k_m values translate into a rapid interfacial drug concentration increase and a good solid wettability, while low k_m values are responsible for a slow interfacial drug concentration rise and a poor solid wettability. Therefore, infinitely high k_m values imply the absence of wettability problems of the solid surface for the solvent. In the light of eqs 3.4.1.3 – 3.4.1.4, Fick's second law (for a linear concentration profile in the boundary layer) leads to:

$$C_b = C_s\left(1 - e^{-\frac{S}{V}\frac{k_d t}{1+k_d/k_m}}\right) \qquad (3.4.1.5)$$

Thus far, solids properties such as C_s have been implicitly assumed constant during dissolution. However, it is well-known that many organic compounds may exist in different crystalline structures such as polymorphs and solvates, as it often happens to organic drugs (Nogami et al., 1969). Moreover, temperature, pressure, and surrounding conditions (i.e. the existence of a liquid phase in contact with the solid phase) determine which crystalline structure is the most stable. Accordingly, during dissolution (at constant temperature and pressure), the contact with a new fluid phase (solvent) may induce a solid phase transformation from a polymorphic phase (the most stable configuration in the absence of dissolving medium) to another (the most stable configuration in the presence of dissolving medium). Hence, the polymorphic transformation may take place in some solvents but not in others. As, for thermodynamic reasons, a solid exhibiting polymorphism should possess different activities depending on its structure (Higuchi et al., 1967), the polymorphic transformations generally imply a variation of C_s, thus highly influencing the entire dissolution process. A particularly interesting phase transformation is that of an amorphous compound which becomes a solid when encounters an aqueous dissolving medium. In this case, a considerable variation (decrease) of drug solubility may also occur (Nogami et al., 1969). By assuming that the release rate at the amorphous compound/dissolving medium interface is much faster than the mass transport process across the diffusion layer, superficial phase transformations

occur until the entire dissolving surface becomes a crystalline solid. This indicates that solubility ranges from an initial value (C_{si}), that of the amorphous state, to a final one (C_{sf}), that of the crystalline solid. By supposing that the rate of crystal growth is 1) proportional to the degree of supersaturation and 2) ruled by a first order kinetics with respect to concentration, the solubility variation may be described by the following equation (Nogami et al., 1969):

$$\frac{dC_s}{dt} = k_r\left(C_{sf} - C_s\right) \tag{3.4.1.6}$$

where C_s is the time-dependent solid solubility and k_r is the recrystallization constant. Equation 3.4.1.6 solution leads to:

$$C_s = C_{sf} + \left(C_{si} - C_{sf}\right)e^{-k_r t} \tag{3.4.1.7}$$

Furthermore, by assuming that the phase transformation leaves the dissolving surface unvaried and D_{d0} in the diffusion layer is the same for the two forms (amorphous and crystalline), the entire dissolution process may be described by introducing eq 3.4.1.7 into eq 3.4.1.1:

$$\frac{dC_b}{dt} = \frac{S}{V}k_d\left[C_{sf} + \left(C_{si} - C_{sf}\right)e^{-k_r t} - C_b\right] \tag{3.4.1.8}$$

whose solution is:

$$C_b = C_{sf}\left(1 - e^{-\frac{k_d S}{V}t}\right) + \frac{C_{si} - C_{sf}}{1 - \frac{k_r V}{k_d S}}\left(e^{-k_r t} - e^{-\frac{k_d S}{V}t}\right) \tag{3.4.1.9}$$

In the case of sink conditions ($C_{bmax} < 0.2C_{sf}$, i.e. $C_s(t) - C_b \approx C_s(t)$ in eq 3.4.1.8), eq 3.4.1.9 is simplified in:

$$C_b = \frac{k_d S}{V}\left[C_{sf}t + \frac{C_{si} - C_{sf}}{k_r}\left(1 - e^{-k_r t}\right)\right] \tag{3.4.1.10}$$

By starting from eq 3.4.1.10, it is possible to find a simple way to evaluate k_d and C_{si}:

$$\left.\frac{dC_b}{dt}\right|_{t\to\infty} = \frac{k_d S}{V}C_{sf} \tag{3.4.1.11}$$

$$\left.\frac{dC_b}{dt}\right|_{t=0} = \frac{k_d S}{V}C_{si} \tag{3.4.1.12}$$

As $\left.\frac{dC_b}{dt}\right|_{t\to\infty}$ and $\left.\frac{dC_b}{dt}\right|_{t=0}$ may be numerically evaluated from experimental data and C_{sf} is experimentally known, eqs 3.4.1.11 and 3.4.1.12 allow the evaluation of k_d and C_{si}. Then, eq 3.4.1.10 fitting to experimental data allows the determination of the last fitting parameter, i.e. k_r. In this way, it is possible to overcome the issue connected with the correlation of an elevated number of parameters in both eqs 3.4.1.9 and 3.4.1.10.

While all the above considerations regard the dissolution of a pure solid phase, it may be very important to consider the dissolution of a uniform, intimate, and non-disintegrating mixture of two solid compounds, *A* and *B*. A particularly interesting case is that of *A* and *B* representing, respectively, the crystalline and amorphous phases of the same compound. In this situation, the global dissolution rate depends on 1) the crystalline and amorphous solubility and 2) the compound diffusion coefficient in the boundary layer facing the mixture surface. As dissolution proceeds, however, the amorphous phase content of the solid-liquid interface reduces due to its higher solubility, while the crystalline fraction of the interface increases up to the total disappearance of the amorphous phase. In other words, as the speed of the receding front for the amorphous phase is higher than that relative to the crystalline phase during dissolution, the position of the amorphous phase front (L_a) is farther from the initial interface than that of the crystalline phase (L_c). Obviously, the higher the difference ($L_a - L_c$), the lower the amorphous phase dissolution rate, as the molecules detaching from the amorphous phase travel an increasing distance represented by the sum of ($L_a - L_c$) and δ. Hence, the following set of equations holds (Grassi et al., 2007):

$$V\frac{dC_b}{dt} = S_c k_{dc}\left(C_{sc} - C_b\right) + \frac{S_a\left(C_a - C_b\right)}{\frac{1}{k_{da}} + \frac{\tau}{D_{d0}\,\varepsilon}\left(L_a - L_c\right)} \tag{3.4.1.13}$$

$$\frac{dM_c}{dt} = -S\,A_c\frac{dL_c}{dt} = -S_c k_{dc}\left(C_{sc} - C_b\right) \tag{3.4.1.14}$$

$$VC_b = S\,L_c A_c + S\,L_a A_a \Rightarrow L_a = \frac{VC_b}{S\,A_a} - \frac{L_c A_c}{A_a} \tag{3.4.1.15}$$

where S_a and S_c are, respectively, the dissolving surfaces of the amorphous and crystalline phases ($S = S_a + S_c$), k_{dc} and k_{da} are, respectively, the crystalline and amorphous phases dissolution constants (theoretically equal), while C_{sc} and C_{sa} are, respectively, the crystalline and amorphous drug solubility. Furthermore, C_{sa} time dependency is represented by eq 3.4.1.7. While M_c indicates the mass of the crystalline phase, A_a and A_c represent, respectively, the amount of the amorphous

and crystalline phases per unit volume and are defined by:

$$A_a = \frac{\rho_a \rho_c (1 - X_c)}{\rho_c (1 - X_c) + \rho_a X_c} \tag{3.4.1.16}$$

$$A_c = \frac{\rho_a \rho_c X_c}{\rho_c (1 - X_c) + \rho_a X_c} \tag{3.4.1.17}$$

where ρ_a and ρ_c are, respectively, the amorphous and crystalline phases density, while X_c is the crystalline mass fraction in the mixture. S_a and S_c are evaluated by assuming that the amorphous and crystalline phases consist of small cubes of side ΔX. Thus, the number of the amorphous (N_a) and crystalline (N_c) cubes is represented by $V_a/\Delta X^3$ and $V_c/\Delta X^3$, respectively, where V_a and V_c indicate, respectively, the volume occupied by the amorphous and crystalline phases in the assumed non-porous mixture. By assuming that the dissolving surface, for each phase, is the sum of the six cubes faces (the same final result may be also obtained by considering only the face perpendicular to the dissolution direction), it follows that $S_a = 6\Delta X^2 N_a$ and $S_c = 6\Delta X^2 N_c$. The substitution of the expressions of N_a and N_c leads to $S_a = 6V_a/\Delta X$ and $S_c = 6V_c/\Delta X$. As $V_a/V_c = (\rho_c/\rho_a)(1 - X_c)/X_c$, then $S_a/S_c = (\rho_c/\rho_a)(1 - X_c)/X_c$. Hence, it may be concluded that:

$$S_a = S\frac{1 - X_c}{1 + X_c\left(\frac{\rho_a}{\rho_c} - 1\right)} \qquad S_c = S\frac{X_c}{\frac{\rho_c}{\rho_a} - X_c\left(\frac{\rho_c}{\rho_a} - 1\right)} \tag{3.4.1.18}$$

It is easy to verify that when $\rho_a = \rho_c$, $S_a = SA_a/(A_a + A_c)$ and $S_c = SA_c/(A_a + A_c)$.

Fundamentally, eq 3.4.1.13 states that the variation of the compound concentration in the dissolving medium is due to the sum of two distinct contributions: the one of the crystalline phase (eq 3.4.1.13 first right-hand side term) and that of the amorphous phase (eq 3.4.1.13 second right-hand side term). In particular, while the mass transport resistance for the crystalline phase is represented by $1/k_{dc}$, this phase being always in direct contact with the dissolving medium, the mass transport resistance relative to the amorphous phase is represented by $\tau(L_a - L_c)/(D_{d0}\,\varepsilon)$. Indeed, before reaching the boundary layer (the mass transport resistance equals $1/k_{da}$), the compound molecules detaching from the amorphous phase travel the additional length ($L_a - L_c$). In order to consider the path tortuosity (τ) and porosity (ε), this length is multiplied by τ/ε. During the amorphous phase dissolution, the mixture becomes porous and its porosity is:

$$\varepsilon = \frac{A_a}{\rho_a} \tag{3.4.1.19}$$

While eq 3.4.1.14 expresses the reduction of the crystalline mass and, consequently, allows evaluating L_c increase with time, eq 3.4.1.15 is a mass balance stating that the compound amount dissolved up to time t equals the one present in the dissolving medium (VC_b). This last equation allows the determination of the time variation of L_a.

The described model is suited to studying the interesting practical situation arising when the crystalline phase consists entirely of nanocrystals.

3.4.2. Case Study: Griseofulvin

The theoretical considerations presented in the previous section (Section 3.4.1) allow establishing the dependence of γ_d on solubility and, thus, nanocrystals radius. Notably, this information is essential for a realistic prediction of the solubility increase with the reduction of nanocrystals dimension, as discussed in Chapter 2 (see eq 2.3.11). In the present case study, the attention is focused on GRI ($C_{17}H_{17}ClO_6$), a drug belonging to Amidon's class II (low water solubility and good permeability) whose physical properties are displayed in Table 3.4.2.1. It is an orally

Table 3.4.2.1. Griseofulvin physicochemical properties. *UCS* indicates the diameter of the unit cell imagined as a sphere, M_w is molecular weight, γ_∞^{sl}, γ_∞^{lv}, and γ_∞^{sv} are, respectively, the solid-liquid, liquid-vapor, and solid-vapor surface energy referring to a plane surface (infinite curvature radius), δ_0 is Tolman's length, ρ_s and ρ_l are, respectively, the solid and liquid density, $T_{m\infty}$ and $\Delta H_{m\infty}$ are, respectively, the melting temperature and enthalpy of the infinitely large crystal, ΔC_P is the difference between the liquid and solid specific heat at constant pressure, V_m is molar volume, while C_s is the solubility in water (37°C).

Formula	**$C_{17}H_{17}ClO_6$**	**Ref**
UCS(nm)	1.45	Puttaraja et al., 1982
M_w(-)	352.77	-
γ_∞^{sl} (J/m^2)	0.0097	Bergese et al., 2004
γ_∞^{lv} (J/m^2)	0.0525	
γ_∞^{sv} (J/m^2)	0.0622	
ρ_s(kg/m^3)	1494.7	
ρ_l(kg/m^3)	1383.1	
$T_{m\infty}$(°C)	220.9	
$\Delta H_{m\infty}$(J/kg)	124400	
ΔC_P(J/kg°C)	511	
V_m(m^3/mole)	$255 \cdot 10^{-6}$	
C_s(µg/cm^3) - 37°C	11.9 ± 0.5	Grassi et al., 2007

Table 3.4.2.2. Estimation of the activity coefficient in water (γ_d) for different drugs in their macrocrystalline state. X_d and C_s represent, respectively, the molar and mass/volume drug solubility, while T is temperature.

Drug	C_s(μg/cm^3)	X_d(-)	T(°C)	γ_d(-)	Source
nimesulide	11.8	$5.285 \cdot 10^{-7}$	37	88148	Table 4.1.1
griseofulvin	11.9	$6.111 \cdot 10^{-7}$	37	45832	Table 3.4.2.1
nifedipine	20.0	$1.046 \cdot 10^{-6}$	37	53339	Table 3.4.2.3
paracetamol	17314.0	$2.066 \cdot 10^{-3}$	30	43	Table 3.4.2.4

Table 3.4.2.3. Nifedipine physicochemical properties. *UCS* indicates the diameter of the unit cell imagined as a sphere, M_w is molecular weight, γ_∞^{sl}, γ_∞^{lv}, and γ_∞^{sv} are, respectively, the solid-liquid, liquid-vapor, and solid-vapor surface energy referring to a plane surface (infinite curvature radius), δ_0 is Tolman's length, ρ_s and ρ_l are, respectively, the solid and liquid density, $T_{m\infty}$ and $\Delta H_{m\infty}$ are, respectively, the melting temperature and enthalpy of the infinitely large crystal, ΔC_P is the difference between the liquid and solid specific heat at constant pressure, V_m is molar volume, while C_s is the solubility in water (37°C).

Formula	$C_{17}H_{18}N_2O_6$	Ref
UCS(nm)	1.47	Triggle et al., 1980
M_w(-)	346.34	-
γ_∞^{sl}(J/m^2)	0.0064	Bergese et al., 2004
γ_∞^{lv}(J/m^2)	0.0461	
γ_∞^{sv}(J/m^2)	0.0525	
ρ_s(kg/m^3)	1375.5	
ρ_l(kg/m^3)	1272.3	
$T_{m\infty}$(°C)	172.8	
$\Delta H_{m\infty}$(J/kg)	107500	
ΔC_P(J/kg°C)	486	
V_m(m^3/mole)	$272 \cdot 10^{-6}$	
C_s(μg/cm^3) - 37°C	20	Hecq et al., 2005

administered antimycotic employed to treat several forms of dermatophytosis, including fungal infections of nails and skin when antifungal creams are ineffective.

The first step consists in evaluating γ_d for GRI in its macrocrystalline state. On the basis of the physical properties displayed in Table 3.4.2.1, eq 2.3.11 allows concluding that γ_d = 45832. This extremely high value reveals that the actual solubility of GRI in water at 37°C is far lower than its ideal value obtained from eq 2.3.11 for γ_d = 1. For this purpose, Table 3.4.2.2 shows γ_d estimation for some poorly water-soluble drugs and paracetamol ($C_8H_9NO_2$), an analgesic and antipyretic

without particular solubility problems. It is evident that paracetamol γ_d is approximately 2-3 orders of magnitude lower than that of poorly water-soluble drugs such as NIF ($C_{17}H_{18}N_2O_6$), an antihypertensive belonging to the class of calcium antagonists and the chemical class of 1,4-dihydropyridines, and NIM ($C_{13}H_{12}N_2O_5S$), a non-steroidal anti-inflammatory (NSAID) with analgesic and antipyretic properties. High values of γ_d are related to a low solubility in a solvent and indicate that the solvent environment is uncomfortable for the drug molecule. On the contrary, low values of γ_d are related to a high solubility in a solvent and indicate a situation approaching ideality, in which the entropy effects become gradually less important in the solution (Granberg and Rasmuson, 1999).

Table 3.4.2.4. Paracetamol physicochemical properties. M_w is molecular weight, $T_{m\infty}$ and $\Delta H_{m\infty}$ are, respectively, the melting temperature and enthalpy of the infinitely large crystal, ΔC_P is the difference between the liquid and solid specific heat at constant pressure, while C_s is the solubility in water (30°C).

Formula	**$C_8H_9NO_2$**	**Ref**
M_w(-)	151.16	Granberg et al., 1999
$T_{m\infty}$(°C)	170.4	
$\Delta H_{m\infty}$(J/kg)	179276.7	
ΔC_P(J/kg°C)	660	
C_s(μg/cm^3) - 30°C	17314	

The second and third steps to determine γ_d dependence on solubility consist in evaluating nanocrystals dimension and solubility. For this purpose, a mixture of crystalline and amorphous GRI was characterized by DSC (Grassi et al., 2007). Briefly, DSC was performed by means of a power compensated Pyris 1 DSC by Perkin Elmer. The sample was placed in an aluminum pan (about 1.8 mg) and then scanned under an N_2 stream of 20 cm^3/min at a heating rate of 10°C/min. Temperature calibration was performed by employing Hg and In as standards. The obtained DSC trace is displayed in Figure 3.4.2.1. It is interesting to observe that, as the endothermic melting peak is around 218.7°C, i.e. below the melting temperature of macrocrystalline GRI (220.9°C), the presence of GRI macrocrystals may be excluded and the crystalline fraction consists of nanocrystals. In order to obtain the nanocrystals size distribution by processing the data depicted in Figure 3.4.2.1 according to the approach discussed in Chapter 4 (Section 4.2), it is necessary to determine the shape of GRI nanocrystals. For this purpose, the WinXMorph program (Kaminsky, 2007) suggests that, although the shape of GRI crystal is complicated (see Figure 3.4.2.2), the choice of a cubic shape is sufficiently close to the actual one. On the basis of this assumption, the

model provides a nanocrystals mass fraction of 0.795, while the amorphous one is 0.205, and the crystals size distribution displayed in Figure 3.4.2.3. Figure 3.4.2.3 clarifies that the distribution peak is around R_{sphere} = 11 nm, equivalent to a cube with a side of 17.75 nm (volume of 5596 nm^3). Although other criteria could be applied, it was decided, in this study, to assume the distribution peak radius as the mean dimension of GRI nanocrystals.

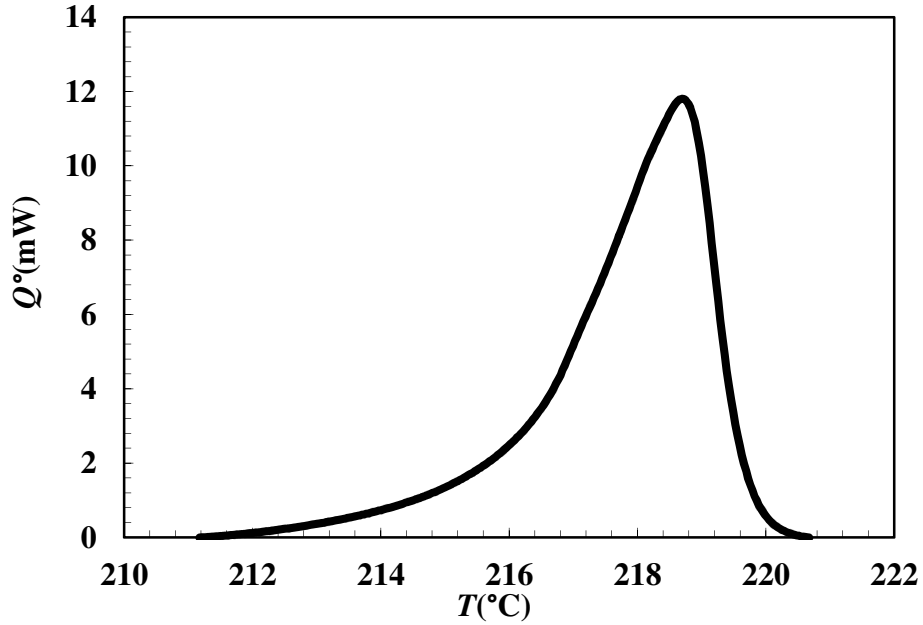

Figure 3.4.2.1. DSC trace referring to a mixture of nanocrystalline and amorphous griseofulvin. T is temperature and $Q°$ indicates the thermal power provided by the instrument.

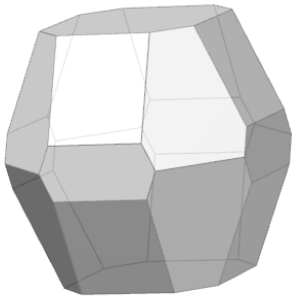

(C) Werner Kaminsky
University of Washington

Figure 3.4.2.2. WinXMorph prediction of griseofulvin crystal shape.

Nanocrystals solubility is then determined by means of the approach described in Section 3.4.1. For this purpose, it is, first, necessary to evaluate the characteristics of amorphous GRI, i.e. C_{si}, k_r,

and k_d by fitting eq 3.4.1.10 to the experimental data shown in Figure 3.4.2.4. In order to overcome the issue connected with the correlation of an elevated number of parameters in eq 3.4.1.10, C_{si}

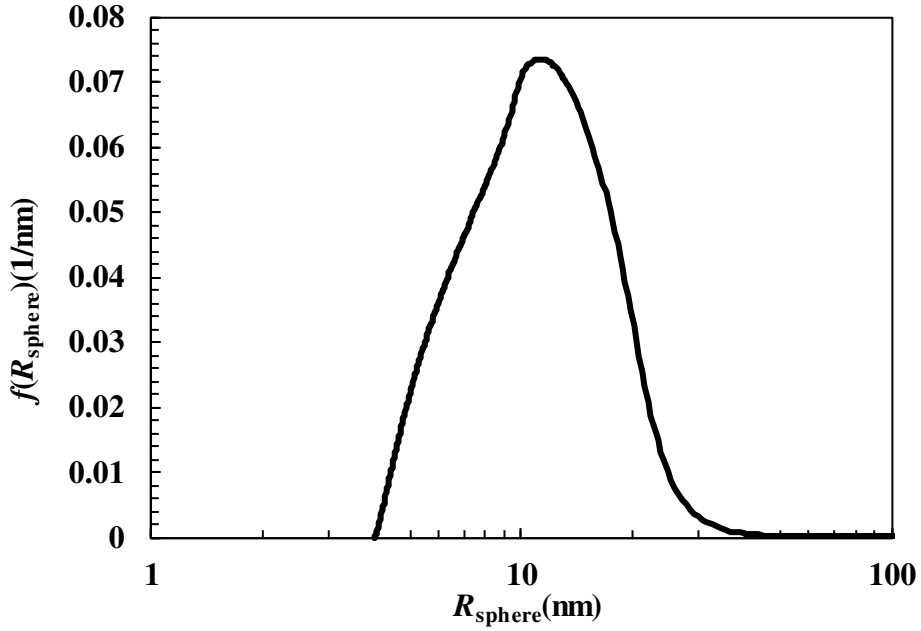

Figure 3.4.2.3. Griseofulvin nanocrystals size distribution referring to the data in Figure 3.4.2.1 opportunely processed according to the approach presented in Chapter 4, Section 4.2. f is frequency and R_{sphere} is the radius of the sphere having the same volume of the cubic nanocrystal.

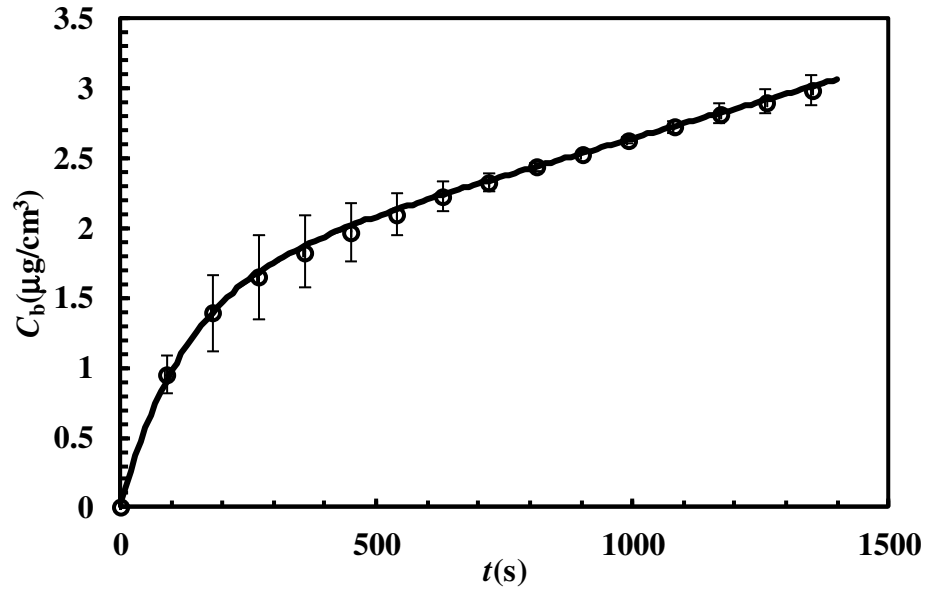

Figure 3.4.2.4. Equation 3.4.1.10 best fit (solid line) to the experimental IDR data (symbols) referring to amorphous griseofulvin (T = 37°C; V = 250 cm^3; S = 3.14 cm^2). The vertical bars indicate the standard deviations (data from Grassi et al., 2007).

and k_d are evaluated according to the strategy illustrated immediately after the introduction of eq

3.4.1.10, thus obtaining $k_d = 3.41 \cdot 10^{-5}$ m/s and $C_{si} = 0.250$ kg/m^3. This last value, in particular, appears to agree with Murdande's theoretical prediction (Murdande et al., 2010). Hence, for $C_{si} = 0.250$ kg/m^3, $k_d = 4.33 \cdot 10^{-5}$ m/s (very close to the initial guess $3.41 \cdot 10^{-5}$ m/s), $k_r = 8.0 \cdot 10^{-3}$ s^{-1}, and $C_{sf} = 0.022$ kg/m^3 as fitting parameters, eq 3.4.1.10 provides a good fit (see Figure 3.4.2.4). The fact that the estimation of C_{sf} is higher than the actual macrocrystalline solubility (0.0119 kg/m^3) is scarcely surprising since a much longer dissolution time should have been considered.

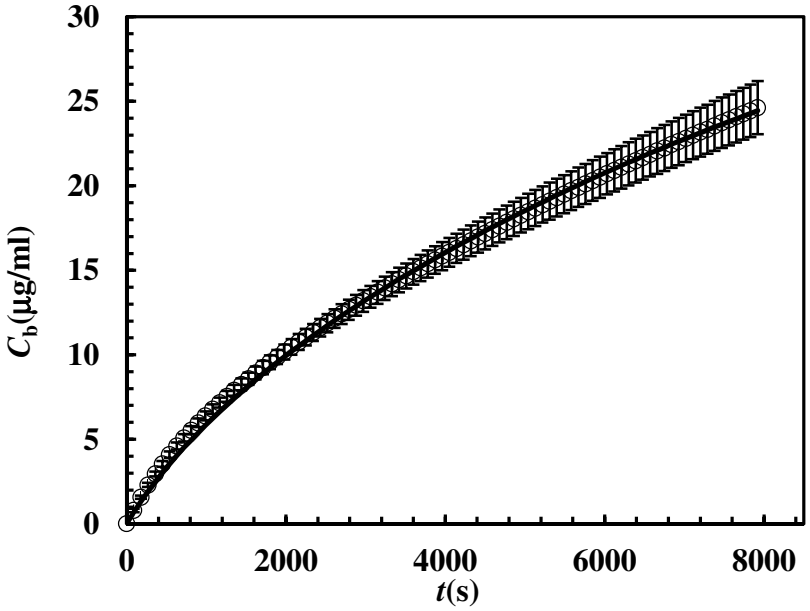

Figure 3.4.2.5. Equations 3.4.1.13 – 3.4.1.15 best fit (solid line) to the experimental IDR data (symbols) referring to a nanocrystalline/amorphous griseofulvin mixture ($T = 37$°C; $V = 250$ cm^3; $S = 3.14$ cm^2). The vertical bars indicate the standard deviations (data from Grassi et al., 2007).

Nevertheless, this would have meant exceeding the sink conditions, the range in which the determination of both k_d and k_r is much more reliable. On the basis of these results, it was possible to fit eqs 3.4.1.13 – 3.4.1.15 to the experimental data referring to a nanocrystalline/amorphous mixture and displayed in Figure 3.4.2.5. In order to reduce the number of fitting parameters, the physical quantity τ/D_{d0} (see eq 3.4.1.13) was set equal to 10^9 s/m^2 since τ ranges from 1 to 3 and D_{d0}, for small organic drugs such as GRI, is approximately 10^{-9} m^2/s in water at 37°C (Grassi et al., 2007). C_{sf} (0.25 kg/m^3), C_{si} (0.022 kg/m^3), k_d ($4.3 \cdot 10^{-5}$ m/s), and X_{nc} (0.795) were chosen according to what previously found, while C_{sc} and k_r were considered the only fitting parameters. As shown in Figure 3.4.2.5, a good fit is obtained with $C_{sc} = 0.05$ kg/m^3 and $k_r = 6.4 \cdot 10^{-4}$ s^{-1}. k_r difference from the amorphous drug one obtained by IDR would allow supposing that this parameter may be also affected by the external environment/concentration. However, this last data fitting allows determining the solubility of cubic nanocrystals whose average volume is 5596 nm^3,

equivalent to R_{sphere} = 11 nm. This is a very important information as it allows establishing a relation between nanocrystals dimension and solubility. The knowledge of nanocrystals solubility and dimension allows the evaluation of γ_d as the developed thermodynamic model (see Chapter 2) concludes that T_m = 217.4°C and ΔH_m = 121393 J/kg, while ΔC_P = 511 J/kg°C. Thus, eq 2.3.11 yields γ_d = 12678 for GRI nanocrystals. As this value is lower than the one of GRI macrocrystals (45832), nanocrystals solubility is closer to the ideal one than macrocrystals solubility. Finally, it is possible to evaluate γ_d for the smallest (theoretical) nanocrystal, i.e. that characterized by the

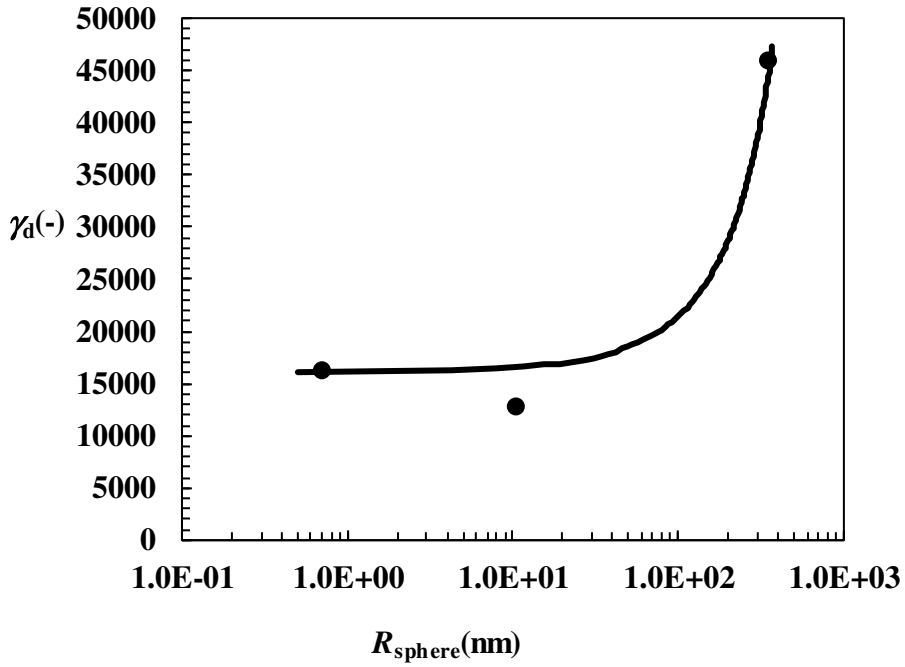

Figure 3.4.2.6. Activity coefficient (γ_d) dependence on nanocrystal dimension represented by the radius of the sphere (R_{sphere}) having the same volume of the nanocrystal. The solid line indicates the trend of eq 3.4.1.20, while the dots represent the experimental data.

same volume of GRI primitive cell (1.6 nm^3; R_{sphere} = 0.726 nm). Indeed, the developed thermodynamic model predicts T_m = 162.3°C and ΔH_m = 75719 J/kg, while ΔC_P = 511 J/kg°C. In addition, by associating the solubility of amorphous GRI (0.25 kg/m^3) with its primitive cell (a vanishingly small nanocrystal), eq 2.3.11 yields γ_d = 16054. Figure 3.4.2.6, by summarizing all these findings referring to γ_d evaluation, helps to clarify that γ_d substantially decreases with crystal dimension (R_{sphere}) and this trend may be approximated by the following exponential function:

$$\gamma_d = 16054 e^{0.002917(R_{sphere}-0.726)} \qquad (3.4.2.1)$$

The substitution of this expression in eq 2.3.11 provides the actual tendency of solubility to increase with R_{sphere}. In particular, Figure 3.4.2.7 displays the comparison between the ideal and actual increments of the ratio $C_s/C_{s\infty}$ as a function of crystal dimension (R_{sphere}). As γ_d reduces with crystal size, the actual increment of $C_s/C_{s\infty}$ exceeds the ideal one, in which γ_d is constantly equal to one.

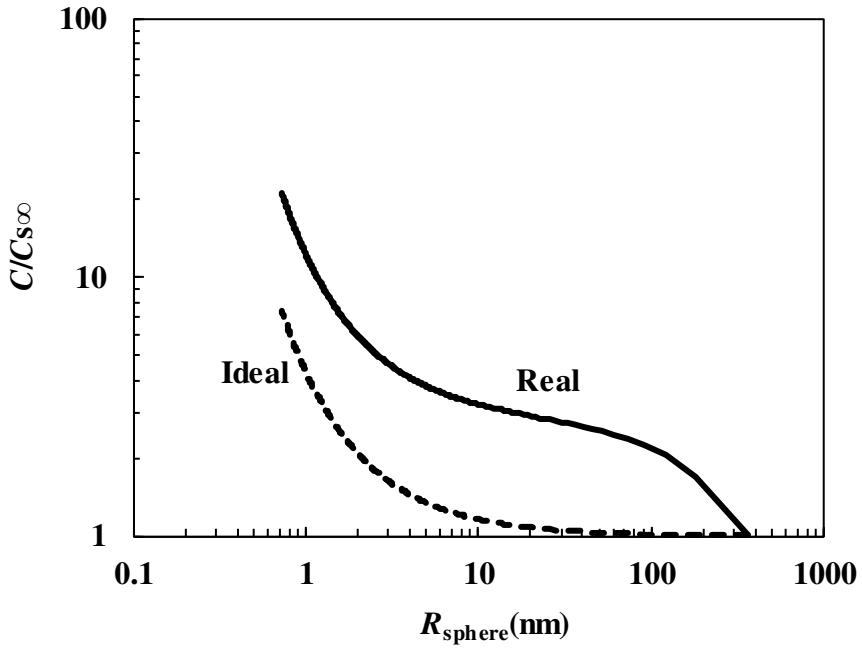

Figure 3.4.2.7. Ideal and actual relative increase in griseofulvin solubility (C) as a function of nanocrystal size represented by the radius of the sphere (R_{sphere}) having the same volume of the nanocrystal. $C_{s\infty}$ is the solubility of an infinitely large nanocrystal (i.e. a macrocrystal).

3.4.3. Case Study: Vinpocetine

Vinpocetine (VIN, $C_{22}H_{26}N_2O_2$) is a semisynthetic derivative of Vinca minor L. alkaloid vincamine employed to treat cognitive disorders and related symptoms such as cerebral infarction, cerebral hemorrhage residual effects, and cerebral arteries cirrhosis effects (Csanda et al., 1988; Lorincz et al., 1976). This basic drug (pK_a = 7.1) (Weinshaar and Bristol, 1990) was taken into consideration because it is practically insoluble in water (1.6 μg/cm^3 at pH = 7.4 and 37°C) (Hasa et al., 2011). Its physicochemical properties are displayed in Table 3.4.3.1. VIN physical properties when combined with eq 2.3.11 yield γ_d = 911460, an extremely high value witnessing the very scarce affinity of VIN for water. Interestingly, this value is approximately one order of magnitude

higher than those referring to NIM, NIF, and GRI, while it is four orders of magnitude greater than

Table 3.4.3.1. Vinpocetine physicochemical properties. *UCS* indicates the diameter of the unit cell imagined as a sphere, M_w is molecular weight, γ_∞^{sl}, γ_∞^{lv}, and γ_∞^{sv} are, respectively, the solid-liquid, liquid-vapor, and solid-vapor surface energy referring to a plane surface (infinite curvature radius), δ_0 is Tolman's length, ρ_s and ρ_l are, respectively, the solid and liquid density, $T_{m\infty}$ and $\Delta H_{m\infty}$ are, respectively, the melting temperature and enthalpy of the infinitely large crystal, ΔC_P is the difference between the liquid and solid specific heat at constant pressure, V_m is molar volume, while C_s is the solubility in water (37°C).

Formula	**$C_{17}H_{18}N_2O_6$**	**Ref**
UCS(nm)	1.2	Hasa et al., 2011
M_w(-)	350.45	
γ_∞^{sl}(J/m^2)	0.0072	
γ_∞^{lv}(J/m^2)	0.0312	
γ_∞^{sv}(J/m^2)	0.0384	
ρ_s(kg/m^3)	1268	
ρ_l(kg/m^3)	1217	
$T_{m\infty}$(°C)	149.6	
$\Delta H_{m\infty}$(J/kg)	94600	
ΔC_P(J/kg°C)	374	
V_m(m^3/mole)	$287 \cdot 10^{-6}$	
C_s(μg/cm^3) - 37°C, pH 7.4	1.6	

that of paracetamol (see Table 3.4.2.4). As in the case of GRI, the evaluation of γ_d for VIN unit cell (the smallest VIN crystal) may be conducted by resorting to eq 2.3.11 and assuming that its solubility is 22 μg/cm^3, i.e. the one of amorphous VIN (Hasa et al., 2011), T_m = 37°C and ΔH_m = 26174 J/kg according to the developed thermodynamic model (see Chapter 2 and Figure 3.4.3.1), while ΔC_P = 374 J/kg°C. This approach leads to γ_d = 879223. In this case, unlike GRI, a very small variation of γ_d results from considering macrocrystalline VIN. Thus, a simple γ_d linear dependence on R_{sphere} may be assumed. By embodying this law in eq 2.3.11, the actual trend of $C/C_{s\infty}$ as a function of R_{sphere} is obtained, as depicted in Figure 3.4.3.2. It may be noticed that the actual behavior substantially follows the ideal one.

VIN case study represents a possible general strategy to evaluate $\gamma_d(R_{sphere})$ for a generic drug provided that its amorphous/macrocrystalline solubility and thermodynamic properties are known, for instance, those displayed in Table 3.4.3.1.

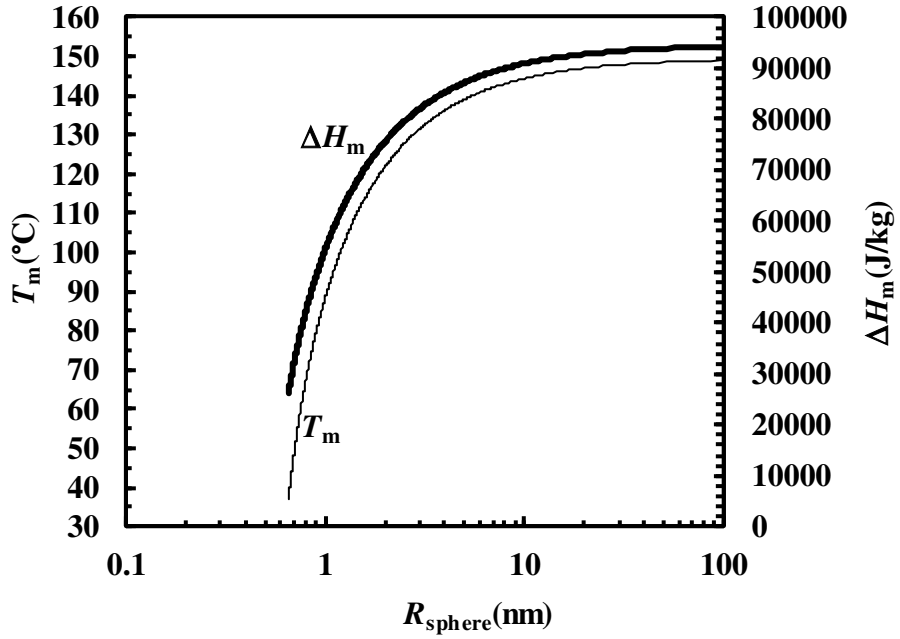

Figure 3.4.3.1. Vinpocetine. Reduction of the melting temperature (T_m) and enthalpy (ΔH_m) as a function of crystal dimension represented by the radius of the sphere (R_{sphere}) having the same volume of the crystal. The shape of vinpocetine crystals is assumed cubic.

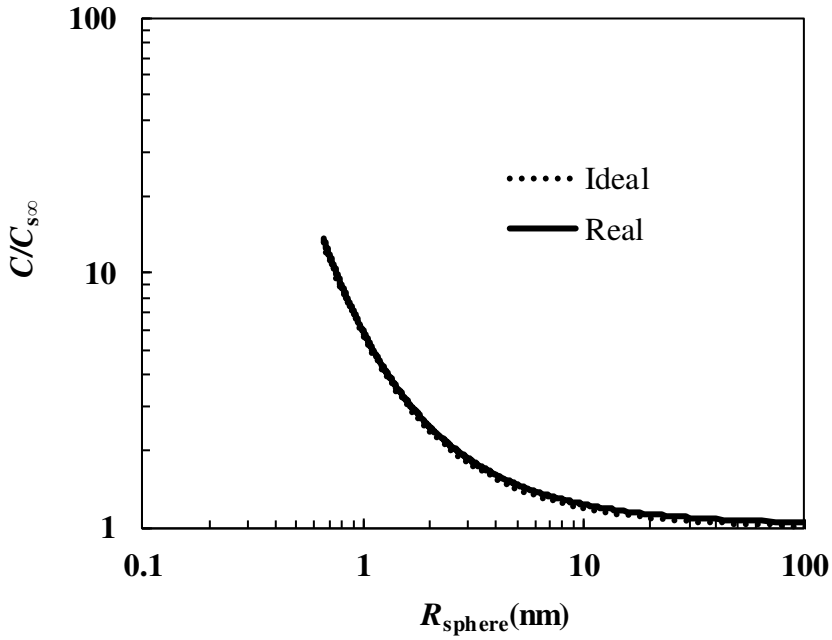

Figure 3.4.3.2. Ideal and actual relative increase in vinpocetine solubility (C) as a function of nanocrystal size represented by the radius of the sphere (R_{sphere}) having the same volume of the nanocrystal. $C_{s\infty}$ is the solubility of an infinitely large nanocrystal (i.e. a macrocrystal).

3.5. Conclusions

This chapter provides a way to validate the thermodynamic model proposed in Chapter 2 by resorting to a molecular dynamics approach (Section 3.2) and other theoretical considerations based on the comparison with a previous model (Gibbs-Thomson's equation) and the nucleation theory (Section 3.3). By considering three drugs of class II (poorly soluble and permeable drugs – nimesulide, nifedipine, and griseofulvin), the molecular dynamics approach substantially confirms the prediction of the thermodynamic model concerning the melting temperature and enthalpy reduction with crystals size. In addition, in the light of the nucleation theory, the output of the presented thermodynamic model appears much more reasonable than that of a previous well-known approach (Gibbs-Thomson's equation).

The final part of this chapter (Section 3.4) provides an attempt to exploit the thermodynamic model to evaluate the dependence of the drug activity coefficient in a solution on drug nanocrystals dimension. Indeed, only by knowing this property, it is possible to predict the actual increase in solubility when nanocrystals size decrease. It appears to be the first attempt to predict the solubility increase by also considering the non-ideal solution properties.

CHAPTER 4

MODEL OUTCOMES

4.1 Theoretical Results

To perform a sound comparison among the thermal properties of differently shaped crystals, it is no longer possible to refer to sphere radius (R_s), parallelepiped base side (a_s), and cylinder base radius (R_s). Indeed, in doing so, the melting temperature (T_m) and enthalpy (ΔH_m) of crystals having different volumes and, thus, different masses would be compared. As melting is a bulk phenomenon (although it starts from surface), the comparison of the thermal properties should be referred to nanocrystals characterized by equal volume V_C (sphere $4\pi R_s^3/3$; parallelepiped $a_s b_s c_s$; cylinder $\pi R_s^2 L_s$) and, consequently, different R_s and a_s. Accordingly, eqs 2.2.1.8 – 2.2.1.9, 2.2.2.6 – 2.2.2.7, and 2.2.3.6 – 2.2.3.7 were solved as functions of R_s (sphere), a_s (parallelepiped), and R_s (cylinder), respectively. By knowing $T_m(a_s$ or $R_s)$ and $\Delta H_m(a_s$ or $R_s)$, it was, then, possible to develop and compare the corresponding trends $T_m(V_C)$ and $\Delta H_m(V_C)$ for the three different considered geometries. Model features were explored by considering nimesulide (NIM) as a proof of concept (see Table 4.1.1 displaying the NIM physicochemical parameters required for the simulations). Indeed, NIM is a typical non-steroidal anti-inflammatory drug characterized by a low bioavailability due to its low water solubility (Davis and Brogden, 1994; Cignarella et al., 1996). Figure 4.1.1, showing the T_m and ΔH_m depression in the case of parallelepiped-shaped crystals characterized by $X_{nc} = 1$ and a square basis ($\beta = a_s/b_s = 1$), clarifies the effect of the shape ratio ξ ($= c_s/a_s$) (the representation is inferiorly limited to the volume of approximately four NIM unit cells ≈ 11 nm^3). It is observable that the shape ratio ξ affects in a qualitatively similar manner both T_m and ΔH_m, even if its effect appears more accentuated for T_m. In particular, Figure 4.1.1 shows that, at fixed crystal volume (V_C), platelet nanocrystals ($\xi = 0.01$) are characterized by lower T_m and ΔH_m than rod-shaped ($\xi = 100$) nanocrystals. In addition, both of them show lower T_m and

ΔH_m than cubic nanocrystals. Conversely, at fixed T_m or ΔH_m, cubic crystals are characterized by the smallest dimensions among the other shapes (rods and platelets). It is worth mentioning that

Table 4.1.1. Nimesulide physicochemical parameters. *UCS* indicates the diameter of the unit cell imagined as a sphere, M_w is the molecular weight, γ_∞^{sl}, γ_∞^{lv}, and γ_∞^{sv} are, respectively, the solid-liquid, liquid-vapor, and solid-vapor surface energy referring to a plane surface (infinite curvature radius), δ_0 is Tolman's length, ρ_s and ρ_l are, respectively, the solid and liquid density, $T_{m\infty}$ and $\Delta H_{m\infty}$ are, respectively, the melting temperature and enthalpy of the infinitely large crystal, ΔC_P is the difference between the liquid and solid specific heat at constant pressure, V_m is the molar volume, while C_s is the solubility in water (37°C) (data from Chiarappa et al., 2017).

Formula	$C_{13}H_{12}N_2O_5S$
UCS (nm)	1.74
M_w (–)	308.51
γ_∞^{sl} (J/m^2)	0.0133
γ_∞^{lv} (J/m^2)	0.0433
γ_∞^{sv} (J/m^2)	0.0576
δ_0 (nm)	0.2385
ρ_s (kg/m^3)	1490.0
ρ_l (kg/m^3)	1343.7
$T_{m\infty}$ (°C)	148.7
$\Delta H_{m\infty}$ (J/kg)	108720
ΔC_P (J/kg°C)	333.3
V_m (m^3/mole)	$192 \cdot 10^{-6}$
C_s (µg/cm^3) – 37°C, pH 1.2	11.8 ± 0.5
C_s (µg/cm^3) – 37°C, pH 7.5	104 ± 12

the relation existing between T_m and V_C is substantially compatible with the outcomes of the nucleation theory, which allows determining the size (V_C) of the smallest nucleus (namely a cluster of molecules) which a crystal originates from (Hamilton et al., 2012).

This model output is explicable by remembering the theoretical expression of the melting temperature/enthalpy dependence on the surface and bulk atoms number in the case of parallelepiped-shaped nanocrystals theorized by Magomedov (Magomedov, 2004; Magomedov, 2011). This, fundamentally, underlines the importance of the ratio between the surface and bulk

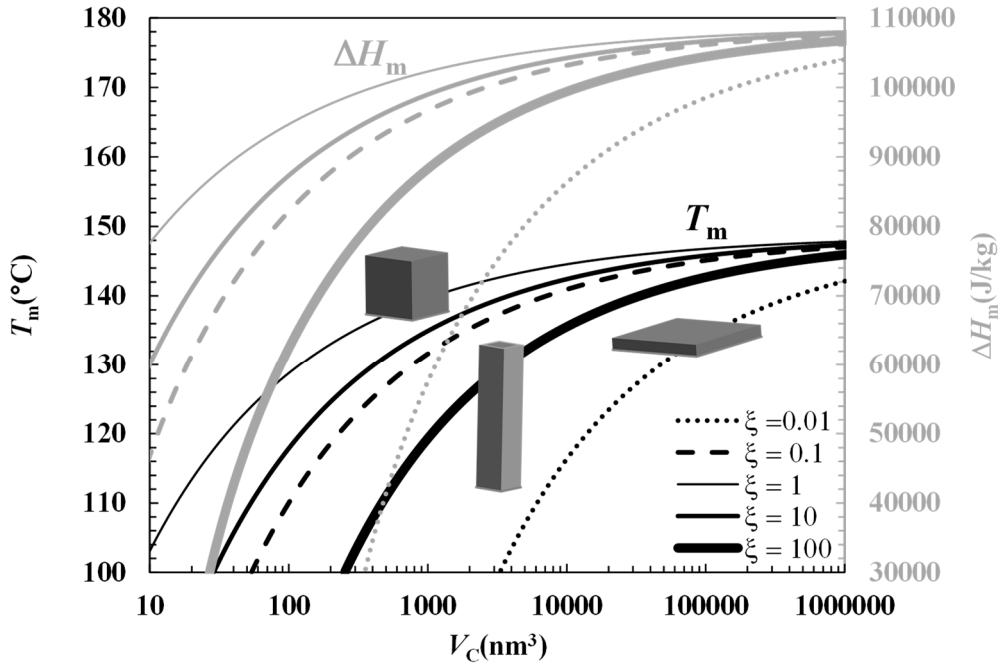

Figure 4.1.1. Effect of the shape ratio $\xi = c_s/a_s$ on the melting temperature T_m (left vertical axis, black lines) and enthalpy ΔH_m (right vertical axis, gray lines) of parallelepiped-shaped nanocrystals, when assuming the nanocrystals mass fraction $X_{nc} = 1$ and $\beta = a_s/b_s = 1$. a_s, b_s, and c_s are the dimensions of the parallelepiped-shaped crystal, while V_C is the crystal volume. The shaded parallelepipeds qualitatively represent the shape of the crystals pertaining to the curve they intersect.

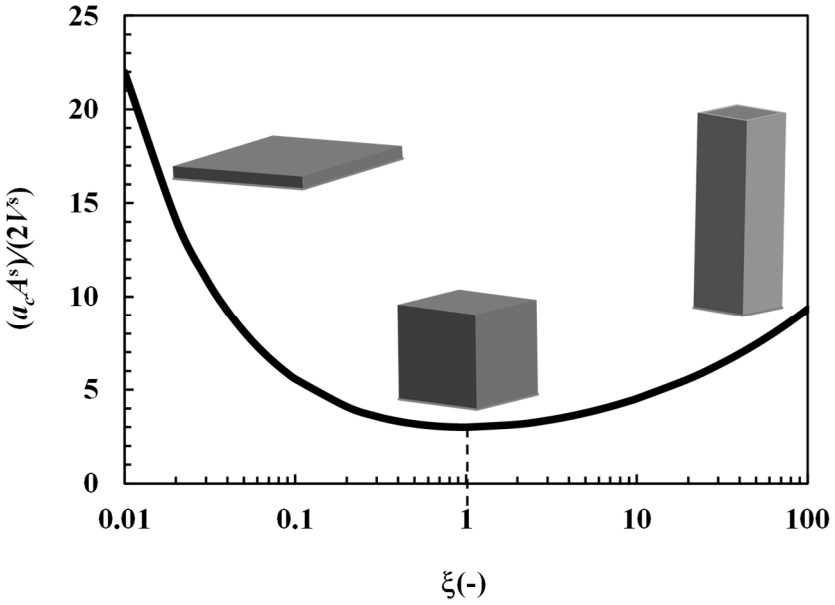

Figure 4.1.2. Equation 4.1.1 plot showing the dependence of the dimensionless ratio between crystal surface (A^s) and volume (V^s) on the shape ratio $\xi = c_s/a_c$ at constant volume. The value $\beta = b_s/a_c = 1$ was assumed to perform a coherent connection with Figure 4.1.1. The shaded parallelepipeds qualitatively represent the shape of the crystals pertaining to the different ξ values.

atoms/molecules. Indeed, at constant volume (V_C), cubic crystals show the minimum surface-volume ratio with respect to the other conformations (rods and platelets), as witnessed by eq 4.1.1 and Figure 4.1.2:

$$\frac{a_c}{2}\frac{A^s}{V^s} = \sqrt[3]{\beta}\left[\sqrt[3]{\frac{1}{\xi^2}} + \sqrt[3]{\xi}\left(1+\frac{1}{\beta}\right)\right] \tag{4.1.1}$$

where a_c stands for the side of the cube, while A^s and V^s (= V_C = $a_c b_c c_c$) are the surface and the volume of the crystal, respectively. Additionally, the higher surface-volume ratio shown by platelet crystals with respect to rod crystals (Figure 4.1.2) explains why platelet crystals are characterized by lower T_m and ΔH_m in comparison to rod crystals. In the case of cylindrical

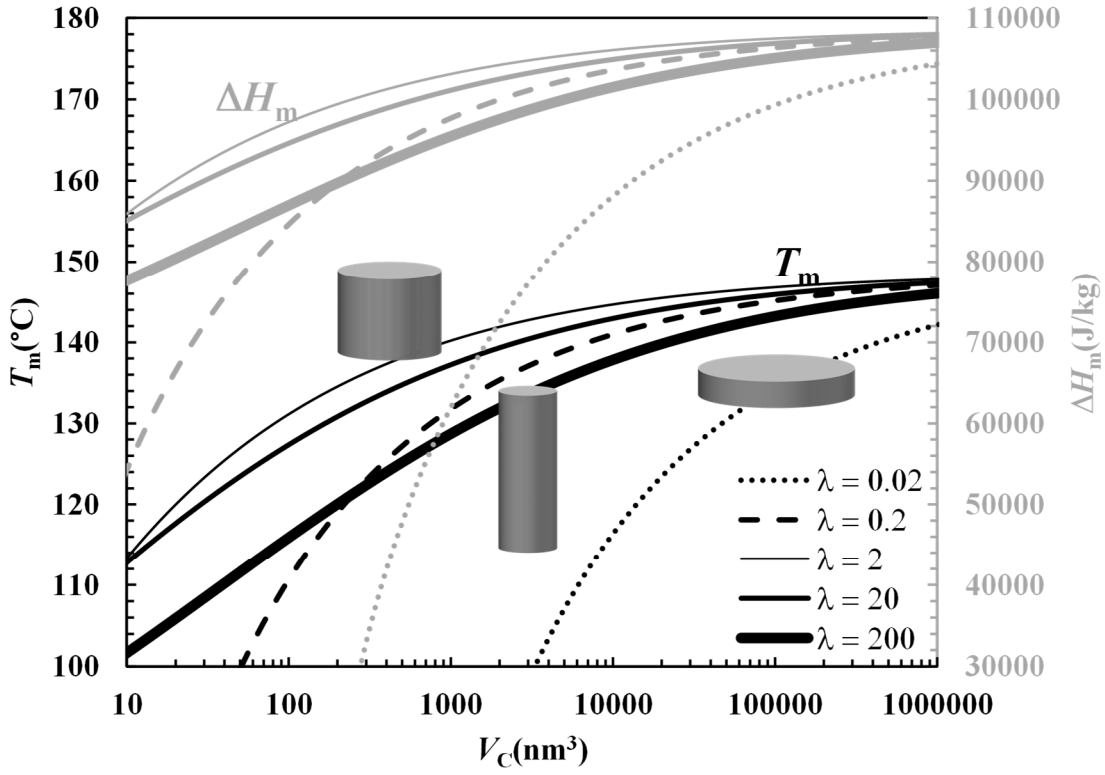

Figure 4.1.3. Effect of the shape ratio $\lambda = L_s/R_s$ on the melting temperature T_m (left vertical axis, black lines) and enthalpy ΔH_m (right vertical axis, gray lines) of cylindrical nanocrystals, when assuming the nanocrystals mass fraction $X_{nc} = 1$. L_s and R_s are the length and the radius of the cylindrical-shaped crystal, while V_C is the crystal volume. The shaded cylinders qualitatively represent the shape of the crystals pertaining to the curve they intersect.

crystals, model results (eqs 2.2.3.6 – 2.2.3.7) are qualitatively similar to those found for parallelepipeds. Indeed, Figure 4.1.3, showing the effect of the shape ratio λ on T_m and ΔH_m

depression, reveals that rod-shaped (λ = 200; black/gray solid thickest lines) and platelet-shaped (λ = 0.02; black/gray dotted lines) crystals are characterized by more consistent reductions of T_m and ΔH_m than those referring to the equilateral cylinder (λ = 2; black/gray solid thinnest lines) (the representation is inferiorly limited to the volume of approximately four NIM unit cells ≈ 11 nm^3). However, since the surface-volume ratio of the equilateral cylinder is close to the one of rod-shaped crystals (see Figure 4.1.4):

$$\frac{A^s R_s}{V^s} = \sqrt[3]{\frac{4}{\lambda^2}} + \sqrt[3]{4\lambda} \tag{4.1.2}$$

the T_m and ΔH_m trends of rod-shaped crystals are less detached from those of the equilateral one differently from the case of parallelepiped-shaped crystals (Figure 4.1.1). It is important to remind

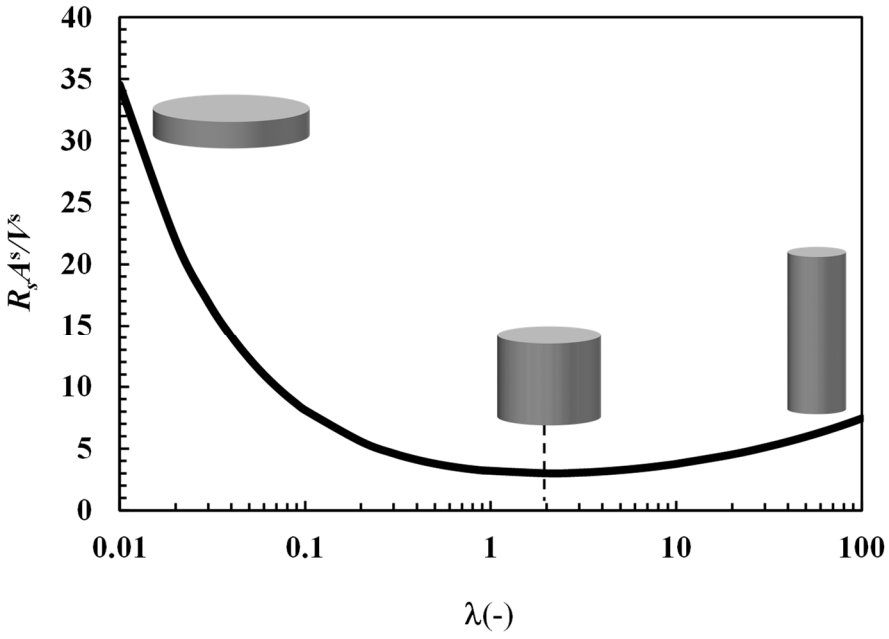

Figure 4.1.4. Equation 4.1.2 plot showing the dependence of the dimensionless ratio between crystal surface (A^s) and volume (V^s) on the shape ratio λ = L_s/R_s at constant volume. The shaded cylinders qualitatively represent the shape of the crystals pertaining to the different λ values.

that the value of X_{nc} appears to slightly affect the results shown in Figure 4.1.1 and Figure 4.1.3, where X_{nc} = 1 was considered. However, the reduction of X_{nc} is reflected in a decrease of both T_m and ΔH_m, being V_C the same.

It is now interesting to evaluate the effect of nanocrystals shape (sphere, cube (ξ = β = 1), and equilateral cylinder (λ = 2)) on T_m and ΔH_m depression. Figure 4.1.5, concerning the melting

process of spherical, cubic, and (equilateral) cylindrical crystals, clarifies that, at equal crystal volume (V_C), T_m and ΔH_m of cubic nanocrystals are lower than those of cylindrical nanocrystals. In turn, cylindrical nanocrystals show lower T_m and ΔH_m with respect to spherical nanocrystals. The explanation of this behavior relies on both the dimensionless surface-volume ratio (cube → 3; equilateral cylinder → 2; sphere → 3) and the reduction of surface energy with surface curvature ($1/r$, see eq 2.2.1.3). Indeed, not only cubic crystals are characterized by the highest value of the surface-volume ratio but they also show the highest surface energy as they are constituted by plane surfaces (curvature = $1/r \rightarrow 0$).

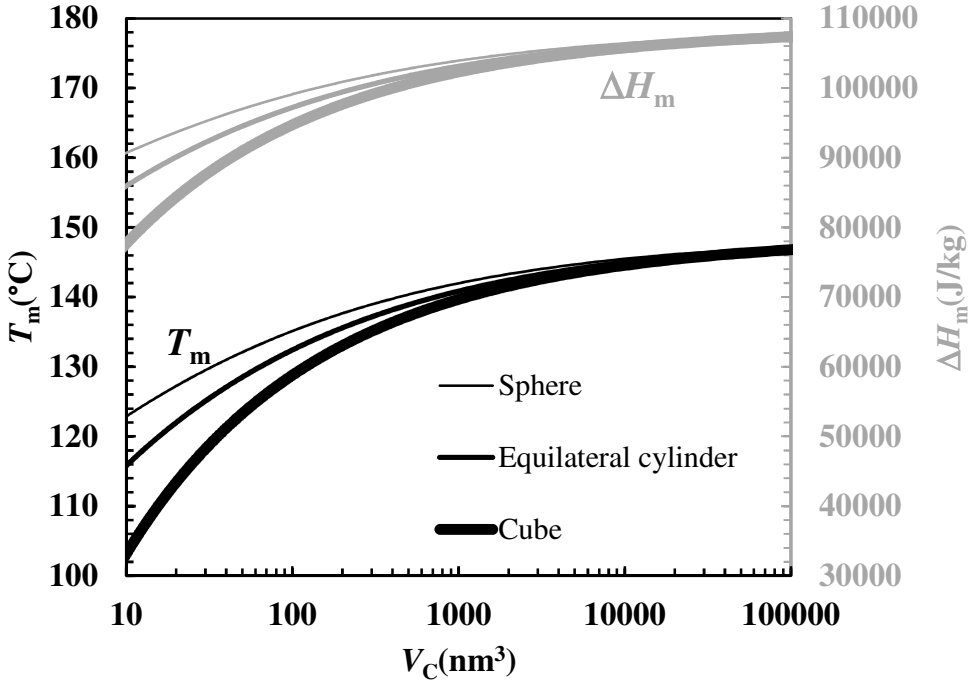

Figure 4.1.5. Effect of geometry (sphere, cube ($\xi = \beta = 1$), equilateral cylinder ($\lambda = 2$)) on melting temperature T_m (left vertical axis, black lines) and enthalpy ΔH_m (right vertical axis, gray lines) depression, when assuming the nanocrystals mass fraction $X_{nc} = 1$. The representation is inferiorly limited to the volume of approximately four nimesulide unit cells ≈ 11 nm^3.

On the contrary, spherical crystals, although characterized by the same surface-volume ratio (3), suffer from the reduction of surface energy with curvature, this last one increasing as crystal radius decreases. Equation 2.27b clarifies that, for vanishingly small values of γ^{lv} and γ^{sl}, T_m and ΔH_m are independent of sphere radius. Cylindrical crystals are in between the spherical and cubic ones as they are characterized by the smallest surface-volume ratio, but the effect of curvature affects only the lateral surface and not the two bases.

4.2 Practical Results

The findings of this study are reflected in two crucial and practical aspects characterizing nanocrystals based delivery systems, i.e. the nanocrystals size distribution inside a polymeric carrier and nanocrystals water solubility. For this purpose, it is worthwhile to take into consideration the work performed by Coceani and collaborators (Coceani et al., 2012) on NIM loaded into a stabilizing polymeric matrix constituted by cross-linked polyvinylpyrrolidone (PVP Cl-M), a white, tasteless, odorless, and water-insoluble powder obtained by popcorn polymerization.

NIM/PVP Cl-M physical mixtures (ratio 1:3, w/w) were co-ground for 0.5, 1, 2, and 4 h in a planetary mill rotating at 350 rpm and, then, analyzed with a differential scanning calorimeter (DSC) in order to determine the fraction of the original macrocrystalline drug (X_{mc}) and that of the newly formed nanocrystalline (X_{nc}) or amorphous (X_{am}) one.

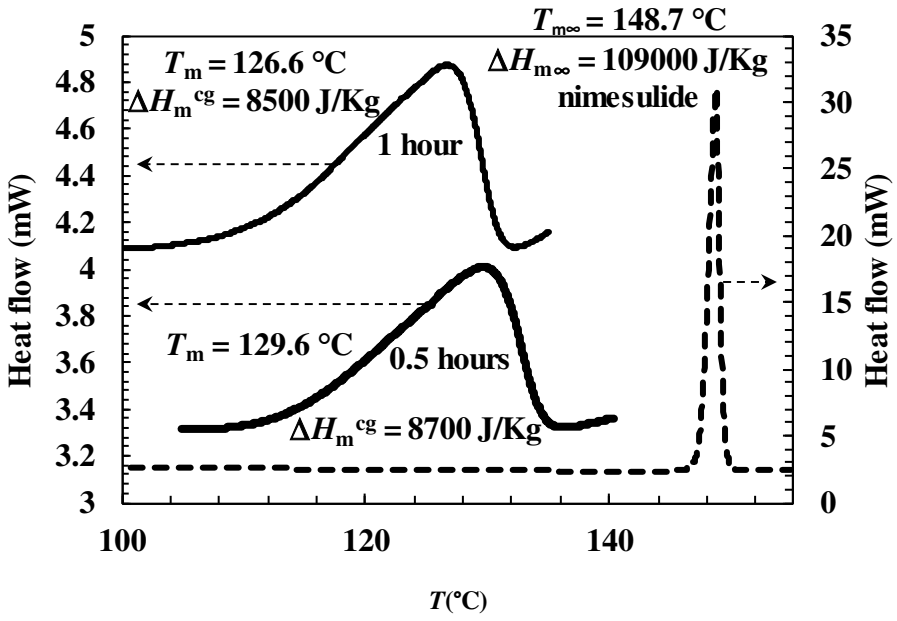

Figure 4.2.1. Pure nimesulide (dotted line), 0.5 h (thick line), and 1 h co-ground system (thin line) thermograms performed by differential scanning calorimetry. The reduction of melting temperature T_m and enthalpy ΔH_m^{cg} for the two co-ground systems is clearly evident (from Coceani et al., 2012).

Figure 4.2.1 displays the pure NIM melting peak (dotted line; $T_{m\infty}$ = 148.7°C, $\Delta H_{m\infty}$ = 109000 J/kg) and the DSC profiles of two co-ground systems (0.5 h, thick line; 1 h, thin line). While the 0.5 h co-ground system shows a melting peak at 129.6°C requiring 8700 J/kg, the 1 h one decreases to 126.6°C and 8500 J/kg. Figure 4.2.1 clarifies that simply 0.5 h is sufficient to completely destroy the original macrocrystals into nanocrystals (X_{mc} = 0), as no thermal event occurs at the pure NIM

melting temperature. Similarly, Figure 4.2.2 displays the DSC profiles relative to two other co-ground systems (2 h, thick line; 4 h, thin line). The 2 h DSC curve shows a melting event at 118°C

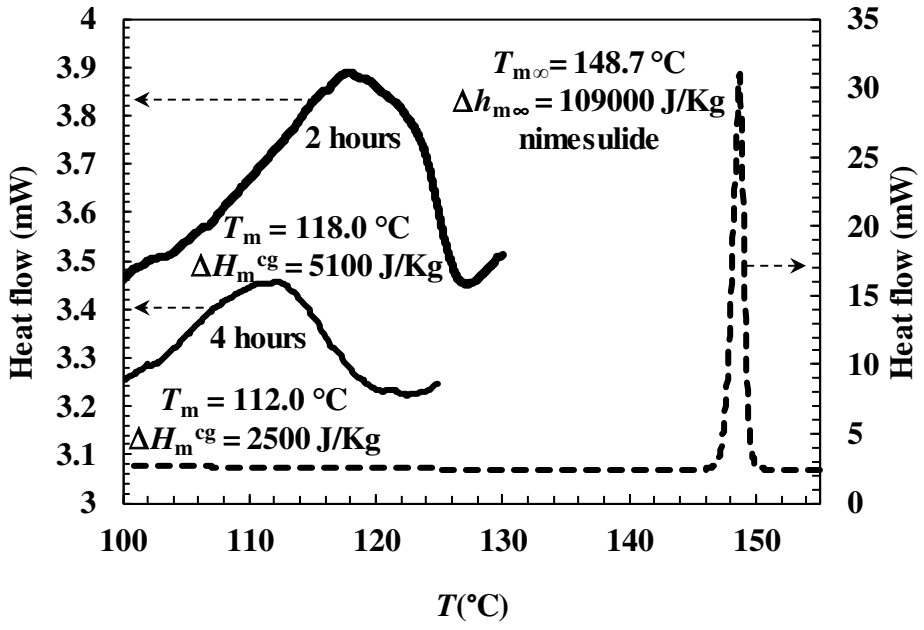

Figure 4.2.2. Pure nimesulide (dotted line), 2 h (thick line), and 4 h co-ground system (thin line) thermograms performed by differential scanning calorimetry. The reduction of melting temperature T_m and enthalpy ΔH_m^{cg} is more pronounced than the 0.5 and 1 h co-ground systems (from Coceani et al., 2012).

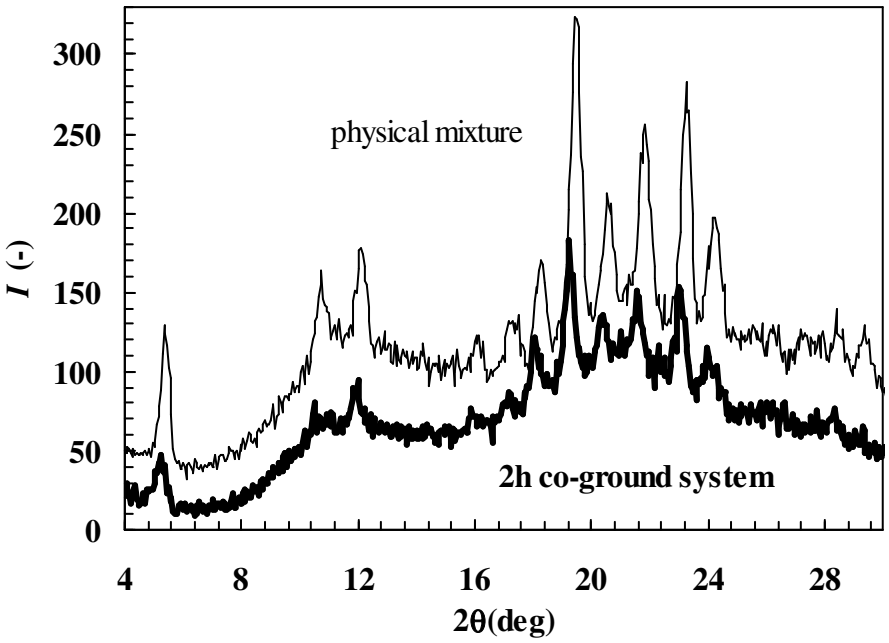

Figure 4.2.3. Comparison between the XRPD pattern relative to a PVP Cl-M/nimesulide (3/1, w/w) physical mixture (thin line) and the 2 h co-ground system (thick line). No substantial modifications of the XRPD pattern derive from co-grinding, meaning that no drug polymorphs were formed (from Coceani et al., 2012).

requiring 5100 J/kg, while the 4 h curve is characterized by a melting peak occurring at 112 °C after 2500 J/kg heat. Figure 4.2.3 shows the comparison between the X-rays powder diffraction (XRPD) patterns relative to the physical mixture and the same mixture after two-hour milling. It is possible to notice that no substantial shift of the typical NIM diffraction peaks (occurring at 2θ = 5, 11, 12, 18, 19.5, 21, 22, 23, and 24.3) arises. As analog diffraction patterns may be obtained for the other grinding times (0.5, 1, and 4 h), it was concluded that no polymorphs were generated during grinding.

Furthermore, the determination of the aforementioned drug fractions, in the case of spherical crystals, was also theoretically achieved by means of the iterative simultaneous numerical solution of eqs 2.2.1.8 and 2.2.1.9, explained in paragraph 2.2.1, which starts by making a reasonable first guess of X_{nc}. Once a first estimation of the drug specific melting enthalpy per unit mass (ΔH_m) as a function of drug crystal radius is obtained, X_{nc} is recalculated according to:

$$X_{nc} = \frac{\Delta H_m^{cg}(\omega_d)}{\Delta H_{m\infty}^{mix}(\omega_d) - \omega_d\left(\Delta H_{R_s} + \Delta H_T\right)} \tag{4.2.1}$$

where ΔH_m^{cg} is the experimental co-ground system specific melting enthalpy per unit mass (owed to drug melting only, as the polymeric carrier is amorphous) at T_m, i.e. the melting temperature of drug nanocrystals with radius R_s, ω_d is the drug mass fraction characterizing both the physical mixture and the co-ground system, $\Delta H_{m\infty}^{mix}$ is the experimental physical mixture specific melting enthalpy per unit mass at $T_{m\infty}$, i.e. drug macrocrystals melting temperature, while ΔH_{R_s} and ΔH_T are, respectively, the second and the third term in the right-hand side of eq 2.2.1.9. If the relative difference between X_{nc} calculated according to eq 4.2.1 and the initially guessed one is lower than a fixed tolerance, the iterative procedure ends by providing the theoretical value of X_{nc}. On the contrary, the procedure is repeated by assuming the new value of X_{nc} as:

$$X_{nc} = X_{nc}^{old}(1-\lambda) + \lambda X_{nc}^{new} \tag{4.2.2}$$

where λ is a relaxation parameter ranging from 0 to 1, X_{nc}^{old} and X_{nc}^{new} represent, respectively, the X_{nc} value assumed at the beginning of the i^{th} iterative loop and that recalculated according to eq 4.2.1 at the end of the same loop. The procedure is repeated until the aforesaid relative difference test is passed. Obviously, the determination of X_{mc} simply requires the evaluation of:

$$X_{mc} = \frac{\Delta H_{m\infty}^{cg}(\omega_d)}{\Delta H_{m\infty}^{mix}(\omega_d)} \tag{4.2.3}$$

where $\Delta H_{m\infty}^{cg}$ is the experimental co-ground system specific melting enthalpy per unit mass at $T_{m\infty}$. X_{am} is, finally, determined as:

$$X_{am} = 1 - X_{nc} - X_{mc} \tag{4.2.4}$$

Once ΔH_m, T_m, and X_{nc} are obtained from the previous iterative procedure, it is possible to evaluate the nanocrystals size distribution. The starting point is the definition of the melting enthalpy (ΔH_m^{nc}) of the mass of drug nanocrystals with a radius ranging from R_s to (R_s + dR_s):

$$\mathrm{d}\left(\Delta H_m^{nc}\right) = \Delta H_m \rho_s \mathrm{d}V_{nc} \tag{4.2.5}$$

where dV_{nc} is the volume occupied by nanocrystals with a radius ranging between R_s and (R_s + dR_s). Equation 4.2.5 yields:

$$\begin{aligned} \frac{\mathrm{d}V_{nc}}{\mathrm{d}R_s} &= \frac{\mathrm{d}\left(\Delta H_m^{nc}\right)}{\mathrm{d}R_s}\frac{1}{\Delta H_m \rho_s} = \frac{\mathrm{d}\left(\Delta H_m^{nc}\right)}{\mathrm{d}T_m}\frac{\mathrm{d}T_m}{\mathrm{d}R_s}\frac{1}{\Delta H_m \rho_s} = \\ &= \underbrace{\frac{\mathrm{d}\left(\Delta H_m^{nc}\right)}{\mathrm{d}t}}_{\dot{Q}}\underbrace{\frac{\mathrm{d}t}{\mathrm{d}T_m}}_{1/v}\frac{\mathrm{d}T_m}{\mathrm{d}R_s}\frac{1}{\Delta H_m \rho_s} = \frac{\dot{Q}}{v}\frac{\mathrm{d}T_m}{\mathrm{d}R_s}\frac{1}{\Delta H_m \rho_s} \end{aligned} \tag{4.2.6}$$

where t is time, $\dot{Q}$ is the heat flow recorded by DSC, and v is DSC heating rate. The function dT_m/dR_s may be numerically obtained from $T_m(R_s)$. Consequently, nanocrystals differential volume distribution (f) is given by:

$$f\left(R_s\right) = \frac{\frac{\mathrm{d}V_{nc}}{\mathrm{d}R_s}}{\int_{R_s^{min}}^{R_s^{max}}\left(\frac{\mathrm{d}V_{nc}}{\mathrm{d}R_s}\right)\mathrm{d}R_s} \tag{4.2.7}$$

where R_s^{max} and R_s^{min} represent, respectively, the maximum and the minimum value assumed by drug nanocrystals radius.

Figure 4.2.4, displaying the results of the exposed numerical approach to the aforesaid four co-ground systems on the basis of the values in Table 4.1.1, shows how X_{nc} decreases with grinding time. Although there is no difference between the 0.5 h and 1 h processed powders in terms of X_{nc}, interestingly, the last ones are characterized by smaller dimensions, as witnessed by the left shift of f. Thus, in this case, the difference of mechanical energy provided to the co-ground mixture translates into a further reduction of R_s without significant effect on X_{nc}. Further increases of grinding time determine both X_{nc} and R_s reductions. Moreover, longer grinding times are reflected

in a progressive narrowing of *f* as clearly visible in Figure 4.2.4. It is worth noticing that, for the four considered systems, R_s ranges from about 0.8 nm to 3.5 nm.

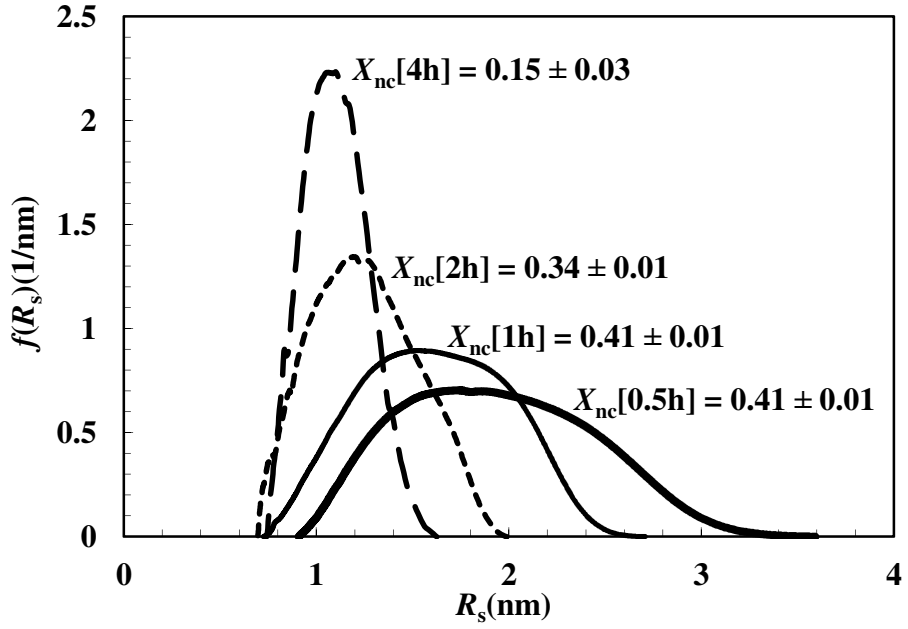

Figure 4.2.4. Nanocrystals fraction (X_{nc}) and differential size distribution (*f*) in the four considered co-ground systems. R_s is nanocrystals radius (from Coceani et al., 2012).

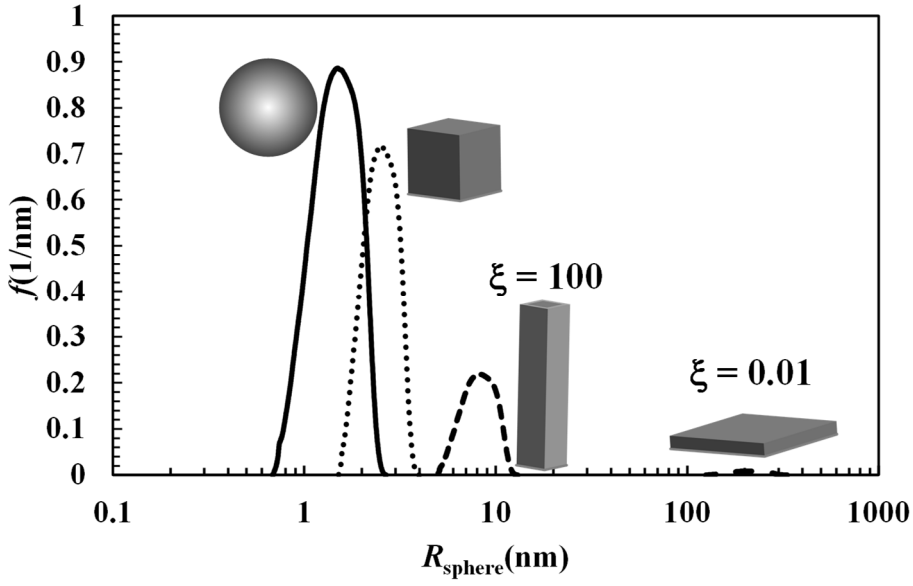

Figure 4.2.5. Effect of nanocrystals geometry (sphere, cube (ξ = β = 1), and parallelepiped (ξ = 0.01 and 100; β = 1)) on their size distribution (*f*) referring to the nimesulide-polyvinylpyrrolidone (1:3) system described in Coceani et al., 2012 after one-hour co-grinding. R_{sphere} is the radius of the equivalent sphere sharing the same volume of parallelepiped-shaped nanocrystals. Nimesulide unit cell half dimension corresponds to R_{sphere} = 0.77 nm.

It is interesting to evaluate how crystal geometry may affect the results depicted in Figure 4.2.4.

Hence, the attention was focused on the one-hour co-ground system by assuming that NIM nanocrystals are square base parallelepipeds ($\beta = 1$) characterized by different shape factors (ξ). For this purpose, it is more significant to express nanocrystals size distribution (f(1/nm)) as a function of the radius, R_{sphere}, of the equivalent sphere sharing the same volume of the considered crystal. The inspection of Figure 4.2.5 reveals that both the distribution wideness and the peak position increase when considering, in order, spherical, cubic, and parallelepiped (rods $\beta = 1$ and $\xi = 100$; platelets $\beta = 1$ and $\xi = 0.01$) nanocrystals. This result sounds reasonable as, in the case of spherical crystals, the size distribution lies very close to the physical limit of NIM nanocrystals, i.e. one-half of NIM unit cell (0.77 nm). On the contrary, when cubic nanocrystals are considered (whose shape is close to that of the real NIM crystals as predicted by the WinXMorph software (Kaminsky, 2007)), the distribution moves towards larger radii. Finally, increasingly larger radii are considered by the rod and platelet distributions. These findings could contribute to explain why, when presuming crystals to be spherical, the estimation of crystals size by DSC is usually lower than that performed by means of the X-Rays approach (Hasa et al., 2013; Hasa et al., 2016).

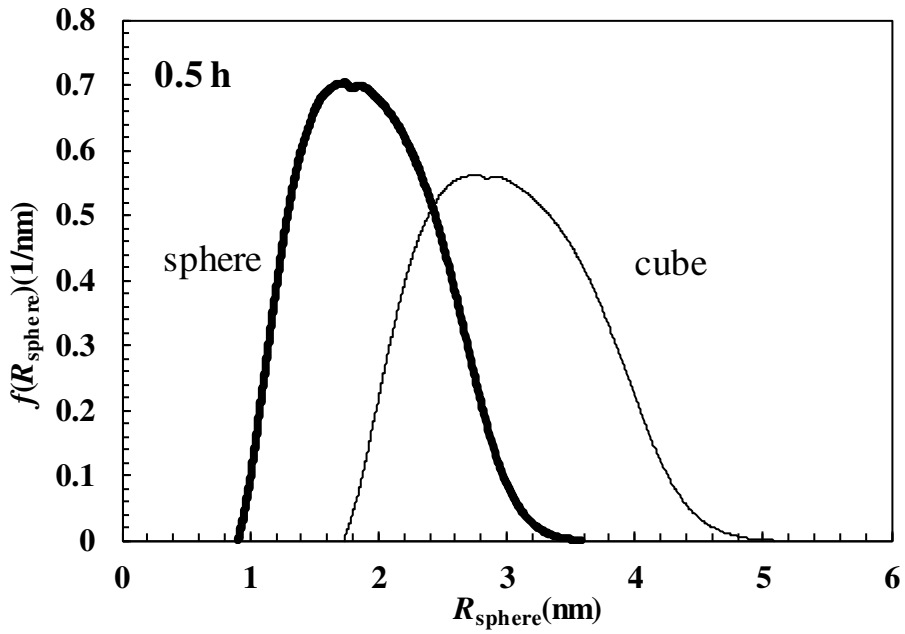

Figure 4.2.6. Size distribution assuming NIM nanocrystals to be spherical (thick line) or cubic ($\xi = \beta = 1$) in the case of the 0.5 h co-ground system. R_{sphere} is the radius of the equivalent sphere sharing the same volume of the considered crystal.

Finally, Figures 4.2.6 – 4.2.9 exhibit the comparison between the nanocrystals size distribution assuming NIM nanocrystals to be spherical (Coceani et al., 2012) or cubic (the result of the present study) for the considered four co-ground systems. It is evident that, no matter how co-grinding time is long, size distribution shifts towards larger radii of the equivalent sphere (R_{sphere}). On the

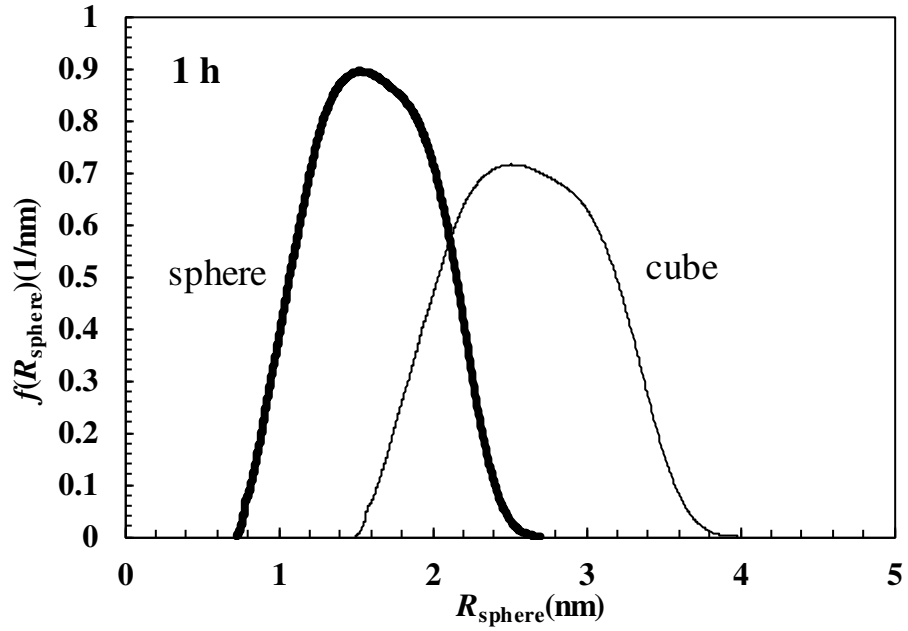

Figure 4.2.7. Size distribution assuming NIM nanocrystals to be spherical (thick line) or cubic ($\xi = \beta = 1$) in the case of the 1 h co-ground system. R_{sphere} is the radius of the equivalent sphere sharing the same volume of the considered crystal.

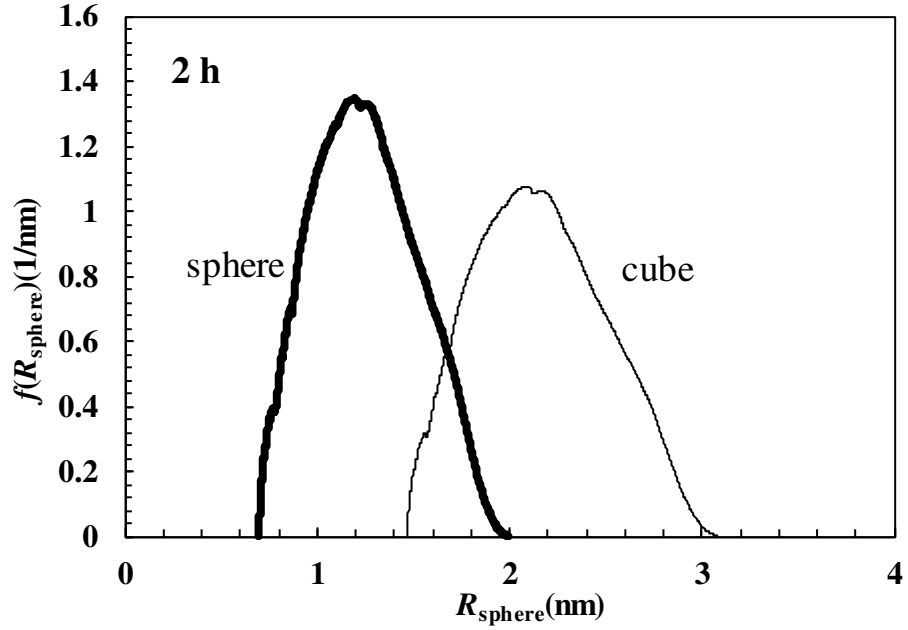

Figure 4.2.8. Size distribution assuming NIM nanocrystals to be spherical (thick line) or cubic ($\xi = \beta = 1$) in the case of the 2 h co-ground system. R_{sphere} is the radius of the equivalent sphere sharing the same volume of the considered crystal.

contrary, crystal shape plays a minor role in the determination of X_{nc}. Indeed, regardless of co-grinding time, X_{nc} coincides with the values displayed in Figure 4.2.4 when cubic, rod-like, or

platelet-like nanocrystals are considered.

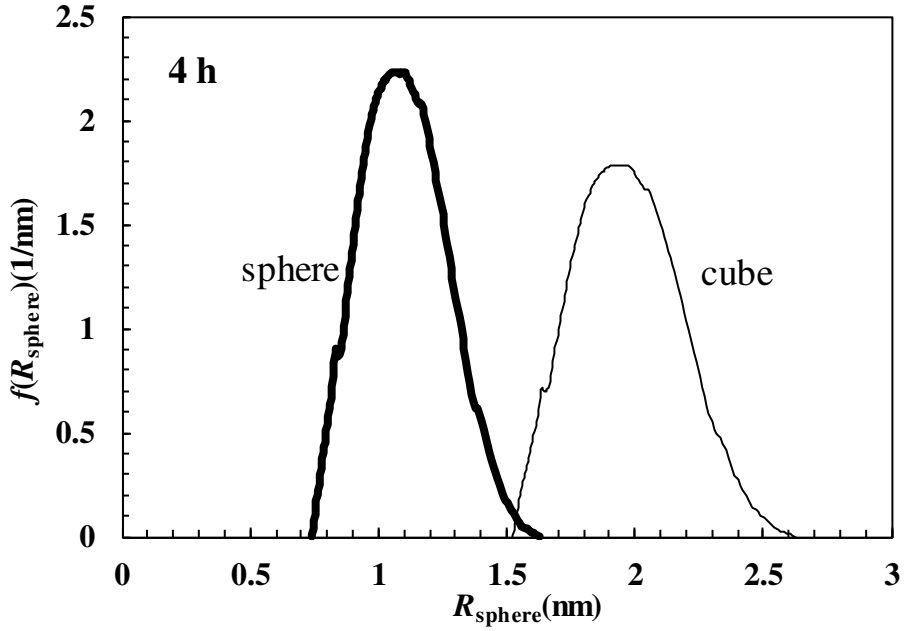

Figure 4.2.9. Size distribution assuming NIM nanocrystals to be spherical (thick line) or cubic ($\xi = \beta = 1$) in the case of the 4 h co-ground system. R_{sphere} is the radius of the equivalent sphere sharing the same volume of the considered crystal.

When moving to the effect of geometry on nanocrystals water solubility, it is useful to recall the relation existing between solubility and T_m or ΔH_m (eqs 2.3.11 and 2.3.12). This thermodynamic approach leads to the interesting conclusion that the solute solubility in the liquid phase also depends on the T_m and ΔH_m of the solid phase. In particular, the lower T_m and ΔH_m the higher the solubility of the solid phase in the liquid one, as shown by Figure 4.2.10 that depicts eqs 2.3.11 and 2.3.12 outcomes regarding the solubility trend of spherical and cubic NIM nanocrystals ($X_{nc} = 1$) as a function of nanocrystals size up to NIM unit cell volume (2.77 nm^3), a value corresponding to R_{sphere} = 0.87 nm. Figure 4.2.10, based, for the sake of simplicity, on the assumption that γ_d is almost constant with concentration, allows evaluating the ratio $C_s/C_{s\infty}$, where $C_{s\infty}$ is the mass/volume solubility of the infinitely large NIM crystal. The choice of the cubic shape is dictated by the approximately cubic morphology of the real NIM nanocrystals as predicted by the WinXMorph software (Kaminsky, 2007). It is clear that cubic shape implies a more pronounced increase of solubility since cubic crystals are characterized by lower T_m and ΔH_m with respect to spherical crystals of the same volume (see Figure 4.1.5). Interestingly, the maximum theoretical solubility increase occurring for $R_{sphere} \rightarrow 0.87$ nm (approximately eightfold) is compatible with the solubility increase of amorphous drugs (not chemically too dissimilar to NIM) lying in the range 10 – 100 (amorphous drug is expected to be more soluble than nanocrystalline

drug) (Murdande et al., 2010; Bahl and Bogner, 2006).

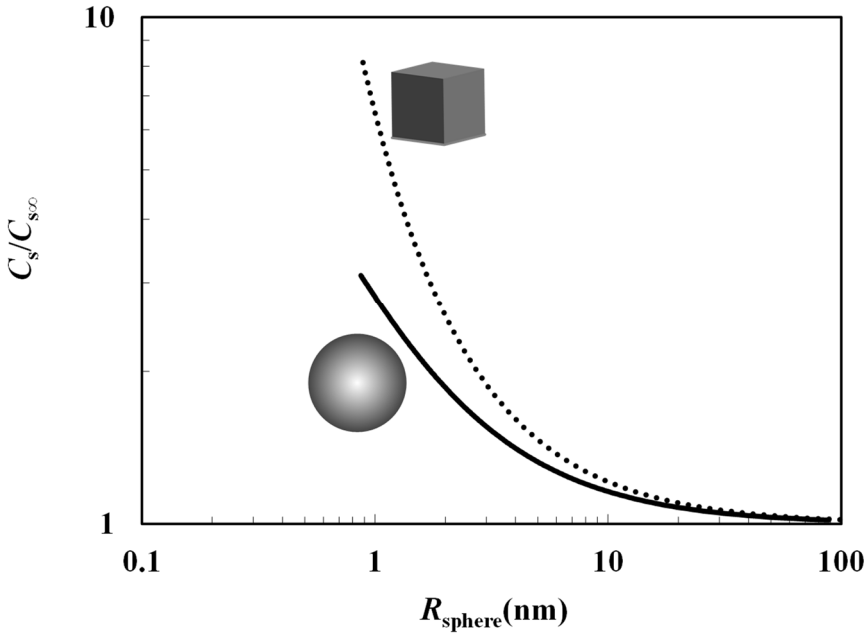

Figure 4.2.10. Effect of nanocrystals geometry (sphere, cube ($\xi = \beta = 1$) on the ratio between the solubility of nimesulide nanocrystals (C_s) and that of the infinitely large nimesulide crystal ($C_{s\infty}$), when assuming the nanocrystals mass fraction $X_{nc} = 1$. R_{sphere} is the radius of a sphere sharing the same volume of the cubic nanocrystal. The simulation is arrested at the value corresponding to nimesulide unit cell volume (2.77 nm^3), i.e. $R_{sphere} = 0.87$ nm.

4.3 Conclusions

The thermodynamic model developed in this work allows evaluating the effect of size and shape on T_m and ΔH_m of organic (drug) nanocrystals. In particular, the differences existing among spherical, cylindrical, and parallelepiped-shaped nanocrystals, characterized by different shape ratios (from needles to platelets), are explained in terms of the ratio between the number of the surface and bulk molecules. Indeed, the higher this ratio the higher the T_m and ΔH_m reductions are and, consequently, the higher the drug solubility is. As a drug solubility increase is reflected in a drug bioavailability enhancement, the considerable practical effect of nanocrystals geometry on nanocrystals based delivery systems clearly emerges.

Model reliability, tested in the case of a well-known poorly water-soluble drug (nimesulide, a non-steroidal anti-inflammatory drug), is supported by the fact that the predicted solubility increase is physically sound in relation to the solubility of the amorphous drug, which is expected to be considerably higher. In addition, model reliability was also proved by the results obtained from a molecular dynamics approach developed in chapter 3, which confirms the T_m and ΔH_m reduction

predicted by the thermodynamic model and the effect of shape ratio variation. Accordingly, this model may be considered a reliable tool for the characterization/design of nanocrystals based delivery systems (determination of X_{nc} and nanocrystals size distribution in polymer-drug systems) and for the evaluation of nanocrystals solubility increase, an aspect of paramount importance for the bioavailability enhancement of poorly water-soluble drugs. In addition, as it relies on thermodynamics, the developed model potentially holds for every drug and its polymorphic forms which may be considerably significant in the pharmaceutical field. Clearly, it requires the knowledge of a certain number of fundamental physical parameters such as surface tension, density, and $T_{m\infty}/\Delta H_{m\infty}$ of the specific drug/polymorphic species. Finally, as it evidences the key role played by nanocrystals geometry, the presented model possible development may imply a shift from the physically sound but rather simple parallelepiped shape to a more complex prismatic one. Indeed, prisms may approximate in a more realistic way the actual nanocrystals shape.

CHAPTER 5

RELEASE AND ABSORPTION

5.1. Physiologically-based Pharmacokinetic Model

The mathematical representation of the human body is essentially based on the physiologically-based pharmacokinetic (PBPK) model presented by Di Muria and co-workers (Di Muria et al., 2010). The gastrointestinal (GI) tract is described by a continuous hollow cylinder subdivided into three zones: gastric lumen (GL), small intestine lumen (SIL), and large intestine lumen (LIL) (see Figure 5.1). The physiological and morphological differences (for instance, pH and internal radius) in the GI tract are considered by means of different permeability (P_{GL}, P_{SIL}, and P_{LIL}, respectively), drug solubility (C_{sGL}, C_{sSIL}, and C_{sLIL}, respectively), and internal radius (R^{i}_{GL}, R^{i}_{SIL}, and R^{i}_{LIL}, respectively) for each zone. The GI tract is crossed by the release environment, an aqueous volume (V_r) containing the delivery system (an ensemble of non-eroding polydispersed polymeric particles loaded with drug), which, due to peristalsis, flows downward from GL to SIL and, eventually, to LIL. For modeling purposes, it is assumed that the release environment shape is the one of a hollow cylinder whose external radius coincides with R^{i}_{GL}, R^{i}_{SIL} or R^{i}_{LIL}, while the internal radius (R^{i}) may vary from zero to R^{i}_{GL}, R^{i}_{SIL} or R^{i}_{LIL}. When R^{i} equals zero, the release environment is simply a cylinder of radius R^{i}_{GL}, R^{i}_{SIL} or R^{i}_{LIL} depending on its GI position. When, on the contrary, R^{i} is greater than zero, the release environment assumes the shape of a hollow cylinder. In both cases, the length of the release environment is defined by (see Figure 5.1):

$$L_j = \frac{V_r}{\pi\left(R_j^{i\,2} - R^{i\,2}\right)} \qquad (j = GL, SIL, LIL) \qquad (5.1.1)$$

It is, thus, evident that the choice of R^{i} serves to define the (time/position-dependent) contact area

between the release environment and the GI tract mucosa. Consequently, R^i may be considered a model fitting parameter. When lacking further physiological information, the most obvious $R^i = 0$ condition was considered in this work.

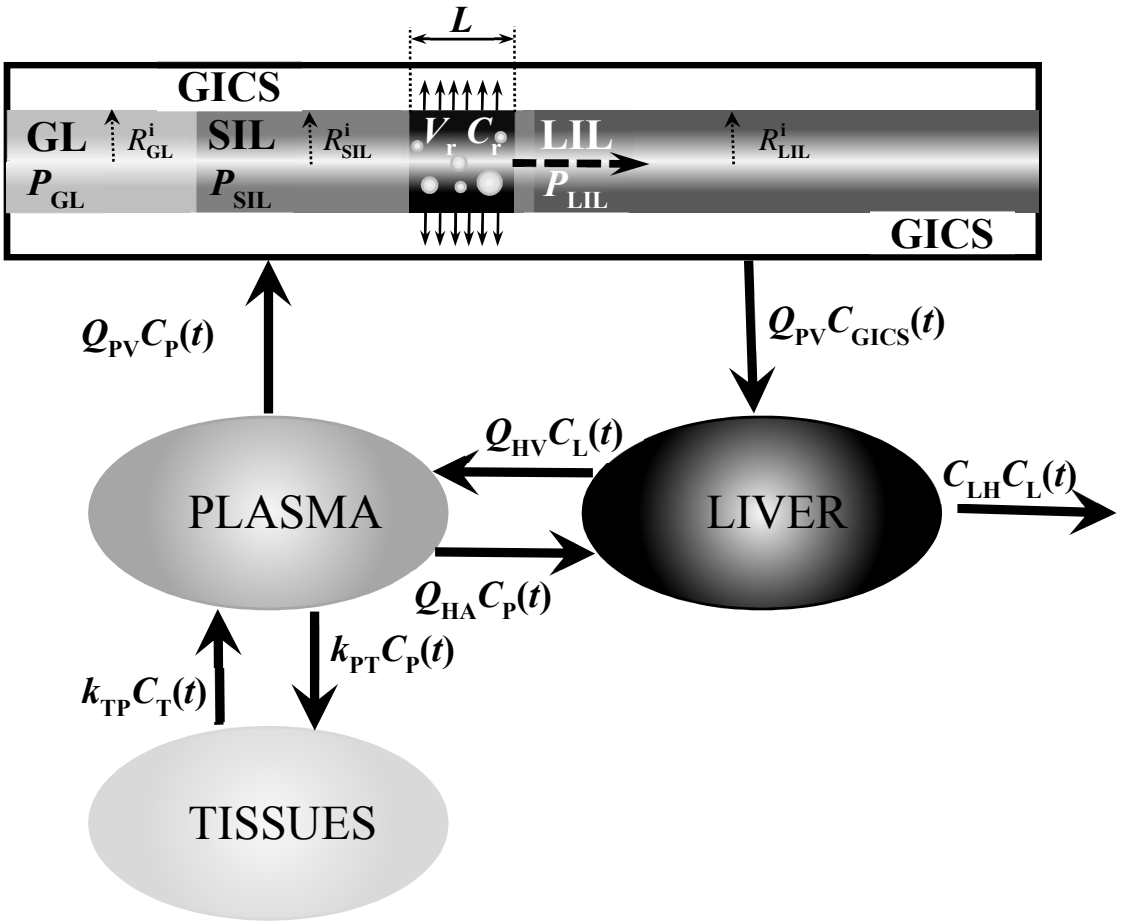

Figure 5.1. Schematic representation of the physiologically-oriented mathematical model. The release environment (volume V_r), due to peristalsis, flows from the gastric lumen (GL) to the small (SIL) and, eventually, large (LIL) intestine. After leaving the delivery system (a non-eroding polydispersed ensemble of polymeric particles), the drug spreads through the release environment fluids and, then, may permeate, by passive absorption, GL, SIL, and LIL mucosae, reaching the gastrointestinal circulatory system (GICS). Afterward, the drug reaches, through the portal vein (PV), the liver where undergoes metabolic/biliary clearance (C_{LH}) or joins the plasma through the hepatic vein (HV). From the plasma, the drug may reach the less perfused tissues, return to the liver through the hepatic artery (HA) or to CIGS through PV. Adapted from Di Muria et al., 2010.

Due to the well-known differences in the morphology/physiology of each zone, it is supposed that the release environment velocity (v_{re}) may vary along the GI tract by setting three different residence times (t_{GL}, t_{SIL}, and t_{LIL}, respectively), one for each zone. The position in the GI tract (P_{os}) and v_{re} are connected by the following relation:

$$P_{os} = \int_0^t v_{re} \mathrm{d}t \tag{5.1.2}$$

where t is time. Thus, by assuming v_{re} as a constant, the transit time (t_t) of the whole GI tract (L_t) is:

$$t_t = \frac{L_t}{v_{re}} \tag{5.1.3}$$

Alternatively, by always assuming v_{re} as a constant, after a certain time t, the position reached by the release environment is:

$$P_{os} = v_{re} t \tag{5.1.4}$$

After being released, the drug may undergo elimination in the release environment (the coefficient of elimination (k_{el}^{RE}) is dimensionally an inverse of time) and cross, due to passive diffusion, the GI mucosa depending on the local permeability, which is a function of the V_r position in the GI tract. Then, the drug reaches the gastrointestinal circulatory system (GICS), a compartment introduced in pharmacokinetic (PK) modeling by Di Muria and co-workers (Di Muria et al., 2010) for the first time. Fundamentally, it corresponds to the ensemble of the mesenteric artery (MA), portal vein (PV), and microcirculatory GI vessels. This section of the whole circulatory system behaves differently from the remaining one. In the case of parenteral administration, MA transports the drug toward the GI tract. In the case of enteral administration, on the contrary, PV transports the drug from the GI tract toward the liver (where the drug undergoes the so-called first-pass effect), from which it reaches the remaining part of the circulatory system (plasma) and the other tissues. The introduction of GICS allowed transforming the very detailed PK model proposed by Jain and co-workers (Jain et al., 1981) (consisting in 21 compartments and 38 ordinary differential equations with approximately 100 parameters) into a simple and effective model (7 compartments and 7 ordinary differential equations with about 20 parameters). GICS is assumed as a well-stirred environment characterized by a constant volume (V_{GICS}) and a time-dependent drug concentration (C_{GICS}).

PV ensures the drug convective transport (blood volumetric flow, Q_{PV}) from GICS to the liver (volume, V_L). The drug concentration in the liver (C_L) varies due to the hepatic clearance (C_{LH}) (dimensionally a volumetric flow) and the convective transport by the hepatic vein (HV) and artery (HA). HV connects the liver to the highly perfused tissues and organs (where the drug concentration is assumed equal to the plasma one) by a blood volumetric flow (Q_{HV}), while HA

returns the drug from the plasma to the liver (blood volumetric flow, Q_{HA}). Once in the plasma (volume, V_P), the drug may be eliminated (the coefficient of elimination (k_{el}^*) is dimensionally a volumetric flow), convectively returned to GICS through PV, and exchanged with the poorly perfused tissues and organs ("tissues" in Figure 5.1). The drug exchange between plasma and tissues (volume, V_T) is ruled by the mass transfer coefficient from plasma to tissues (k_{PT}^*, dimensionally a volumetric flow) and the reverse one from tissues to plasma (k_{TP}^*, dimensionally a volumetric flow). However, the model equations may be rewritten with the more common drug elimination coefficient ($k_{el} = k_{el}^*/V_P$) and plasma-tissues exchange constants ($k_{PT} = k_{PT}^*/V_P$; $k_{TP} = k_{TP}^*/V_P$), which are dimensionally an inverse of time. Accordingly, the PBPK model, depicted in Figure 5.1, is mathematically represented by the following system of ordinary differential equations, where t is the independent variable:

$$\frac{dC_{GICS}}{dt} = \frac{A_j P_j}{V_{GICS}}(C_r - C_{GICS}) + \frac{Q_{PV}}{V_{GICS}}(C_P - C_{GICS}) \qquad \text{GICS} \qquad (5.1.5)$$

$$\frac{dC_L}{dt} = \frac{Q_{PV}}{V_L} C_{GICS} + \frac{Q_{HA}}{V_L} C_P - \left(\frac{Q_{HV} + C_{LH}}{V_L}\right) C_L \qquad \text{LIVER} \qquad (5.1.6)$$

$$\frac{dC_P}{dt} = \frac{Q_{HV}}{V_P} C_L - \left(\frac{Q_{PV} + Q_{HA}}{V_P}\right) C_P - (k_{el} + k_{PT}) C_P + k_{TP} C_T \qquad \text{PLASMA} \qquad (5.1.7)$$

$$\frac{dC_T}{dt} = k_{PT} F C_P - k_{TP} F C_T \qquad \text{TISSUES} \qquad (5.1.8)$$

$$\frac{dM_{el}}{dt} = V_r k_{el}^{re} C_r + C_{LH} C_L + k_{el} V_P C_P \qquad (5.1.9)$$

where $A_j = 2\pi R_j L_j$ (j = GL, SIL, LIL), $P_j = P_{GL}, P_{SIL}, P_{LIL}$, and $F = V_P/V_T$.

Equation 5.1.5 allows the calculation of C_{GICS}, eq 5.1.6 evaluates C_L, eq 5.1.7 determines the plasma drug concentration (C_P), eq 5.1.8 calculates the tissues drug concentration (C_T), and, finally, eq 5.1.9 allows the determination of the amount of the drug eliminated in the release environment, liver, and plasma. The inspection of eq 5.1.5 reveals that the drug diffusive flux from the release environment to GICS requires the knowledge of the drug concentration in the release environment (C_r), which is disclosed in the following.

5.2. Delivery Model

The developed model assumes that the drug release kinetics is essentially determined by (i) the polymeric particles size distribution in the dry state; (ii) the particle swelling after the contact with the release environment fluids (particle erosion is considered negligible for highly cross-linked polymeric networks); (iii) the drug dissolution and diffusion inside the particles; and (iv) the possible drug recrystallization in the release environment fluids.

The first point is described by assuming that the dry particles size distribution is conveniently represented by Weibull's distribution function (Grassi et al., 2006):

$$\frac{V}{V_0} = 1 - \mathrm{e}^{-\left(2\frac{R_\mathrm{p} - R_\mathrm{min}}{\eta}\right)^{\delta}} \tag{5.2.1}$$

where R_p and R_min are, respectively, the generic and the minimum particle radius, η and δ are two parameters regulating Weibull's size distribution, while V_0 and V are the volume occupied by all the polymeric particles and the one occupied by the particles of a radius less than or equal to R_p, respectively. In order to consider particles polydispersity, Weibull's size distribution is subdivided into N_c classes depending on particles radius. Accordingly, the particles of the i^{th} class (i ranging from 1 to N_c) share the same radius R_pi.

For each class, the swelling process (ii) may be evaluated by the following mass balance referred to the swelling agent (solvent):

$$\frac{\partial C_\mathrm{pi}}{\partial t} = \frac{1}{R_\mathrm{i}^2}\frac{\partial}{\partial R_\mathrm{i}}\left(-R_\mathrm{i}^2 J_\mathrm{i}\right) \tag{5.2.2}$$

$$J_\mathrm{i} = J_\mathrm{fi} + J_\mathrm{vi} \tag{5.2.3}$$

$$J_\mathrm{fi} = -D_\mathrm{f}\frac{\partial C_\mathrm{pi}}{\partial R_\mathrm{i}} \tag{5.2.4}$$

$$J_\mathrm{vi} = -D_\mathrm{v}\frac{\partial \sigma_\mathrm{i}}{\partial R_\mathrm{i}} \tag{5.2.5}$$

where C_pi is the local solvent concentration, t is time, R_i is the radial coordinate, J_fi and J_vi indicate the fickian and non-fickian components of the solvent flux, respectively, D_f and D_v are the fickian and viscoelastic (dimensionally a time) diffusion coefficients of the solvent, respectively, while σ_i is the stress tensor generated by the incoming solvent in the film network. Fundamentally, eq 5.2.2

derives from the assumption that the solvent chemical potential depends on both C_{pi} and σ_i. The existence of two contributions in the solvent flux is due to the viscoelasticity of the polymer-solvent system, i.e. polymeric chains undergo rearrangements over time (relaxation) after the solvent uptake. Hence, J_{vi} represents a delayed flux induced by the polymer-solvent system viscoelastic character. Despite the complexity of the theoretical description of the stress and deformation states in the swelling matrix, it is generally assumed that the stress state may be approximated by a scalar viewed as an osmotically induced viscoelastic swelling pressure related to the trace of the stress tensor (Swaminathan and Edwards, 2004). Indeed, one-third of the tensor trace represents the normal stress of the tensor spherical (or hydrostatic) part. On a more physical plane, σ_i may be interpreted as the polymeric network reaction to its enlargement induced by the solvent uptake. Moreover, by following Ferreira and coworkers' suggestions (Ferreira et al., 2014), σ_i may be described by the generalized Maxwell's model, a combination, in series, of one elastic and N_v viscoelastic elements:

$$\sigma_i = \sigma_{0i} + \sum_{j=1}^{N_v} \sigma_{ji} \tag{5.2.6}$$

$$\sigma_{0i} = -E_{0i}\varepsilon_i \tag{5.2.7}$$

$$\frac{d\sigma_{ji}}{dt} + \frac{\sigma_{ji}}{\lambda_{ji}} = -\frac{d\varepsilon_i}{dt} E_{ji} \qquad \text{(j from 1 to } N_v\text{)} \tag{5.2.8}$$

$$E_{ji} = E_{mj}\frac{\rho_s - C_{pi}}{\rho_s - C_m} \qquad \text{(j from 0 to } N_v\text{)} \tag{5.2.9}$$

$$\lambda_{ji} = \lambda_{ej} e^{k\left(1-\frac{C_{pi}}{C_{pe}}\right)} \qquad \text{(j from 1 to } N_v\text{)} \tag{5.2.10}$$

$$\varepsilon_i = \sqrt[3]{\left(\frac{\rho_s - C_{sw}}{\rho_s - C_{pi}}\right)} - 1 \tag{5.2.11}$$

where σ_{0i} and E_{0i} are, respectively, the stress and the elastic modulus of the elastic element, ε_i is the local deformation, ρ_s is solvent density, σ_{ji}, E_{ji}, and λ_{ji} are, respectively, the stress, the elastic modulus, and the relaxation time of the generic viscoelastic element, k is a model parameter, C_{pe} indicates the solvent concentration in the fully swollen particle (thermodynamic equilibrium), while λ_{ej} is the value assumed by λ_{ji} at equilibrium (i.e. when $C_{pi} = C_{pe}$). The "minus" sign

appearing in eqs 5.2.7 and 5.2.8 remembers that stress opposes deformation. The linear dependence of E_{ji} on C_{pi} (eq 5.2.9) is a direct consequence of Flory's theory (Flory, 1953). Indeed, according to Flory, the crosslink density (ρ_x), i.e. the moles, per unit volume, of junctions among the different chains constituting the polymeric network, varies linearly with C_{pi}. Furthermore, by resorting to the same theory, the elastic modulus (Young's modulus) is proportional to ρ_x by $3RT$ (R = gas constant, T = absolute temperature). Thus, in the present work, it is assumed that the E_{ji} dependence on C_{pi} may be described by eq 5.2.9, where C_m is the uniform solvent concentration in the polymeric matrix corresponding to the condition of the (rheological) determination of each E_{mj}. Finally, eq 5.2.11 is derived from the deformation tensor in the simplifying hypothesis of incompressible materials and vanishingly small deformation gradient. In addition, eq 5.2.11 implies that no deformation (and, therefore, stress) occurs when C_{pi} equals the solvent concentration (C_{sw}) corresponding to the crosslinking conditions (if C_{sw} = 0, the expression employed by Ferreira and collaborators (Ferreira et al., 2015) may be derived). A Fujita type dependence for the fickian diffusion coefficient of the solvent was considered (Grassi et al., 2007):

$$D_f = D_f^e e^{-f\left(1-\frac{C_{pi}}{C_{pe}}\right)} \tag{5.2.12}$$

where D_f^e is the equilibrium value of D_f (i.e. when $C_{pi} = C_{pe}$) and f is a model parameter to be determined. Although other possibilities exist (Ferreira et al., 2015), the evaluation of the viscoelastic diffusion coefficient was performed according to Darcy's theory (Truskey et al., 2004), which assimilates a polymeric network to a porous system:

$$D_v = \frac{\alpha^3 r_f^2}{4g\eta_s(1-\alpha)^2} C_{pi} \qquad \left(\alpha = \frac{C_{pi}}{\rho_s}\right) \tag{5.2.13}$$

$$g = \frac{2}{3}\frac{\alpha^3}{1-\alpha}\left[\frac{1}{-2\ln(1-\alpha)-3+4(1-\alpha)-(1-\alpha)^2} + \frac{2}{-\ln(1-\alpha)-\frac{1-(1-\alpha)^2}{1+(1-\alpha)^2}}\right] \tag{5.2.14}$$

where α is system porosity, η_s is the water viscosity at a fixed temperature, and r_f is the radius of the chains (assumed cylindrical) constituting the polymeric network. Fundamentally, Darcy's theory provides a sigmoidal increase (in a bilogarithmic diagram) of D_v with C_{pi} (see Figure 5.2). The swelling part of the model is completed by assuming the solvent-polymer mix ideal, i.e. the particle volume may be computed by summing the polymer, drug, and solvent volumes. In order to consider particles swelling, an isotropic volume increase was introduced (Grassi et al., 2007):

$$dR_i = \frac{dR_i^0}{\sqrt[3]{1 - \frac{C_{pi}}{\rho_s} - \frac{C_i + C_{di}^{am} + C_{di}^{nc} + C_{di}^{mc}}{\rho_d}}} \tag{5.2.15}$$

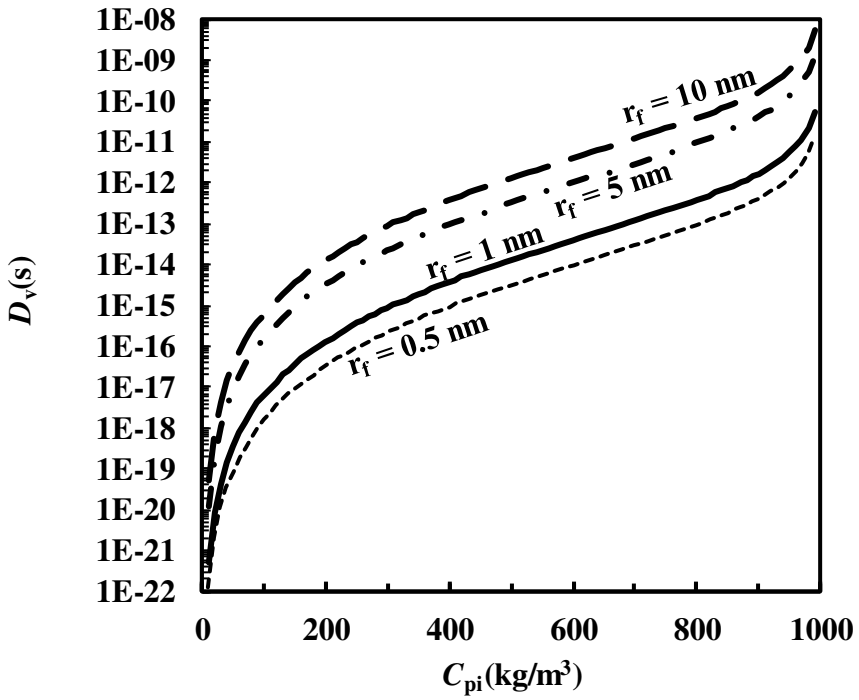

Figure 5.2. Dependence of the viscoelastic diffusion coefficient (D_v) on the local solvent concentration in the matrix (C_{pi}) according to Darcy's law for different polymeric chain radii (r_f). Each simulation assumes water as the swelling fluid ($\eta_s = 10^{-3}$ Pa; $\rho_s = 1000$ kg/m^3).

where dR_i indicates the thickness of the generic spherical shell of a particle, dR_i^0 is the dR_i value in the initial dry state, ρ_d is drug density, C_i is the local concentration of the dissolved drug, C_{di}^{am}, C_{di}^{nc}, and C_{di}^{mc} are, respectively, the position-dependent concentrations of the undissolved drug in the amorphous, nanocrystalline, and microcrystalline states. Equation 5.2.2 may be solved by assuming that particles are initially solvent-free, the solvent flux is null in the particle center for symmetry reasons, and the solvent concentration at the particle surface is obtained by:

$$\lambda_i \left(\frac{dC_{pi}}{dt} \right)_{R=R_{pi}} = C_{pe} - \left(C_{pi} \right)_{R=R_{pi}} \qquad \left[\lambda_i = \frac{\sum_{j=1}^{N_v} \left(\lambda_{ji} E_{ji} \right)_{R=R_{pi}}}{\sum_{j=1}^{N_v} \left(E_{ji} \right)_{R=R_{pi}}} \right] \tag{5.2.16}$$

where λ_i is the polymer-solvent relaxation time at the particle surface.

The drug transport in the polymeric network (iii) is modeled according to the following equation:

$$\frac{\partial C_{\mathrm{i}}}{\partial t}=\frac{1}{R_{\mathrm{i}}^{2}}\frac{\partial}{\partial R_{\mathrm{i}}}\left[\left(D\frac{\partial C_{\mathrm{i}}}{\partial R_{\mathrm{i}}}-v_{\mathrm{i}}C_{\mathrm{i}}\right)R_{\mathrm{i}}^{2}\right]-\left(\frac{\partial C_{\mathrm{di}}^{\mathrm{am}}}{\partial t}+\frac{\partial C_{\mathrm{di}}^{\mathrm{nc}}}{\partial t}+\frac{\partial C_{\mathrm{di}}^{\mathrm{mc}}}{\partial t}\right) \tag{5.2.17}$$

where D is the drug diffusion coefficient in the polymer matrix. Equation 5.2.17 represents the drug mass balance relative to the i$^{\mathrm{th}}$ class of particles, i.e. the class of particles of radius R_{pi}. The first right-hand side term of eq 5.2.17 describes the drug transport due to the existence of a concentration gradient and a convective field (v_{i}) induced by the stress gradient caused by the solvent absorption from the release environment. Indeed, by assuming that the stress gradient acts similarly to a pressure gradient in a pipe, the non-fickian solvent flux may be regarded as the cause of a convective field defined by:

$$J_{\mathrm{vi}}=-D_{\mathrm{v}}\frac{\partial \sigma_{\mathrm{i}}}{\partial R_{\mathrm{i}}}=v_{\mathrm{i}}C_{\mathrm{pi}} \tag{5.2.18}$$

Equation 5.2.17 implies the existence of the dissolved and undissolved drug in the swelling polymeric network. While the undissolved drug is unable to move, the dissolved drug mobility is controlled by its diffusion coefficient, which depends on the local solvent concentration according to Peppas-Reinhart's theory (Peppas and Reinhart, 1983):

$$\frac{D}{D_{\mathrm{ds}}}=\mathrm{e}^{-h\frac{\varphi_{\mathrm{i}}}{1-\varphi_{\mathrm{i}}}}\qquad\left(\varphi_{\mathrm{i}}=1-\frac{C_{\mathrm{pi}}}{\rho_{\mathrm{s}}}\right) \tag{5.2.19}$$

In eq 5.2.19, D_{ds} represents the drug diffusion coefficient in the pure solvent, h is a model parameter to be determined, while φ_{i} is the local polymer volume fraction. Indeed, in polymeric matrices, depending on the adopted drug loading technique, the drug may be found in the amorphous, nanocrystalline, and microcrystalline states (Grassi et al., 2006). As nanocrystals and the amorphous drug are characterized by a higher solubility than microcrystals (Coceani et al., 2012), their presence is able to have a significant effect on drug bioavailability. Whatever the state is, the drug dissolution rate is assumed to be proportional (being K^{am}, K^{nc}, and K^{mc} the proportionality constants for the amorphous, nanocrystalline, and microcrystalline drugs, respectively) to the difference between C_{i} and the drug solubility ($C_{\mathrm{s}}^{\mathrm{am}}$, $C_{\mathrm{s}}^{\mathrm{nc}}$, and $C_{\mathrm{s}}^{\mathrm{mc}}$, respectively, for the amorphous, nanocrystalline, and microcrystalline drugs):

$$\frac{\partial C_{\mathrm{di}}^{\mathrm{am}}}{\partial t}=\begin{cases}-K^{\mathrm{am}}\left(1-\dfrac{C_{\mathrm{i}}}{C_{\mathrm{s}}^{\mathrm{am}}}\right)C_{\mathrm{pi}} & \text{if } C_{\mathrm{di}}^{\mathrm{am}}>0\\ 0 & \text{if } C_{\mathrm{di}}^{\mathrm{am}}=0\end{cases} \tag{5.2.20}$$

$$\frac{\partial C_{\mathrm{di}}^{\mathrm{nc}}}{\partial t}=\begin{cases}-K^{\mathrm{nc}}\left(1-\dfrac{C_{\mathrm{i}}}{C_{\mathrm{s}}^{\mathrm{nc}}}\right)C_{\mathrm{pi}} & \text{if } C_{\mathrm{di}}^{\mathrm{nc}}>0\\ 0 & \text{if } C_{\mathrm{di}}^{\mathrm{nc}}=0\end{cases} \tag{5.2.21}$$

$$\frac{\partial C_{\mathrm{di}}^{\mathrm{mc}}}{\partial t}=\begin{cases}-K^{\mathrm{mc}}\left(1-\dfrac{C_{\mathrm{i}}}{C_{\mathrm{s}}^{\mathrm{mc}}}\right)C_{\mathrm{pi}} & \text{if } C_{\mathrm{di}}^{\mathrm{mc}}>0\\ 0 & \text{if } C_{\mathrm{di}}^{\mathrm{mc}}=0\end{cases} \tag{5.2.22}$$

As the amorphous drug is often unstable and, when dissolving, generally transforms itself into the more thermodynamically stable microcrystalline condition (iv), its solubility reduces with time according to Nogami's theory (Nogami et al., 1969):

$$C_{\mathrm{s}}^{\mathrm{am}}=\left(C_{\mathrm{s0}}^{\mathrm{am}}-C_{\mathrm{s}}^{\mathrm{mc}}\right)\mathrm{e}^{-K_{\mathrm{r}}t}+C_{\mathrm{s}}^{\mathrm{mc}} \tag{5.2.23}$$

where K_{r} is the recrystallization constant and $C_{\mathrm{s0}}^{\mathrm{am}}$ is the amorphous drug solubility. Obviously, the drug recrystallization may also occur in the release environment:

$$\frac{\mathrm{d}M_{\mathrm{c}}}{\mathrm{d}t}=V_{\mathrm{r}}\,K_{\mathrm{rb}}\left(C_{\mathrm{r}}-C_{\mathrm{sc}}^{\mathrm{mc}}\right) \tag{5.2.24}$$

where M_{c}, K_{rb}, and $C_{\mathrm{sc}}^{\mathrm{mc}}$ are, in the release environment, the amount of recrystallized drug up to time t, recrystallization constant, and microcrystalline drug solubility, respectively.

The solution of eq 5.2.17 is performed by assuming that, initially in the particles, no dissolved drug exists (it is possible to find only the solid or amorphous drug in the polymeric network) and the solid and/or amorphous drug concentrations are uniform. Finally, for symmetry reasons, the drug flux in the particle center is set to zero and the usual drug partition condition at the particle-solvent interface is considered. In order to face the issue of the balance between the number of problem unknowns (C_{GICS}, C_{L}, C_{P}, C_{T}, C_{pi}, C_{i}, C_{r}) and that of equations, it is necessary to write a further equation for the definition of C_{r}. In particular, the drug overall mass balance is adopted:

$$\begin{aligned}M_0=&V_{\mathrm{r}}\,C_{\mathrm{r}}+\sum_{\mathrm{i}=1}^{N_{\mathrm{c}}}N_{\mathrm{pi}}\int_0^{R_{\mathrm{pi}}}\left[C_{\mathrm{i}}\left(R_{\mathrm{i}}\right)+C_{\mathrm{di}}^{\mathrm{am}}\left(R_{\mathrm{i}}\right)+C_{\mathrm{di}}^{\mathrm{nc}}\left(R_{\mathrm{i}}\right)+C_{\mathrm{di}}^{\mathrm{mc}}\left(R_{\mathrm{i}}\right)\right]4\pi R_{\mathrm{i}}^2\mathrm{d}R_{\mathrm{i}}+\\&+V_{\mathrm{GICS}}C_{\mathrm{GICS}}+V_{\mathrm{L}}C_{\mathrm{L}}+V_{\mathrm{P}}C_{\mathrm{P}}+V_{\mathrm{T}}C_{\mathrm{T}}+M_{\mathrm{c}}+M_{\mathrm{el}}\end{aligned} \tag{5.2.25}$$

where M_0 is the administered drug dose, N_{pi} is the number of particles belonging to the i^{th} class (N_{pi} may be evaluated by eq 5.2.1). Equation 5.2.25 states that, anytime, the drug amount in the release environment, particles (the sum of integrals), GICS, liver, plasma, and tissues plus M_{c} and

M_{el} must be equal to M_0. Interestingly, the use of eq 5.2.25 is allowed only if the other kinetic equations (5.1.5 – 5.1.9) are expressions of the drug mass balance in the different body compartments (GICS, liver, plasma, and tissues).

Due to the simultaneous presence of ordinary and partial differential equations, the solution of the model required a numerical algorithm running on computers as a FORTRAN program. In particular, the ordinary differential equations were converted into linear algebraic equations according to the implicit Euler's method (Chapra and Canale, 1998), while the implicit control volumes strategy (Patankar, 1986) (20 particles classes, 20 radial subdivisions) was considered for the partial differential equations conversion into linear and non-linear algebraic equations. In order to ensure the numerical solution accuracy, the integration time step was set to 1 s. Gauss-Seidel's approach was employed for the iterative solution of the algebraic equations system, while the relaxation method was utilized to accelerate the solution convergence (Chapra and Canale, 1998).

5.3. Results

One of the critical factors connected with the use of PBPK models is the availability of reliable values for model parameters. Naturally, this is an important issue (Poulin et al., 2011a; Jones et al., 2011; Ring et al., 2011; Vuppugalla et al., 2011; Poulin et al., 2011b) because different values for the same parameter may be found in the literature, in some cases, due to the considerable variability of the subjects involved in tests (Podczeck, 2010; Newton, 2010; Yuen, 2010; Wilson, 2010; Varum et al., 2010; Bowles et al., 2010; Pinto, 2010). Accordingly, in order to simplify the comparison of the three drugs considered in this study (theophylline, temazepam, and nimesulide), it was decided to rely exclusively on only one source (Di Muria et al., 2010) for parameters values. The first active principle, theophylline (THE), also known as 1,3-dimethylxanthine, is a methylxanthine drug with a wide clinical use in the treatment of respiratory diseases such as asthma. Its physicochemical and PK characteristics are displayed in Table 5.3.1. Figure 5.3.1 shows the results of the model simulations for an orally administered THE dose of 100 mg dispersed in a 1 cm^3 polymeric carrier. In particular, the continuous thick solid line refers to the THE concentration in the plasma in the case of a spherical matrix of 6200 μm radius. The initial part of the curve, characterized by zero drug concentration, is related to the drug residence in the stomach, where permeability was set to zero. Then, C_P slowly increases to a maximum and remains steady. The C_P increasing trend corresponds to the drug absorption in SIL and LIL, a result of the simultaneous action of the drug release from the matrix and the following absorption, distribution, metabolism, and elimination (ADME) phenomena. The main reason for low C_P values is the very

Table 5.3.1. Model parameters for microcrystalline theophylline.

PK parameters (Di Muria et al., 2010)			
V_P(ml)	V_L(ml)	V_{GICS}(ml)	V_T(ml)
11000	1500	9.96	24000
Q_{PV}(ml/s)	Q_{HA}(ml/s)	Q_{HV}(ml/s)	C_{LH}(ml/s)
16.25	5.41	21.6	0.4333
k_{el}^{re} (s^{-1})	k_{el}(s^{-1})	k_{TP}(s^{-1})	k_{TP}(s^{-1})
0.0	$2.8 \cdot 10^{-6}$	10^{-6}	10^{-6}
t_{GL}(s)	R_{GL}(cm)	R_{GL}^{i}(cm)	P_{GL}(cm/s)
2880	7.5	0.0	0.0
t_{SIL}(s)	R_{SIL}(cm)	R_{SIL}^{i}(cm)	P_{SIL}(cm/s)
11520	2.5	0.0	$7.0 \cdot 10^{-4}$
t_{LIL}(s)	R_{LIL}(cm)	R_{LIL}^{i} (cm)	P_{LIL}(cm/s)
115200	2.5	0.0	$3.5 \cdot 10^{-4}$
Delivery parameters (Grassi et al., 2000)			
C_{pe}(g/ml)	D_f^e (cm^2/s)	D_{ds}(cm^2/s)	C_s^{mc}(g/ml)
0.31	10^{-7}	$8.2 \cdot 10^{-6}$	12.495
ρ_d(g/ml)	K^{mc}(s^{-1})	K_r(s^{-1})	K_{rb}(s^{-1})
1.47	1.0	0.0	0.0
λ_{e1}(s)	λ_{e2}(s)	λ_{e3}(s)	λ_{e4}(s)
$4.7 \cdot 10^{-2}$	$4.7 \cdot 10^{-1}$	4.7	47
E_0(Pa)	E_1(Pa)	E_2(Pa)	E_3(Pa)
32972	85438	54674	43378
E_4(Pa)	r_f(nm)	V_r(ml)	K_p(-)
76791	1.0	250	1

slow drug delivery kinetics (the low ratio between the release surface and the matrix volume, typical of large spheres) from the matrix as depicted in Figure 5.3.2 (see the continuous thick solid line). By keeping constant the delivery system volume (1 cm^3), its splitting into equal smaller particles leads to a much faster C_P increase. In particular, the thin solid line and the dashed line of Figure 5.3.1 represent, respectively, the C_P trend referred to particles characterized by a radius equal to 620 μm (about 10^3 particles) and 62 μm (about 10^6 particles). It may be observed that the drug concentration rise is fast and, after 2.5 h, C_P reaches about 5 μg/ml in the first case (620 μm) and about 6.5 μg/ml in the second one (62 μm). Further reductions of particles size leaves the C_P trend unaffected. Indeed, as Figure 5.3.2 demonstrates, when the particles radius is around 62 μm, the drug totally and very rapidly dissolves in the release environment (the stomach fluids), thus reaching the maximum value compatible with the administered dose, i.e. 400 μg/ml. In this case, no control over the drug release is exerted and the delivery system ensures a prompt and total

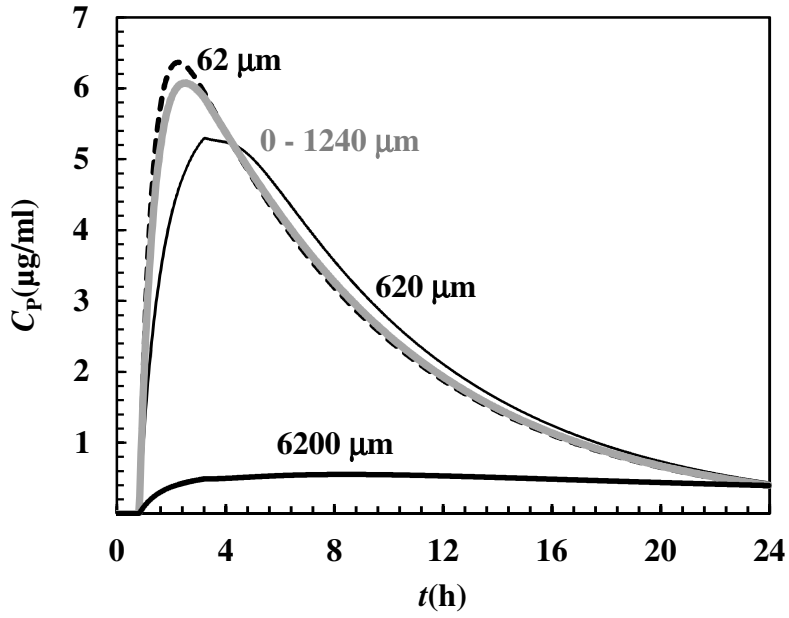

Figure 5.3.1. Theophylline plasma concentration (C_P) for different spherical delivery systems of the same volume (1 cm^3) and dose (100 mg). The number near each curve indicates the diameter of the considered sphere(s), while the gray line refers to a polydispersed ensemble of spherical particles whose diameter ranges from 0 to 1240 μm. In the 6200 μm case, the numerical solution subdivides the particle into 500 control volumes, while the 620 μm ones into 200 and those of 62 μm into 20. In the polydispersed case, the particles distribution was subdivided into 20 classes, while the generic particle of each class in 20 control volumes.

release in the stomach. In other words, no difference is observed in the C_P trend induced by this formulation or a drug solution of the same dose. Moreover, the C_P trend shown by the 62 μm particles may be approximately obtained by the ensemble of polydispersed particles described by eq 5.2.1 with the following parameters: η = 700 μm, δ = 2, R_{min} = 0 μm, and R_{max} = 1200 μm (see the gray line in Figure 5.3.1). The difference, when using a polydispersed distribution, is a lower drug concentration (see the gray line in Figure 5.3.2) in the stomach fluids, which is advantageous in the case of stomach wall aggressive drugs. Finally, it is worthwhile underlining that, depending on the PK parameters displayed in Table 5.3.1, the time evolutions of C_{GICS} and C_L are substantially equal to the C_P one. The rationale are the small CIGS (V_{GICS} = 10 ml) and liver (V_L = 1500 ml) volumes in comparison to the plasma (V_P = 11000 ml) and tissues (V_T = 24000 ml) ones, including the relatively high volumetric flow among the various compartments (Q_{HV}, Q_{PV}, and Q_{HA}; see Figure 5.1 and Table 5.3.1). On the contrary, C_T, in the scarcely perfused tissues and organs ("tissues" in Figure 5.1), monotonically increases, thus reaching, for all formulations, values which are about two orders of magnitude smaller than C_P (see Figure 5.3.3). This is

essentially due to the higher value of the tissues volume (V_T = 24000 ml). Interestingly, for the smaller particles, C_P falls into the THE therapeutic window corresponding to 5 – 15 μg/ml.

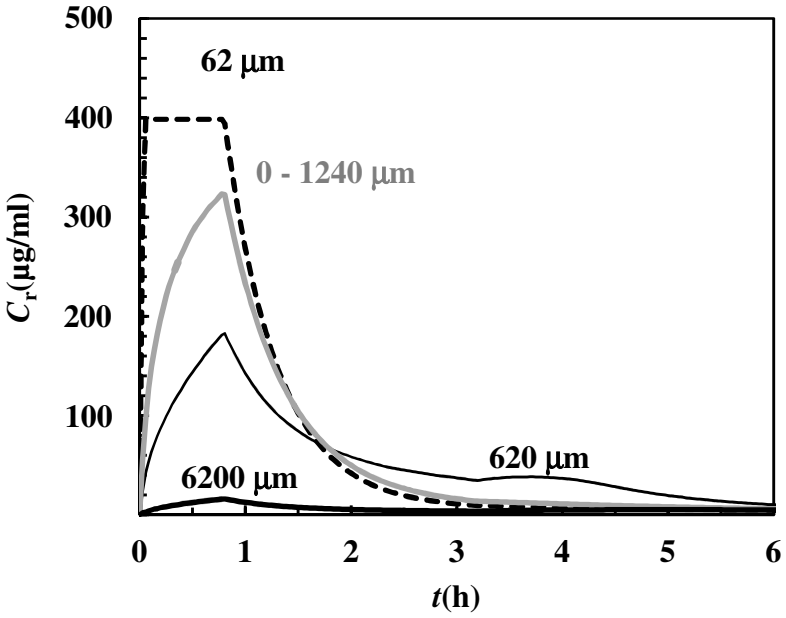

Figure 5.3.2. Theophylline concentration in the release environment (C_r) for different spherical delivery systems of the same volume (1 cm^3) and dose (100 mg). The number near each curve indicates the diameter of the considered sphere(s), while the gray line refers to a polydispersed ensemble of spherical particles whose diameter ranges from 0 to 1240 μm. In the 6200 μm case, the numerical solution subdivides the particle into 500 control volumes, while the 620 μm ones into 200 and those of 62 μm into 20. In the polydispersed case, the particles distribution was subdivided into 20 classes, while the generic particle of each class in 20 control volumes.

The second drug, temazepam (TEM), a benzodiazepine derivative characterized by sedative and hypnotic actions, was selected being possible to load it into a polymeric carrier (such as cross-linked polyvinylpyrrolidone particles) in a completely amorphous form (Grassi et al., 2000). Indeed, this aspect is highly advantageous as amorphous TEM is characterized by a much higher solubility (around 8649 μg/ml) with respect to the microcrystalline drug solubility (about 164 μg/ml). In absence of certain values for TEM PK parameters, those of a similar drug (Di Muria et al., 2010) were adopted, while all other model parameters were set according to a previous study (Grassi et al., 2000) (see Table 5.3.2). The concentration trends were simulated by considering an ensemble of polydispersed particles described by eq 5.2.1 with the following parameters: η = 5.96 μm, δ = 3.88, R_{min} = 0.3 μm, and R_{max} = 7 μm. Figure 5.3.4 clarifies that amorphous TEM (gray line) produces, in PK terms, a better performance with respect to crystalline TEM (black line). Indeed, amorphous TEM not only yields a slightly higher C_P maximum but also the C_P peak occurs more than 10 minutes before the one of its crystalline form. This simulation was performed by

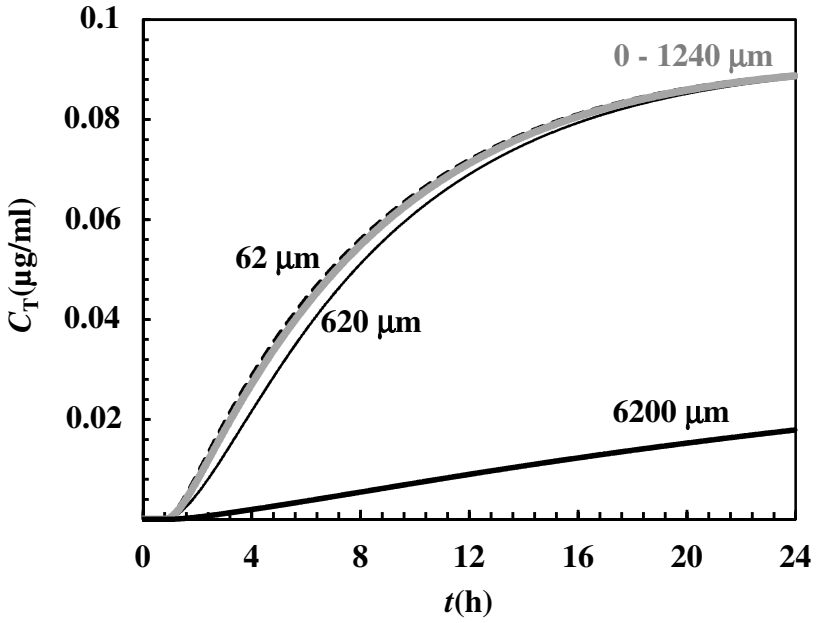

Figure 5.3.3. Theophylline concentration in tissues (C_T) for different spherical delivery systems of the same volume (1 cm^3) and dose (100 mg). The number near each curve indicates the diameter of the considered sphere(s), while the gray line refers to a polydispersed ensemble of spherical particles whose diameter ranges from 0 to 1240 µm. In the 6200 µm case, the numerical solution subdivides the particle into 500 control volumes, while the 620 µm ones into 200 and those of 62 µm into 20. In the polydispersed case, the particles distribution was subdivided into 20 classes, while the generic particle of each class in 20 control volumes.

assuming that no amorphous TEM recrystallization occurs in the stomach, although there is evidence of the contrary in water (Grassi et al., 2000). Indeed, as the recrystallization kinetics may strongly depend on the physicochemical properties of the dissolving fluids (the stomach fluids significantly differ from water), the lack of certain information about the TEM recrystallization in the stomach fluids pushes to neglect recrystallization this time. By doing this, the maximum possible effect of amorphous TEM in respect of crystalline TEM was estimated. Figure 5.3.5 shows that, in the amorphous case, C_r rapidly reaches the maximum value (224 µg/ml) compatible with the administered dose (100 mg). This phenomenon, obviously, occurs in GL ($t < 0.8$ h), while, once in SIL and eventually LIL, C_r decreases to zero. In the crystalline case, on the contrary, the C_r increase is smaller and the maximum value is well below that reached in the amorphous case. At the same time, the C_r reduction in SIL and LIL is slower, thus ensuring higher C_P from approximately 2 hours onward. Finally, C_T, in the scarcely perfused tissues and organs ("tissues" in Figure 5.1), monotonically increases, thus reaching, for all formulations, values which are of the same order of magnitude of C_P (see Figure 5.3.6). This is essentially due to the higher tissues

volume (V_T = 152000 ml).

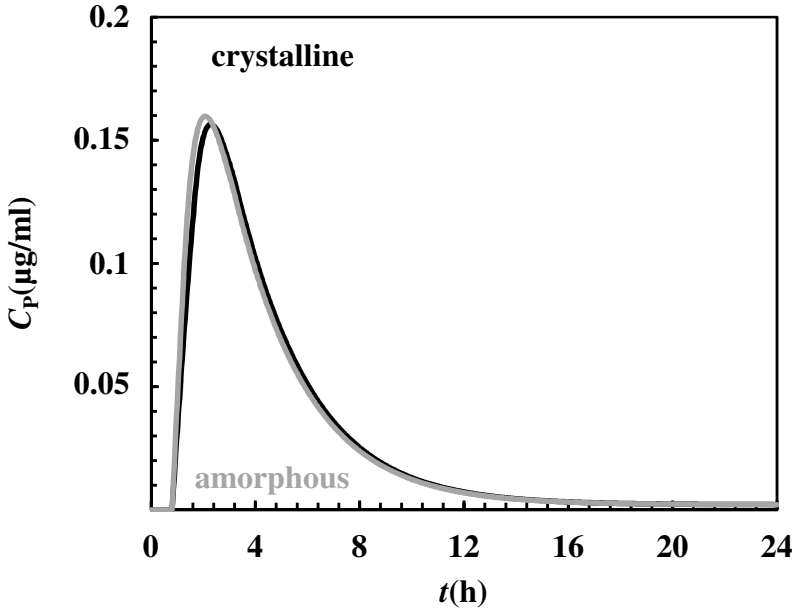

Figure 5.3.4. Amorphous (gray line) and crystalline (black line) temazepam concentrations in the plasma (C_P) for a polydispersed ensemble of spherical particles with a diameter ranging from 0.3 to 7 µm, a global volume of 1 cm^3, and a drug dose of 100 mg. The particles distribution was subdivided into 20 classes, while the generic particle of each class in 20 control volumes.

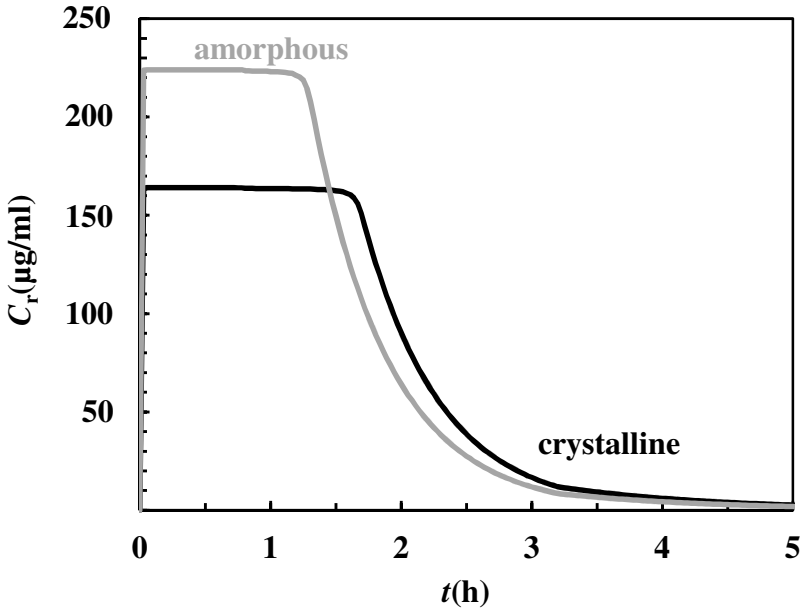

Figure 5.3.5. Amorphous (gray line) and crystalline (black line) temazepam concentrations in the release environment (C_r) for a polydispersed ensemble of spherical particles with a diameter ranging from 0.3 to 7 µm, a global volume of 1 cm^3, and a drug dose of 100 mg. The particles distribution was subdivided into 20 classes, while the generic particle of each class in 20 control volumes.

Table 5.3.2. Model parameters for temazepam.

PK parameters (Di Muria et al., 2010)			
V_P(ml)	V_L(ml)	V_{GICS}(ml)	V_T(ml)
229000	1500	9.96	152000
Q_{PV}(ml/s)	Q_{HA}(ml/s)	Q_{HV}(ml/s)	C_{LH}(ml/s)
16.25	5.41	21.6	16.46
k_{el}^{re} (s^{-1})	k_{el}(s^{-1})	k_{TP}(s^{-1})	k_{TP}(s^{-1})
0.0	0.0	$6.4 \cdot 10^{-5}$	10^{-6}
t_{GL}(s)	R_{GL}(cm)	R_{GL}^{i}(cm)	P_{GL}(cm/s)
2880	7.5	0.0	0.0
t_{SIL}(s)	R_{SIL}(cm)	R_{SIL}^{i}(cm)	P_{SIL}(cm/s)
11520	2.5	0.0	$6.0 \cdot 10^{-4}$
t_{LIL}(s)	R_{LIL}(cm)	R_{LIL}^{i} (cm)	P_{LIL}(cm/s)
115200	2.5	0.0	$3.0 \cdot 10^{-4}$
Delivery parameters (Grassi et al., 2000)			
C_{pe}(g/ml)	D_f^e (cm^2/s)	D_{ds}(cm^2/s)	ρ_d(g/ml)
0.31	10^{-7}	$7.2 \cdot 10^{-6}$	1.35
C_s^{mc}(g/ml)	C_s^{nc} (g/ml)	C_s^{am}(g/ml)	K^{mc}(s^{-1})
0.164	0.224	8.649	0.1
K^{nc}(s^{-1})	K^{am}(s^{-1})	K_r(s^{-1})	K_{rb}(s^{-1})
0.1	0.1	0.007	0.0
λ_{e1}(s)	λ_{e2}(s)	λ_{e3}(s)	λ_{e4}(s)
$4.7 \cdot 10^{-2}$	$4.7 \cdot 10^{-1}$	4.7	47
E_0(Pa)	E_1(Pa)	E_2(Pa)	E_3(Pa)
32972	85438	54674	43378
E_4(Pa)	r_f(nm)	V_r(ml)	K_p(-)
76791	1.0	250	1

The last drug is nimesulide (NIM), a typical non-steroidal anti-inflammatory largely employed in the clinical practice (Bernareggi, 1998). Similarly to TEM, it is scarcely soluble in aqueous media, but its solubility is pH-dependent as it is a weak acid (p*K*a = 6.46) (Fallavena and Schapoval, 1997). Obviously, NIM solubility may be improved by using its amorphous/nanocrystalline form (Coceani et al., 2012). In addition, the first-pass effect for NIM is negligible (Bernareggi, 1998). While some PK parameters (Di Muria et al., 2010; Grassi et al., 2006; Bernareggi, 1998) and all delivery parameters (Grassi et al., 2000; Coceani et al., 2012) may be gathered from the literature, no reliable estimation of the NIM solubility in the gastric environment and of the permeability through GL, SIL, and LIL mucosae were available. Therefore, the model was fitted (four fitting parameters) to the experimental data referring to the oral administration (three humans) of a commercial prompt action NIM formulation (100 mg). The fitting procedure was performed by assuming that NIM in microcrystalline form is loaded into a polymeric carrier showing the

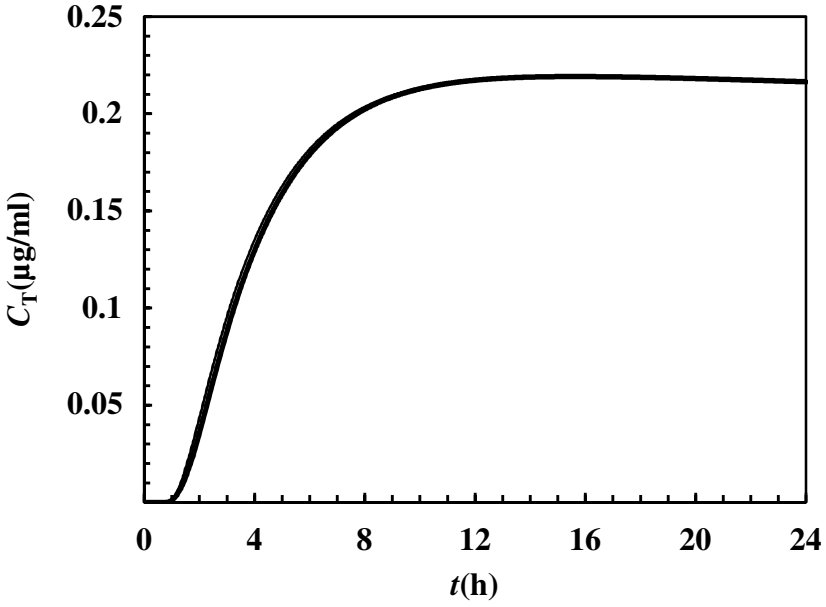

Figure 5.3.6. Amorphous or crystalline temazepam concentration in tissues (C_T) for a polydispersed ensemble of spherical particles with a diameter ranging from 0.3 to 7 μm, a global volume of 1 cm^3, and a drug dose of 100 mg. The particles distribution was subdivided into 20 classes, while the generic particle of each class in 20 control volumes.

physicochemical characteristics displayed in Table 5.3.3, which are similar to those of the polyvinylpyrrolidone particles considered in the TEM case. Furthermore, R_{GL}^{i} was set to 7.3 cm in such a way that the stomach absorption surface equals the one normally present in humans (around 1 m^2) (Grassi et al., 2006). Figure 5.3.7 shows the agreement between the model best fitting (black line) and the experimental data (open circles) after assuming, as fitting parameters, C_s^{mc} = 39 μg/ml, $P_{GL} = 4.9 \cdot 10^{-4}$ cm/s, $P_{SIL} = 1.1 \cdot 10^{-4}$ cm/s, and $P_{LIL} = 6 \cdot 10^{-5}$ cm/s. These permeability values indicate that NIM is rapidly absorbed by the gastric mucosa, while its absorption in SIL and LIL is slower. These results appear reasonable. Indeed, the acid environment of the stomach is particularly favorable for the absorption of NIM because, at lower pH than 3, this drug is completely undissociated. On the contrary, for higher pH such as the SIL one, NIM is partially or totally dissociated, thus preventing the drug from crossing the lipophilic mucous membrane. Accordingly, its physicochemical properties should be responsible for the NIM different permeability through the GI tract rather than the effect of intestinal wall transporters or other phenomena. These physicochemical considerations are supported by studies regarding the local absorption of NIM (Bernareggi and Rainsford, 2005; PPL 322, 1999) conducted on healthy volunteers (gamma scintigraphy). Indeed, these tests proved that the stomach and the proximal

small bowel account for 40% of the NIM absorption. As in the TEM case, the NIM absorption may be improved by employing its amorphous form. Figure 5.3.7 depicts C_P (gray line) in the case of amorphous NIM by assuming, as for TEM, that no recrystallization occurs (K_{rb} = 0). Hence,

Table 5.3.3. Model parameters for nimesulide.

PK parameters (Di Muria et al., 2010; Jain et al., 1981; Grassi et al., 2006; Bowles et al., 2010; Bernareggi, 1998)			
V_P(ml)	V_L(ml)	V_{GICS}(ml)	V_T(ml)
5000	1500	9.96	13000
Q_{PV}(ml/s)	Q_{HA}(ml/s)	Q_{HV}(ml/s)	C_{LH}(ml/s)
16.25	5.41	21.6	0.49
k_{el}^{re} (s^{-1})	k_{el}(s^{-1})	k_{TP}(s^{-1})	k_{TP}(s^{-1})
0.0	0.0	10^{-6}	10^{-6}
t_{GL}(s)	R_{GL}(cm)	R_{GL}^{i}(cm)	P_{GL}(cm/s)
2880	7.5	7.3	$4.9 \cdot 10^{-4}$
t_{SIL}(s)	R_{SIL}(cm)	R_{SIL}^{i}(cm)	P_{SIL}(cm/s)
11520	2.5	0.0	$1.1 \cdot 10^{-4}$
t_{LIL}(s)	R_{LIL}(cm)	R_{LIL}^{i} (cm)	P_{LIL}(cm/s)
115200	2.5	0.0	$0.6 \cdot 10^{-4}$
Delivery parameters (Grassi et al., 2000; Camera-Roda and Sarti, 1990; Coceani et al., 2012)			
C_{pe}(g/ml)	D_f^e (cm^2/s)	D_{ds}(cm^2/s)	ρ_d(g/ml)
0.31	10^{-7}	10^{-6}	1.49
C_s^{mc}(g/ml)	C_s^{nc} (g/ml)	C_s^{am}(g/ml)	K^{mc}(s^{-1})
0.039 (pH < 6.4) 0.1 (pH > 6.4)	0.058 (pH < 6.4) 0.15 (pH > 6.4)	4.108	2.0
K^{nc}(s^{-1})	K^{am}(s^{-1})	K_r(s^{-1})	K_{rb}(s^{-1})
2.0	2.0	0.06	0.0
λ_{e1}(s)	λ_{e2}(s)	λ_{e3}(s)	λ_{e4}(s)
$4.7 \cdot 10^{-2}$	$4.7 \cdot 10^{-1}$	4.7	47
E_0(Pa)	E_1(Pa)	E_2(Pa)	E_3(Pa)
32972	85438	54674	43378
E_4(Pa)	r_f(nm)	V_r(ml)	K_p(-)
76791	1.0	250	1

this prediction should represent the maximum expected effect of amorphous NIM. It is noticeable that the maximum concentration is considerably increased and, up to about 5 hours, the drug concentration is higher than that of the crystalline case. This behavior in the plasma is explained by Figure 5.3.8, where C_r is shown for the amorphous (gray line) and crystalline (black line) drug. In the amorphous case, NIM is rapidly released in the first 3 minutes and its concentration is higher than that corresponding to the crystalline case. This means that its onset of action is considerably

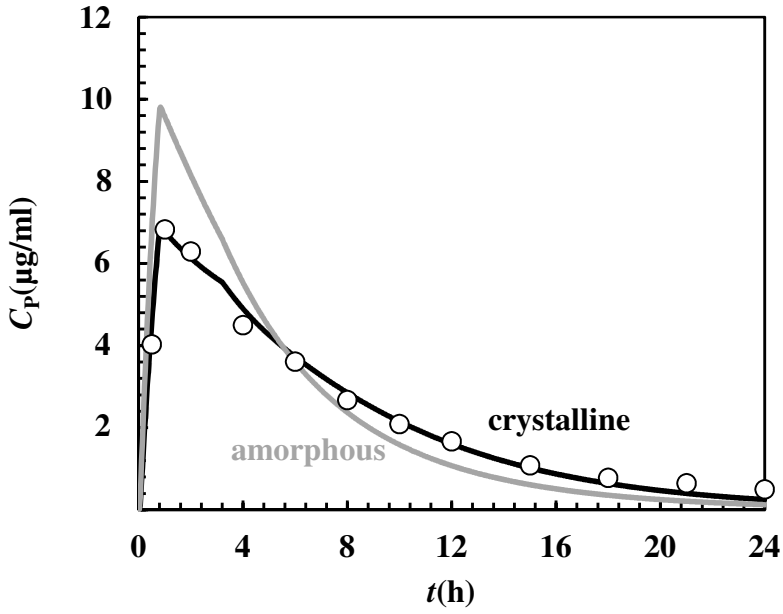

Figure 5.3.7. Amorphous (gray line) and crystalline (black line) nimesulide plasma concentration (C_P) for a polydispersed ensemble of spherical particles with a diameter ranging from 1 to 10 µm, a global volume of 1 cm^3, and a dose of 100 mg. The open circles indicate the experimental data (the average of three subjects) which the model was fitted to (black line). The particles distribution was subdivided into 20 classes, while the generic particle of each class in 20 control volumes.

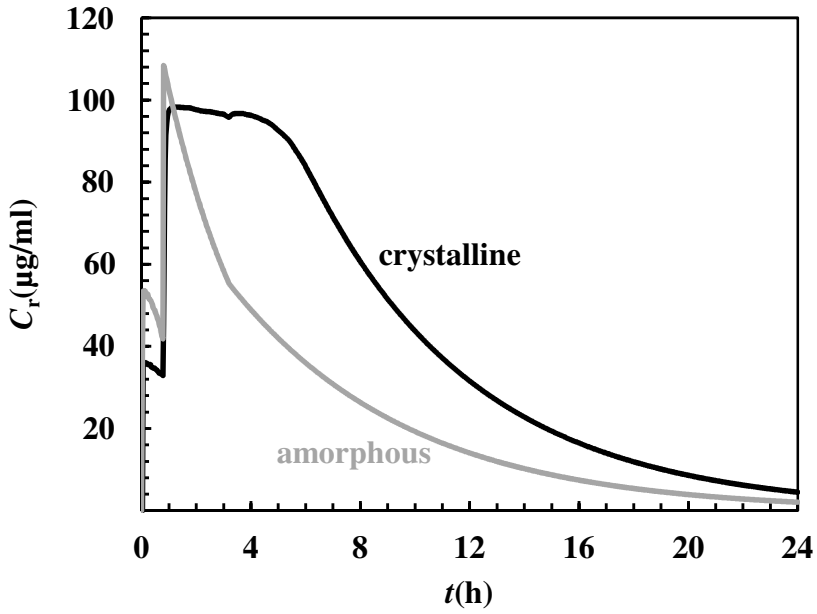

Figure 5.3.8. Amorphous (gray line) and crystalline (black line) nimesulide concentration in the release environment (C_r) for a polydispersed ensemble of spherical particles with a diameter ranging from 1 to 10 µm, a global volume of 1 cm^3, and a dose of 100 mg. The particles distribution was subdivided into 20 classes, while the generic particle of each class in 20 control volumes.

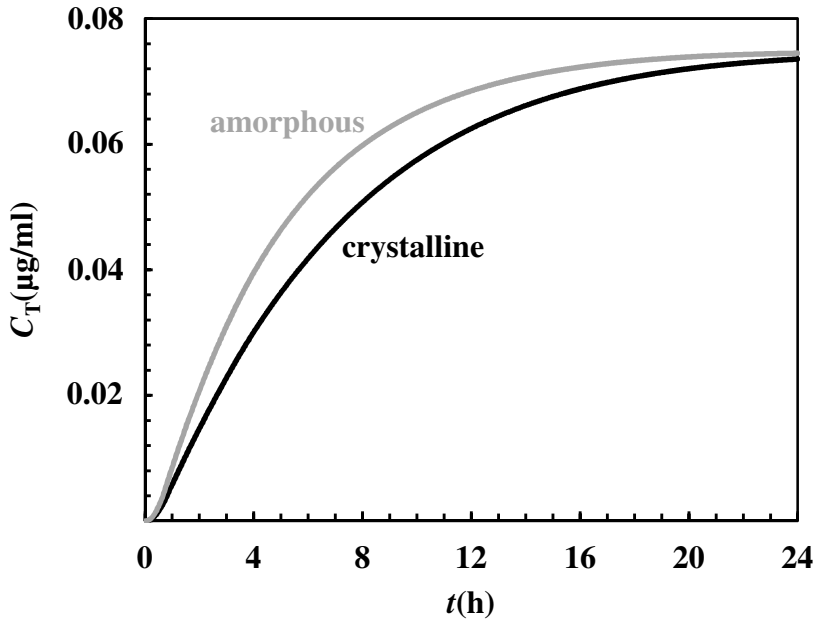

Figure 5.3.9. Amorphous (gray line) and crystalline (black line) nimesulide concentration in tissues (C_T) for a polydispersed ensemble of spherical particles with a diameter ranging from 1 to 10 µm, a global volume of 1 cm^3, and a dose of 100 mg. The particles distribution was subdivided into 20 classes, while the generic particle of each class in 20 control volumes.

increased, a desirable feature for a rapid pain relief. Moreover, in this case, the time evolutions of C_{GICS} and C_L are substantially equal to the C_P one for the same rationale observed in the case of THE. Again, C_T in the scarcely perfused tissues and organs monotonically increases, thus reaching, for all formulations, values that are about two orders of magnitude smaller than C_P. The abrupt increase of C_r occurring after 1 h, in both the crystalline and amorphous cases, is due to the reduced value of P_{LIL}. Indeed, that reduction implies the decrease of the drug flux leaving the release environment which, in turn, causes a drug concentration increase.

5.4. Conclusions

While the problem of a reliable evaluation of the drug concentration in the plasma subsequent to the oral administration remains challenging, a major step toward its solution is represented by mathematical models able to simultaneously take account of the in vivo drug release and the succeeding ADME processes. With this end in view, a sound mathematical model, resulting from merging a physiologically oriented PK model and a delivery one, was developed. Aiming to obtain reliable in vivo simulations, at present, the useful tool developed in this study is able to compare different formulations of the same drug or the same formulation of different drugs. Indeed, this

theoretical approach allows evaluating the effect of different doses, various particles mean sizes or distributions, and different solid forms, i.e. amorphous, nanocrystalline, and microcrystalline. It also demonstrates that the in vivo release kinetics may behave differently from the in vitro one owing to the effect of living tissues. In other words, while the mutual dependence of the drug release and the ADME processes is known, this work represents an attempt to carefully quantify that interplay. In conclusion, the presented model appears to be a rational basis for designing state-of-the-art delivery systems and may constitute an important step toward dependable simulations of the plasma drug concentration subsequent to the oral administration. Finally, it is important to underline that the PK part of the model may be easily improved by adding further compartments or relations among compartments (Chiarappa et al., 2017). For instance, the periodic enteropathic circulation of bile – produced by the hepatocytes, stored in the gallbladder, and delivered to the duodenum by means of Oddi's sphincter, which opens/closes depending on the digestive processes – may be considered if necessary. The reason for this "simplicity" resides in the fact that all these additional features, mathematically speaking, are represented by ordinary differential equations whose integration in the proposed model is straightforward. Indeed, in the light of the implicit Euler's method employed for their resolution, those equations represent nothing but further linear equations.

CHAPTER 6

CONCLUSIONS AND PERSPECTIVES

The thermodynamic model built in the present thesis allows evaluating the effect of size and shape on the melting temperature (T_m) and enthalpy (ΔH_m) of organic (drug) nanocrystals. In particular, the differences existing among spherical, cylindrical, and parallelepiped-shaped nanocrystals, characterized by different shape ratios (from needles to platelets), are explained in terms of the ratio between the number of the surface and bulk molecules. Indeed, the higher this ratio is, the higher the T_m and ΔH_m reductions are and, consequently, the higher the drug solubility is. As a solubility increase is reflected in a drug bioavailability enhancement, the considerable practical effect of nanocrystals geometry on nanocrystals based delivery systems clearly emerges.

Model reliability, tested in the case of well-known poorly water-soluble drugs (nimesulide, griseofulvin, and nifedipine), is supported by the fact that the predicted solubility increase is physically sound in relation to the solubility of the amorphous drugs, which is expected to be considerably higher. In addition, model reliability was also proved by the results obtained from a molecular dynamics approach, which confirms the T_m and ΔH_m reduction predicted by the thermodynamic model and the effect of shape ratio variation. Accordingly, this model may be considered a reliable tool for the characterization/design of nanocrystals based delivery systems (the estimation of X_{nc} and nanocrystals size distribution in polymer-drug systems) and for the evaluation of nanocrystals solubility increase, an aspect of paramount importance for the bioavailability enhancement of poorly water-soluble drugs. Moreover, as it relies on thermodynamics, the developed model potentially holds for every drug and its polymorphic forms which may be significant in the pharmaceutical field. Clearly, it requires the knowledge of a certain number of fundamental physical parameters such as surface tension, density, $T_{m\infty}$, and $\Delta H_{m\infty}$ of the specific drug/polymorphic species. Furthermore, the presented model constitutes the starting point for the development of a thermodynamic model able to consider the actual shape of drug

nanocrystals (typically appearing in form of complex prisms) and the possible variation of surface energy on the various crystal facets.

Nevertheless, in the present thesis, in order to evaluate the bioavailability enhancement deriving from the use of nanocrystalline and amorphous drugs, a physiologically oriented mathematical model aimed at studying in vivo drug release, absorption, distribution, metabolism, and elimination (ADME), with particular attention to the use of drugs embedded in polymeric matrices, was also developed. In fact, quite recently, the Pharmaceutical Research and Manufacturers of America tested the reliability of predictive models in terms of drug efficacy, safety, and properties estimation. In particular, physiologically based pharmacokinetic (PBPK) models, useful theoretical tools for the evaluation of the hepatic clearance and tissue distribution by resorting to in vitro and in silico data, showed, in the 69% of the cases, a medium-high degree of accuracy in simulating the time variation of the plasma drug concentration in humans following the intravenous administration, while, on the contrary, accuracy appeared to decrease to 23% in the case of oral administration.

Predicting the time variation of the drug concentration in plasma/blood following the oral administration presents the considerable difficulty of simulating both the delivery and the absorption stages. In this light, being the oral administration the most common one, the present project attempted to establish a deep connection between ADME phenomena and the delivery of drugs in the form of macro and nanocrystals. In particular, the considered delivery system consists of an ensemble of non-eroding polydispersed polymeric particles loaded with the drug. Particulate systems, indeed, easily disperse within the stomach resulting in an appreciable decrease of local drug concentration and, as a consequence, a considerable reduction of the insurgence of gastric irritations.

The adopted mathematical representation of the human body relies on the PBPK model developed by Di Muria and co-workers: the release environment fluids, due to peristalsis, flow from the gastric environment to the small and large intestine. Once the drug leaves the delivery system, it first reaches the gastrointestinal release environment fluids and then, by permeating the gastrointestinal mucous membranes, the gastrointestinal circulatory system (GICS). Afterward, through the portal vein, it enters the liver where it undergoes a partial elimination by metabolic clearance. Finally, the drug reaches the plasma through the hepatic vein. From the plasma, the drug may be exchanged with the less perfused tissues and return to the liver through the hepatic artery or to the GICS through the portal vein.

The delivery model assumes that drug release kinetics is essentially determined by the polymeric particles size distribution in the dry state and their swelling on contact with the release environment

fluids, the drug dissolution and diffusion within the swollen particles, and the possible recrystallization of amorphous or nanocrystalline drugs in the release environment fluids. In particular, the swelling process, aside from the traditional fickian diffusion, considers a non-fickian component of the solvent flux representing a delayed flux induced by the polymer-solvent couple viscoelastic character. The existence of two contributions in the solvent flux is motivated by the fact that polymeric chains undergo rearrangements which develop with time after the solvent uptake, i.e. the relaxation phenomena. Interestingly, this viscoelastic behavior of polymeric meshes also affects the drug release from the delivery system. Indeed, the convective field induced by the stress gradient due to the fluid uptake into the particles acts similarly to a pressure gradient inside a pipe.

The constructed model was then tested against three widely used drugs: theophylline (no solubility issues), temazepam (low solubility), and nimesulide (low solubility). This mathematical model allows comparing different formulations of the same drug or the same formulation for different drugs, evaluating the effect of different doses, various particles mean sizes or distributions, and different solid forms, i.e. amorphous, nanocrystalline, and microcrystalline. One of the most noteworthy results of this study is the quantitative evaluation of the interplay between release kinetics and the subsequent ADME processes. Indeed, it is usually assumed that the in vivo drug release coincides with the in vitro one with the result of neglecting the effect of the ADME processes. In fact, the proposed model demonstrates that the in vivo release kinetics may be different from the in vitro one due to the effect of living tissues. In conclusion, the present model may be taken into consideration and further developed as a useful tool for the design of different oral delivery systems.

CHAPTER 7

REFERENCES

Abbiati, R.A.; Cavallaro, G.; Craparo, E.F.; Manca, D. Chem. Eng. Trans. 2015a, 43, 283–288.

Abbiati, R.A.; Lamberti, G.; Barba, A.A.; Grassi, M.; Manca, D. Comput. Aided Chem. Eng. 2015b, 37, 77–84.

Adamson, A. W.; Gast, A. P. Physical chemistry of surfaces, 6 ed.; Wiley-Interscience: New York, 1997.

Amidon, G.L.; Lennernäs, H.; Shah, V.P.; Crison, J.R. Pharm. Res. 1995, 12, 413–420.

Androulakis, I. P. Curr. Pharmacol. Rep. 2016, 2, 152–160.

Astarita, G. Adv. Chem. Ser. 1980, 190, 205–226.

Badruddoza, A. Z. M.; Godfrin, P. D.; Myerson, A. S.; Bernhardt L.; Trout, B. L.; Doyle, P. S. Adv. Healthcare Mater. 2016, 5, 1960–1968.

Bahl, D.; Bogner, R. H. Pharm. Res. 2006, 23, 2317–2325.

Bayly, C. I.; Cieplak, P.; Cornell, W.; Kollman, P. A. J. Phys. Chem. 1993, 97, 10269–10280.

Beiner, M.; Rengarajan, G. T.; Pankaj, S.; Enke, D.; Steinhart, M. Nano Lett. 2007, 7, 1381–1385.

Belenguer, A. M.; Lampronti, G. I.; Cruz-Cabeza, A. J.; Hunter, C. A.; Sanders, J. K. M. Chem. Sci. 2016, 7, 6617–6627.

Berendsen, H. J. C.; Postma, J. P. M.; van Gunsteren, W. F.; DiNola, A.; Haak, J. R. J. Chem. Phys. 1984, 81, 3684–3690.

Bergese, P.; Alessandri, I.; Colombo, I.; Coceani, N.; Depero L. E. Compos. Part A Appl. Sci. Manuf. 2005, 36, 443–448.

Bergese, P.; Colombo, I.; Gervasoni, D.; Depero, L. E. J. Phys. Chem. B 2004, 108, 15488–15493.

Bergese, P.; Colombo, I.; Gervasoni, D.; Depero, L.E. J. Appl. Cryst. 2003, 36, 74–79.

Bernareggi, A. Clin. Pharmacokinet. 1998, 35, 247–274.

Bianchi, M.; Broggini, M. Drugs 2003, 63, 37–46.

Bissell, M. J.; Barcellos-Hoff, M. H. J. Cell. Sci. 1987, 8, 327–343.

Bowles, A.; Keane, J.; Ernest, T.; Clapham, D.; Tuleua, C. Int. J. Pharm. 2010, 395, 37–43.

Breitkreutz, J. Pharm. Res. 1998, 15, 1370–1375.

Brun, M.; Lallemand, A.; Quinson, J. F.; Eyraud, C. J. Chim. Phys. Phys.-Chim. Biol. 1973, 70, 979–989.

Buckton, G.; Beezer, A. E. Int. J. Pharm. 1992, 82, R7–R10.

Bugay, D.E. Adv. Drug Deliv. Rev. 2001, 48, 43-65.

Camera-Roda, G.; Sarti, G.C. AIChE J. 1990, 36, 851–860.

Carli, F.; Colombo, I.; Magarotto, L.; Motta, A.; Torricelli, C. Int. J. Pharm. 1986, 33, 115–124.

Chapra, S.C.; Canale, R. P. Numerical Methods for Engineers, 3 ed.; McGraw-Hill: Boston, 1998.

Charman, S.A.; Charman, W.N.; Rogge, M.C.; Wilson, T.D.; Dutko, F.J.; Pouton, C.W. Pharm. Res. 1992, 9, 87–93.

Chiarappa, G.; Grassi, M.; Abrami, M.; Abbiati, R. A.; Barba, A. A.; Boisen, A.; Brucato, V.; Ghersi, G.; Caccavo, D.; Cascone, S.; Caserta, S.; Elvassore, N.; Giomo, M.; Guido, S.; Lamberti, G.; Larobina, D.; Manca, D.; Marizza, P.; Tomaiuolo, G.; Grassi, G. Curr. Drug Deliv. 2017, 14, 158–178.

Chiarappa, G.; Piccolo, A.; Colombo, I.; Hasa, D.; Voinovich, D.; Moneghini, M.; Grassi, G.; Farra, R.; Abrami, M.; Posocco, P.; Pricl, S.; Grassi, M. Cryst. Growth Des. 2017, 17, 4072−4083.

Cignarella, G.; Vianello, P.; Berti, F.; Rossoni, G. Eur. J. Med. Chem. 1996, 31, 359–364.

Coceani, N.; Magarotto, L.; Ceschia, D.; Colombo, I.; Grassi, M. Chem. Eng. Sci. 2012, 71, 345–355.

Colombo, I.; Grassi, G.; Grassi, M. J. Pharm. Sci. 2009, 98, 3961–3986.

Constantinides, P.P. Pharm. Res. 1995, 12, 1561–1572.

Cooper, E. R. J. Control. Release 2010, 141, 300–302.

Crowley K. J.; Zografi G. J. Pharm. Sci. 2002, 91, 492–507.

Csanda, E.; Harcos, P.; Bacsy, Z.; Berghammer, R.; Kenez, J. Drug. Dev. Res. 1988, 14, 185–187.

Curtis, T.M.; Scholfield, C.N. J. Physiol. 2001, 532, 609–623.

Davis, R.; Brogden, R. N. Drugs 1994, 48, 431–454.

Davis, R.; Brogden, R.N. Drugs 1994, 48, 431–454.

Debenedetti, P. G.; Tom, J. W.; Yeo, S. D.; Lim, G. B. J. Control. Release 1993, 24, 27–44.

Del Cont, R.; Abrami, M.; Hasa, D.; Perissutti, B.; Voinovich, D.; Barba, A.; Lamberti, G.; Grassi, G.; Colombo, I.; Grassi, M. ADMET & DMPK 2014, 2, 80–97.

Di Muria, M.; Lamberti, G.; Titomanlio, G. Ind. Eng. Chem. Res. 2010, 49, 2969–2978.

Dobetti, L.; Cadelli, G.; Furlani, D.; Zotti, M.; Ceschia, D.; Grassi, M. IDrugs. 2001, 4, 728–729.

Dwyer, L.; Kulkarni, S.; Ruelas, L.; Myerson, A. S. Crystals 2017, 7, 131 (1-14).

Eral, H. B.; López-Mejías, V.; O'Mahony, M.; Trout, B. L.; Myerson, A. S.; Doyle, P. S. Cryst. Growth Des. 2014, 14, 2073−2082.

Fallavena, P.R.B.; Schapoval, E.E.S. Int. J. Pharm. 1997, 158, 109–112.

Fedors, R. F. Polym. Eng. Sci. 1974, 14, 147–154.

Feig, L. A.; Peppas, N. A.; Colton, C. K.; Smith, K. A.; Lees, R. S. Atherosclerosis 1982, 44, 307–318.

Ferrari, M. Nat. Rev. Cancer 2005, 5, 161–171.

Ferreira, J. A.; Grassi, M.; Gudiño, E.; De Oliveira P. Appl. Math. Model. 2015, 39, 194–204.

Ferreira, J. A.; Grassi, M.; Gudiño, E.; De Oliveira P. SIAM J. Appl. Math. 2014, 74, 620–633.

Flory, P. J. Principles of polymer chemistry; Cornell University Press: Ithaca, 1953.

Folkman, J.; Haudenschild, C. Nature 1980, 288, 551–556.

Gadkar, K.; Kirouac, D.; Parrott, N.; Ramanujan, S. Drug Discov. Today Technol. 2016, 21–22, 57–65.

Gasco, M.R. Industrial applications of microemulsions, Chap. 5; Marcel Dekker: New York, 1997.

Gibbs, J. W. The Collected Works of J. Willard Gibbs; Yale University Press: New Haven, 1928.

Gilis, P.M.V.; De Conde, V.F.V.; Vandecruys, R.P.G. Beads having a core coated with an antifungal and a polymer, US Patent 5633015.

Goswami, G. K.; Nanda, K. K. Curr. Nanosci. 2012, 8, 305-311.

Granberg, R.A.; Rasmuson, Å.C. J. Chem. Eng. Data, 1999, 44, 1391–1395.

Grassi, M.; Colombo, I.; Carli, F.; Lapasin, R. Eur. J. Pharm. Sci. 1998, 6, S65.

Grassi, M.; Colombo, I.; Lapasin, R. J. Control. Release 2000, 68, 97–113.

Grassi, M.; Grassi, G.; Lapasin, R.; Colombo I. Understanding drug release and absorption mechanisms: a physical and mathematical approach; CRC Press: Boca Raton, 2007.

Grassi, M.; Voinovich, D.; Moneghini, M.R.; Franceschinis, E.; Perissutti, B.; Filipović-Grčić, J. J. Control. Release 2003, 88, 381–391.

Graubner, G.; Rengarajan, G. T.; Anders, N.; Sonnenberger, N.; Enke, D.; Beiner, M.; Steinhart, M. Cryst. Growth Des. 2014, 14, 78−86.

Groom, C.R.; Bruno, I.J.; Lightfoot, M.P.; Ward, S.C. Acta Crystallogr. B Struct. Sci. Cryst. Eng. Mater. 2016, 72, 171–179.

Ha, J. M.; Hillmyer, M. A.; Ward, M. D. J. Phys. Chem. B 2005, 109, 1392–1395.

Ha, J. M.; Wolf, J. H.; Hillmyer, M. A.; Ward, M. D. J. Am. Chem. Soc. 2004, 126, 3382–3383.

Hamilton, B. D.; Ha, J. M.; Hillmyer, M. A.; Ward, M. D. Acc. Chem. Res. 2012, 45, 414–423.

Hasa, D.; Carlotta, G.; Perissutti, B.; Voinovich, D.; Grassi, M.; Cervellino, A.; Masciocchi, N.; Guagliardi, A. Mol. Pharm. 2016, 13, 3034–3042.

Hasa, D.; Miniussi, E.; Jones, W. Cryst. Growth Des. 2016, 16, 4582–45885.

Hasa, D.; Perissutti, B.; Chierotti, M. R.; Gobetto, R.; Grabnar, I.; Bonifacio, A.; Dall'Acqua, S.; Invernizzi, S.; Voinovich, D. Int. J. Pharm. 2012, 436, 41–57.

Hasa, D.; Voinovich, D.; Perissutti, B.; Bonifacio, A.; Grassi, M.; Franceschinis, E.; Dall'Acqua, S.; Speh, M.; Plavec, J.; Invernizzi, S. J. Pharm. Sci. 2011, 100, 915–932.

Hasa, D.; Voinovich, D.; Perissutti, B.; Grassi, G.; Fiorentino, S. M.; Farra, R.; Abrami, M.; Colombo, I.; Grassi, M. Eur. J. Pharm. Sci. 2013, 50, 17–28.

Hecq, J.; Deleers, M.; Fanara, D.; Vranckx, H.; Amighi, K. Int. J. Pharm. 2005, 299, 167–177.

Heng, J. Y. Y.; Bismarck, A.; Lee, A. F.; Wilson, K.; Williams, D. R. Langmuir 2006, 22, 2760–2769.

Higuchi, W.I.; Bernardo, P.D.; Mehta, S.C. J. Pharm. Sci. 1967, 56, 200–207.

Huang, W. J.; Sun, R.; Tao, J.; Menard, L. D.; Nuzzo, R. G.; Zuo, J. M. Nat. Mater. 2008, 7, 308–313.

Ishikiriyama, K.; Todoki, M.; Motomura, K. J. Colloid Interface Sci. 1995, 171, 92–102.

Jain, R.; Gerlowski, L.; Weissbrod, J.; Wang, J.; Pierson, R. Ann. Biomed. Eng. 1981, 9, 347–361.

Jiang, Q.; Shi, H. X.; Zhao, M. Acta Mater. 1999, 7, 2109–2112.

Jones, R.D.; Jones, H.M.; Rowland, M.; Gibson, C.R.; Yates, J.W.T.; Chien, J.Y.; Ring, B.J.; Adkison, K.K.; Ku, M.S.; He, H.; Vuppugalla, R.; Marathe, P.; Fischer, V.; Dutta, S.; Sinha, V.K.; Björnsson, T.; Lavé, T.; Poulin, P. J. Pharm. Sci. 2011, 100, 4074–4089.

Kaminsky, W. J. Appl. Cryst. 2007, 40, 382–385.

Kikic, I.; Lora, M.; Cortesi, A.; Sist, P. Fluid Phase Equilib. 1999, 158-160, 913–921.

Knight-Schrijver, V. R.; Chelliah, V.; Cucurull-Sanchez, L.; Le Novère, N. Comput. Struct. Biotechnol. J. 2016, 14, 363–370.

Kumar, D.; Shastri, N. R. Cryst. Growth Des. 2014, 14, 326–338.

Kumar, P.; Mittal, L.K. Handbook of microemulsion science and technology; Marcel Dekker: New York, 1999.

Kwok, D.Y.; Neumann, A.W. Adv. Colloid Interface Sci., 1999, 81, 167–250.

Laporte, J.R.; Ibáñez, L.; Vidal, X.; Vendrell, L.; Leone, R. Drug Saf. 2004, 27, 411–420.

Lee, S. Y.; Yu, G.; Shin, K.; Kim, I. W. J. Nanosci. Nanotechnol. 2013, 13, 2348–2353.

Levich, V.G. Physicochemical Hydrodynamics; Prentice Hall: Englewood Cliffs, 1962.

Lipinski, C. Am. Pharm. Rev. 2002, 5, 82–85.

Lörincz, C.; Szász, K.; Kisfaludy, L. Arzneimittelforschung 1976, 26, 1907.

Lu, H. M.; Wen, Z.; Jiang, Q. J. Phys. Org. Chem. 2007, 20, 236–240.

Lubashenko, V. V. J. Nanopart. Res. 2010, 12, 1837–1844.

Luther, J.M. Curr. Opin. Nephrol. Hypertens. 2014, 23, 456–461.

Lutterotti, L.; Ceccato, R.; Dal Maschio, R.; Pagani, E. Mater. Sci. Forum 1998, 278-281, 87-92.

Madras, G.; McCoy, B. J. Cryst. Growth Des. 2003, 3, 981–990.

Magomedov M. N. Phys. Solid State 2004, 46, 954–968.

Magomedov M. N. Tech. Phys. 2011, 56, 1277–1282.

McDonald, T.F.; Pelzer, S.; Trautwein, W.; Pelzer, D.J. Physiol. rev. 1994, 74, 365–507.

Meriani, F.; Coceani, N.; Sirotti, C.; Voinovich, D.; Grassi, M. J. Pharm. Sci. 2004, 93, 540–552.

Mosharraf, M.; Nyström, C. Drug Dev. Ind. Pharm. 2003, 29, 603–622.

Murdande, S. B.; J. Pikal, M. J.; Shanker, R. M.; Bogner, R. H. J. Pharm. Sci. 2010, 99, 1254–1264.

Musante, C. J.; Abernethy, D. R.; Allerheiligen, S. R. B.; Lauffenburger, D. A.; Zager, M. G. CPT Pharmacometrics Syst. Pharmacol. 2016, 5, 449–451.

Nanda, K. K. Pramana 2009, 72, 617–628.

Newton, J.M. Int. J. Pharm. 2010, 395, 2–8.

Nogami, H.; Nagai, T.; Yotsuyanagi, T. Chem. Pharm. Bull. 1969, 17, 499–509.

O'Mahony, M.; Leung, A. K.; Ferguson, S.; Trout, B. L.; Allan S.; Myerson, A. S. Org. Process Res. Dev. 2015, 19, 1109−1118.

Paolini, M.; Vacis, G. Il racconto del Vajont; Garzanti: Milano, 1997.

Patankar, S. V. Numerical Heat Transfer and Fluid Flow; Hemisphere Publishing: New York, 1986.

Pawlow, P. Z. Phys. Chem. 1909, 65, 1–35.

Peppas, N. A. One Hundred Years of Chemical Engineering; Kluwer: Amsterdam, 1989.

Peppas, N. A.; Langer, R. AIChE J. 2004, 50, 536–546.

Peppas, N. A.; Reinhart, C. T. J. Memb. Sci. 1983, 15, 275–287.

Perrett, S.; Venkatesh, G. Inov. Pharm. Technol. 2006, 19, 80–85.

Pinto, J.F. Int. J. Pharm. 2010, 395, 44–52.

Podczeck, F. Int. J. Pharm. 2010, 395, 1.

Poulin, P.; Jones, H.M.; Jones, R.D.; Gibson, C.R.; Rowland, M.; Chien, J.Y.; Ring, B.J.; Adkison, K.K.; Ku, M.S.; He, H.; Vuppugalla, R.; Marathe, P.; Fischer, V.; Dutta, S.; Sinha, V.K.; Björnsson, T.; Lavé, T.; Yates, J.W.T. J. Pharm. Sci. 2011, 100, 4127–4157.

Poulin, P.; Jones, H.M.; Jones, R.D.; Yates, J.W.T.; Gibson, C.R.; Chien, J.Y.; Ring, B.J.; Adkison, K.K.; He, H.; Vuppugalla, R.; Marathe, P.; Fischer, V.; Dutta, S.; Sinha, V.K.; Björnsson, T.; Lavé, T.; Ku, M.S. J. Pharm. Sci. 2011, 100, 4051–4073.

Pouton, C.W. Adv. Drug Deliv. Rev. 1997, 25, 47–58.

Prausnitz, J.M.; Lichtenthaler, R.N.; Azevedo, E.G. Molecular Thermodynamics of Fluid-Phase Equilibria, 3rd ed.; Prentice Hall: Englewood Cliffs, 1999.

Proffen, T.H.; Billinge, S.J.L.; Egami, T.; Louca, D. Z. Kristallogr. 2003, 218, 132–143.

Puttaraja; Nirmala, K. A.; Sakegowda, D. S.; Duax, W. L. J. Crystallogr. Spectrosc. Res. 1982, 12, 415–423.

Rainsford, K.D. Curr. Med. Res. Opin. 2006, 22, 1161–1170.

Rainsford, K.D. Nimesulide – Actions and Uses; Birkhäuser: Basel, 2005.

Rengarajan, G. T.; Enke, D.; Steinhart, M.; Beiner, M. J. Mater. Chem. 2008, 18, 2537–25395.

Ring, B.J.; Chien, J.Y.; Adkison, K.K.; Jones, H.M.; Rowland, M.; Jones, R.D.; Yates, J.W.T.; Ku, M.S.; Gibson, C.R.; He, H.; Vuppugalla, R.; Marathe, P.; Fischer, V.; Dutta, S.; Sinha, V.K.; Björnsson, T.; Lavé, T.; Poulin, P. J. Pharm. Sci. 2011, 100, 4090–4110.

Rowlinson, J. S.; Windom, B. Molecular theory of capillarity; Clarendon Press: Oxford, 1982.

Samsonov, V. M.; Sdobnyakov, N. Y.; Bazulev, A. N. Colloids Surf., A 2004, 239, 113–117.

Sanphui, P.; Sarma, B.; Nangia, A. J. Pharm. Sci. 2011, 100, 2287–2299.

Sar, D. K.; Nayak, P.; Nanda, K. K. Phys. Lett. A 2008, 372, 4627–4629.

Sdobnyakov, N. Y.; Samsonov, V. M.; Bazulev, A. N.; Kul'pin, D. A. Bull. Russ. Acad. Sci. Phys. 2008, 72, 1371–1373.

Sonnenberger, N.; Anders, N.; Golitsyn, Y.; Steinhart, M.; Enke, D.; Saalwächter, K.; Beiner, M. Chem. Commun. 2016, 52, 4466-4469.

Sorger, P. K.; Abernethy, D. R.; Allerheiligen, S. R. B.; Altman, R.B.; Brouwer, K. L. R.; Califano, A.; D'Argenio, D. Z.; Iyengar, R.; Jusko, W. J.; Lalonde, R. L.; Lauffenburger, D. A.; Shoichet, B.; Stevens, J. L.; Subramaniam, S.; van der Graaf, P.; Vicini, P.; Ward, R. QSP White Paper 2011.

Stephenson, G.A.; Forbes, R.A.; Reutzel-Edens, S.M. Adv. Drug Deliv. Rev. 2001, 48, 67–90.

Swaminathan, S.; Edwards, D. A. Appl. Math. Lett. 2004, 17, 7–12.

Toledano, J.-C.; Toledano, P. The Landau theory of Phase Transitions; World Scientific: Singapore, 1987.

Tolman, R. C. J. Chem. Phys. 1949, 17, 333–337.

Triggle, A. M.; Shefter, E.; Triggle, D. J. J. Med. Chem. 1980, 23, 1442–1445.

Tripathi, K.D. Essentials of medical pharmacology, 6 ed.; Jaypee: New Delhi, 2008.

Truskey, G.A.; Yuan, F.; Katz D. F. Transport Phenomena in Biological Systems; Prentice Hall: Upper Saddle River, 2004.

Ueda, Y.; Shimojo, F.; Shimazaki, Y.; Kado, K.; Honbo, T. Solid Dispersion Composition of FR-900506 Substance, US Patent 4916138.

Vacanti, J.; Morse, M.; Saltzman, M.; Domb, A.; Perez-Atayde, A.; Langer, R. J. Pediatr. Surg. 1988, 23, 3–9.

van der Graaf, P. H.; Benson, N. Pharm. Res. 2011, 28, 1460–1464.

van Krevelen, D.W. Properties of Polymers, 3 ed.; Elsevier: Amsterdam, 1990.

van Krevelen, D.W.; Hoftyzer, P.J. Properties of polymers, 2 ed.; Elsevier: Amsterdam, 1976.

Van Mourik, I.D.; Thomson, M.; Kelly, D.A. Liver Transpl. Surg. 1999, 5, 107–111.

Varum, F.J.O.; Merchant, H.A.; Basit, A.W. Int. J. Pharm. 2010, 395, 26–36.

Voinovich, D.; Perissutti, B.; Grassi, M.; Passerini, N.; Bigotto, A. J. Pharm. Sci. 2009, 98, 4119–4129.

Vuppugalla, R.; Marathe, P.; He, H.; Jones, R.D.; Yates, J.W.T.; Jones, H.M.; Gibson, C.R.; Chien, J.Y.; Ring, B.J.;Adkison, K.K.; Ku, M.S.; Fischer, V.; Dutta, S.; Sinha, V.K.; Björnsson, T.; Lavé, T.; Poulin, P. J. Pharm. Sci. 2011, 100, 4111–4126.

Wagner, J.G. Pharmacokinetics for the Pharmaceutical Scientist; Technomic: Basel, 1993.

Weinshaar, R. E.; Bristol, J. A.; Hansch, C. Comprehensive medicinal chemistry; Pergamon Press: Oxford, 1990.

Wichterle, O.; Lim, D. Nature 1960, 185, 117–118.

Wilson, C.G. Int. J. Pharm. 2010, 395, 17–25.

Yu, L. Adv. Drug Deliv. Rev. 2001, 48, 27-42.

Yu, L.X.; Gatlin, L.; Amidon, G.L. Transport processes in pharmaceutical systems, Chap. 10; Marcel Dekker: New York, 2000.

Yuen, K.H. Int. J. Pharm. 2010, 395, 9–16.

Zandavi, S. H.; Ward, C. A. J. Colloid Interface Sci. 2013, 407, 255–264.

Zhang, M.; Efremov, M. Y.; Schiettekatte, F.; Olson, E. A.; Kwan, A. T.; Lai, S. L.; Wisleder, T.; Greene, J. E.; Allen, L. H. Phys. Rev. B 2000, 62, 10548–10557.

Zhu, W.; Romanski, F. S.; Dalvi, S. V.; Dave, R. N.; Tomassone, M. S. Chem. Eng. Sci. 2012, 73, 218–230.